

C

Internal Report  
DESY F35D-97-02  
February 1997

*Gift aus*



\*X1997-00325\*

# Measurement of Elastic $\omega$ Photoproduction at HERA

by

J. Grosse-Knetter

Eigentum der	<b>DESY</b>	Bibliothek
Property of		library
Zugang	17. FEB. 1997	
Accession		
Leihfrist	7	Days
Loan period:		days

**DESY behält sich alle Rechte für den Fall der Schutzrechtserteilung und für die wirtschaftliche Verwertung der in diesem Bericht enthaltenen Informationen vor.**

**DESY reserves all rights for commercial use of information included in this report, especially in case of filing application for or grant of patents.**

**\*Die Verantwortung für den Inhalt dieses  
Internen Berichtes liegt ausschließlich beim Verfasser\***

# Measurement of Elastic $\omega$ Photoproduction at HERA

Dissertation

zur Erlangung des Doktorgrades  
des Fachbereichs Physik  
der Universität Hamburg

vorgelegt von  
Jörn Grosse-Knetter ✓  
aus Versmold

Hamburg 1997

**Gutachter der Dissertation** : Prof. Dr. E. Lohrmann  
Prof. Dr. V. Blobel

**Gutachter der Disputation** : Prof. Dr. E. Lohrmann  
Prof. Dr. B. Naroska

**Datum der Disputation** : 03.02.1997

**Sprecher des Fachbereichs  
Physik und Vorsitzender  
des Promotionsausschusses** : Prof. Dr. B. Kramer

## Zusammenfassung

Am ZEUS-Detektor ist die Reaktion  $\gamma p \rightarrow \omega p$  ( $\omega \rightarrow \pi^+ \pi^- \pi^0$  und  $\pi^0 \rightarrow \gamma\gamma$ ) in  $ep$  Wechselwirkungen untersucht worden. Der betrachtete kinematische Bereich war durch eine Photon-Proton Schwerpunktsenergie zwischen 70 und 90 GeV und durch  $|t| < 0.6 \text{ GeV}^2$  gegeben, wobei  $t$  das Quadrat des übertragenen Viererimpulses am Protonvertex ist. Der Wirkungsquerschnitt der elastischen  $\omega$  Photoproduktion wurde zu  $\sigma^{\gamma p \rightarrow \omega p} = 1.21 \pm 0.12 \pm 0.23 \mu\text{b}$  bestimmt. Der differentielle Wirkungsquerschnitt  $d\sigma^{\gamma p \rightarrow \omega p}/d|t|$  fällt exponentiell wie  $e^{-b|t|}$ . Der Parameter wurde zu  $b = 10.0 \pm 1.2 \pm 1.3 \text{ GeV}^{-2}$  bestimmt. Die Winkelverteilungen der Zerfallspionen sind mit  $s$ -Kanal-Helizitätserhaltung verträglich. Das Verhältnis  $\sigma^{\gamma p \rightarrow \rho^0 p} : \sigma^{\gamma p \rightarrow \omega p} : \sigma^{\gamma p \rightarrow \phi p}$  bei einer Photon-Proton Schwerpunktsenergie von etwa 80 GeV wurde zu  $9.17 \pm 0.92 \pm 2.27 : 1 : 0.81 \pm 0.11 \pm 0.09$  bestimmt.

## Abstract

The reaction  $\gamma p \rightarrow \omega p$  ( $\omega \rightarrow \pi^+ \pi^- \pi^0$  and  $\pi^0 \rightarrow \gamma\gamma$ ) has been studied in  $ep$  interactions using the ZEUS detector at photon-proton centre-of-mass energies between 70 and 90 GeV and  $|t| < 0.6 \text{ GeV}^2$ , where  $t$  is the squared four-momentum transferred at the proton vertex. The elastic  $\omega$  photoproduction cross section has been measured to be  $\sigma^{\gamma p \rightarrow \omega p} = 1.21 \pm 0.12 \pm 0.23 \mu\text{b}$ . The differential cross section  $d\sigma^{\gamma p \rightarrow \omega p}/d|t|$  has an exponential shape  $e^{-b|t|}$  with a slope  $b = 10.0 \pm 1.2 \pm 1.3 \text{ GeV}^{-2}$ . The angular distributions of the decay pions are consistent with  $s$ -channel helicity conservation. The ratio  $\sigma^{\gamma p \rightarrow \rho^0 p} : \sigma^{\gamma p \rightarrow \omega p} : \sigma^{\gamma p \rightarrow \phi p}$  at a photon-proton centre-of-mass energy of approximately 80 GeV was determined to be  $9.17 \pm 0.92 \pm 2.27 : 1 : 0.81 \pm 0.11 \pm 0.09$ .

# Contents

<b>1</b>	<b>Introduction</b>	<b>1</b>
<b>2</b>	<b>Physics at HERA</b>	<b>3</b>
2.1	Positron-Proton Scattering	3
2.1.1	Kinematics	3
2.1.2	The Electromagnetic Cross Section	5
2.2	Photoproduction	6
2.2.1	Relating $ep$ and $\gamma p$ Cross Sections	7
2.2.2	Vector Meson Dominance Model	8
2.2.3	Classification of the Processes	10
2.3	Elastic Vector Meson Photoproduction	11
2.3.1	Calculation of the $\gamma p \rightarrow Vp$ Cross Section	14
2.3.2	Cross Section Dependence on $t$	14
2.3.3	Decay Angular Distributions	15
2.3.4	Relation to Hadronic Cross Sections	16
2.3.5	Determination of the $\gamma \leftrightarrow V$ Coupling Constants	17
2.4	Theoretical Models	18
2.4.1	Regge Theory	18
2.4.2	The Model of Wu et al.	26
2.4.3	The Model of Ryskin	30
<b>3</b>	<b>Experimental Conditions</b>	<b>33</b>
3.1	HERA	33
3.2	The ZEUS Detector	33
3.2.1	The Calorimeter	35
3.2.2	The Hadron Electron Separator	35

3.2.3	Tracking Devices	37
3.2.4	Luminosity Measurement	37
3.2.5	Background Monitors and Veto Wall	40
3.3	The Trigger for ZEUS	40
<b>4</b>	<b>Identification of Neutral Pions</b>	<b>41</b>
4.1	Preparation of RHES and RCAL Signals	41
4.1.1	RCAL	41
4.1.2	RHES	43
4.1.3	Combining RCAL and RHES	47
4.2	Reconstruction of the $\pi^0$	47
4.2.1	Low-Energy $\pi^0$ Mesons	48
4.2.2	High-Energy $\pi^0$ Mesons	50
4.2.3	Application to Data	50
4.2.4	Correction of the Energy of the Photons	51
<b>5</b>	<b>Elastic Photoproduction of <math>\omega</math> Mesons</b>	<b>57</b>
5.1	Event Selection and Reconstruction	57
5.1.1	Trigger	57
5.1.2	Selection Criteria	58
5.1.3	Reconstruction of the $\pi^0$	59
5.1.4	Reconstruction of the $\omega$	61
5.2	Acceptance Calculation and Monte Carlo Simulation	61
5.2.1	Determination of the FLT Efficiency	61
5.2.2	Monte Carlo Simulation	66
5.3	Background	72
5.3.1	Photoproduction with Photon Dissociation	72
5.3.2	Photoproduction with Proton Dissociation	73
5.3.3	Beam-Gas Interactions	73
5.4	Systematics	74
5.4.1	Checking the Cut on the RHES Energy	74
5.4.2	Systematic Errors	75
5.5	Analysis of the Mass Spectrum	76
5.5.1	Evaluation of the Number of Events	76
5.5.2	Background Below the Resonances	76

5.6	Results	80
5.6.1	Elastic $\gamma p \rightarrow \omega p$ Cross Section	80
5.6.2	Differential Cross Section $d\sigma^{\gamma p \rightarrow \omega p}/d t $	82
5.6.3	Decay Angular Distributions	83
5.6.4	The Total $\omega p$ Cross Section	86
5.6.5	The $\gamma \leftrightarrow \omega$ Coupling Constant	86
<b>6</b>	<b>Comparison of Elastic Photoproduction of <math>\rho^0</math>, <math>\omega</math> and <math>\phi</math> Mesons</b>	<b>87</b>
6.1	Comparison with Existing Measurements of Elastic $\rho^0$ and $\phi$ Photoproduction	87
6.2	Evaluation of the $\omega$ to $\phi$ Cross Section Ratio in the $\pi^+\pi^-\pi^0$ Decay Mode	88
6.2.1	Event Selection and Reconstruction	88
6.2.2	Acceptance Calculation	91
6.2.3	Systematics	91
6.2.4	Analysis of the Mass Spectrum	91
6.2.5	Ratio of the Cross Sections	93
6.3	Discussion	94
<b>7</b>	<b>Conclusion</b>	<b>97</b>
<b>A</b>	<b>Decay Angular Distributions</b>	<b>99</b>
A.1	The Density Matrices	99
A.2	The Probability Distributions	100
A.3	The Density Matrices in Case of SCHC	102

## List of Figures

2.1	Schematic diagram of $ep$ scattering	4
2.2	The kinematical range at HERA in the $W_{\gamma^*p}$ - $Q^2$ -plane	5
2.3	Schematic picture of $\gamma p$ reactions in VDM	9
2.4	Classification of the VDM processes	12
2.5	Schematic diagram of the reaction $ep \rightarrow eVp$	13
2.6	Decay angles in the vector meson restframe	15
2.7	Integration paths in the complex $\ell$ -plane	20
2.8	Chew-Frautschi plot for some mesons	21
2.9	Total hadronic cross sections	23
2.10	Measured slope parameters for elastic $\pi^\pm p$ and $K^\pm p$ reactions	24
2.11	Slopes of the reactions $\gamma p \rightarrow Vp$	25
2.12	Predictions for $\gamma p \rightarrow Vp$ cross sections	27
2.13	Regge fits to $\pi^\pm p$ and $K^\pm p$ data	28
2.14	Gluon ladders for vector meson production	30
3.1	ZEUS in longitudinal cut	34
3.2	ZEUS in cross section	34
3.3	FCAL Module	36
3.4	Schematic view of RHES in RCAL	38
3.5	Structure of a silicon pad	38
3.6	Geometrical structure of RHES	39
4.1	Signal reconstruction of an RHES pad	44
4.2	$E_{HES}$ versus photon energy	45
4.3	Position reconstruction for RHES	46
4.4	Opening angle in the $\pi^0 \rightarrow \gamma\gamma$ decay	47
4.5	Average cosine of the opening angle in the $\pi^0 \rightarrow \gamma\gamma$ decay	47

4.6	Expected width of the $m_{\gamma\gamma}$ peak	49
4.7	Reconstructed two photon mass for merged RCAL clusters	51
4.8	Shift in $\langle m_{\gamma\gamma} \rangle$ for merged RCAL clusters	51
4.9	Measured spectrum of $m_{\gamma\gamma}$ in DIS events	52
4.10	Inactive material in front of RCAL	53
4.11	Correction function from Monte Carlo	53
4.12	Measured and corrected spectrum of $m_{\gamma\gamma}$ in DIS events	54
4.13	Correction function with the presampler	55
4.14	Measured and corrected spectrum of $m_{\gamma\gamma}$ in DIS events	56
5.1	Invariant mass of the $\gamma\gamma$ system	60
5.2	$\pi^+\pi^-\pi^0$ -mass with cut on $m_{\gamma\gamma}$	62
5.3	$\pi^+\pi^-\pi^0$ -mass after constraining $m_{\gamma\gamma}$ to $m_{\pi^0}$	62
5.4	Division of RCAL at FLT	63
5.5	FLT-efficiencies of $\pi^+$ and $\pi^-$	64
5.6	FLT-efficiency for photons	66
5.7	Acceptance as function of $W_{\gamma p}$ , $p_T^2$ , $\cos\theta_h$ and $\phi_h$	68
5.8	Comparison data-Monte Carlo for $W_{\gamma p}$ , $p_T^2$ , $\cos\theta_h$ and $\phi_h$	69
5.9	Comparison data-Monte Carlo for $E_{CAL}$ and $E_{HES}$	70
5.10	Dependence of the Monte Carlo on $W_{\gamma p}$	71
5.11	Probability distribution for $\log_{10} Q^2$ for $\xi = 0$ or 1	72
5.12	Track momentum and energy in RHES for conversion $e^\pm$	74
5.13	Spectrum of $m_{3\pi}$ after all cuts	77
5.14	Spectrum of $m_{3\pi}$ for background from non-resonant $\gamma\gamma$	79
5.15	Spectrum of $m_{3\pi}$ for background from $\gamma p \rightarrow Xp$ reactions	79
5.16	Sum of the $m_{3\pi}$ spectra from both background models	80
5.17	Elastic cross section for $\gamma p \rightarrow \omega p$	81
5.18	Conversion of $p_T^2$ to $ t $	83
5.19	Differential cross section $d\sigma^{\gamma p \rightarrow \omega p}/d t $	84
5.20	Corrected $ \cos\theta_h $ and $\phi_h$ distributions	85
6.1	Invariant mass of the $\gamma\gamma$ system in 1995 data	90
6.2	Spectrum of $m_{3\pi}$ after all cuts in 1995 data	92
A.1	$\epsilon$ versus $W_{\gamma p}$	103

## List of Tables

2.1	Measurements of resonant $e^+e^-$ collisions used for $f_V^2/4\pi$	19
2.2	Photoproduction measurements used for $f_V^2/4\pi$	19
2.3	Photon-vector meson coupling constants $f_V^2/4\pi$	19
2.4	Regge fits to $\pi^\pm p$ data	29
2.5	Regge fits to $K^\pm p$ data	29
5.1	Efficiencies for the reaction $\gamma p \rightarrow \omega p$	67
5.2	Systematic errors in $\sigma^{\gamma p \rightarrow \omega p}$ , $b$ and $(d\sigma/d t )_{t=0}$	82
6.1	Systematic errors in $\sigma^{\gamma p \rightarrow \omega p}$ : $\sigma^{\gamma p \rightarrow \phi p}$	93



# Chapter 1

## Introduction

The hadron electron ring accelerator HERA provides colliding beams of positrons with an energy of 27.5 GeV and protons with an energy of 820 GeV. Events in which the exchanged four-momentum between incoming and outgoing positron is small can be related to photoproduction. A special kind of reaction is the elastic photoproduction of vector mesons,  $\gamma p \rightarrow Vp$ . It has been extensively studied in fixed target experiments at photon-proton centre-of-mass energies up to  $W_{\gamma p} \approx 20$  GeV. However, HERA offers the possibility to extend the measured  $W_{\gamma p}$ -range to higher values. The photoproduction of  $\rho^0$ ,  $\omega$  and  $\phi$  is usually described in the framework of the vector meson dominance model (VDM) and Regge theory [1]. VDM relates photoproduction cross sections to those of purely hadronic processes. The  $W_{\gamma p}$  dependence of hadronic cross sections can be parametrized in Regge theory by the sum of two terms, one due to Pomeron exchange and the other to Reggeon exchange [2]. While the latter falls with  $W_{\gamma p}$ , the former is almost flat. Whereas  $\rho^0$  and  $\phi$  production is predominantly due to Pomeron exchange at all energies, the energy behaviour of  $\omega$  production investigated before HERA suggests a non-negligible contribution from Reggeon exchange. It is therefore of interest to analyse  $\omega$  photoproduction at HERA, where Pomeron exchange should dominate. More specifically, it is important to establish if the features typical of elastic  $\rho^0$  and  $\phi$  vector meson production are also observed in  $\omega$  photoproduction at high energy. Among these features are the weak dependence of the elastic cross section on  $W_{\gamma p}$ , the exponential shape of the differential cross section in  $t$ , where  $t$  is the squared four-momentum transferred at the proton vertex, and  $s$ -channel helicity conservation (SCHC) [3].

The photoproduction of  $\rho^0$ ,  $\phi$  and  $J/\psi$  has already been observed with the ZEUS detector – the corresponding results are published [4, 5, 6]. This thesis reports the first measurement of the photoproduction of  $\omega$  mesons decaying into  $\pi^+\pi^-\pi^0$  using the ZEUS detector. In contrast to the above mesons which could be identified by the decay into just two charged particles, the crucial part in this analysis of the  $\omega$  production is the reconstruction of the  $\pi^0$  meson. In addition to the track reconstruction needed to retrieve information about the charged pions, the detection of the decay  $\pi^0 \rightarrow \gamma\gamma$  requires a precise analysis of signals in the calorimeter of the ZEUS detector. The use of another component in the  $\pi^0$ -reconstruction turned out to be useful: the hadron electron separator. It is a layer of silicon diodes positioned in the calorimeter. It provides a better position resolution than obtained by the calorimeter alone due to its finer segmentation. In addition, it allows to suppress signals caused by the radioactivity of the calorimeter material.

Using the momentum information of two opposite charged tracks (supposed to be a  $\pi^+$  or  $\pi^-$

respectively) and of the  $\pi^0$ , the four-momentum of an  $\omega$  candidate was reconstructed. The  $\omega$  itself is then identified by its invariant mass. The kinematic range was restricted to  $70 < W_{\gamma p} < 90$  GeV and  $p_T^2 < 0.6$  GeV<sup>2</sup>, where  $p_T$  is the transverse momentum of the  $\omega$  with respect to the beam axis. For the considered events the scattered positron was not observed in the detector, thereby restricting the photon virtuality  $Q^2$  to values smaller than 4 GeV<sup>2</sup>, with a median  $Q^2$  of about  $10^{-4}$  GeV<sup>2</sup>.

In addition to the comparison of the results to the above theoretical expectations, the cross section for elastic  $\omega$  photoproduction can be compared with those of  $\rho^0$  and  $\phi$ , checking the corresponding prediction from the SU(6) quark model [7].

## Chapter 2

# Physics at HERA

HERA is the first storage ring with colliding positron and proton beams. This chapter deals with the physics potential of  $ep$  collisions at HERA, focusing on photoproduction. Especially the elastic photoproduction of vector mesons is discussed.

### 2.1 Positron-Proton Scattering

The scattering of positrons and protons can be described in first order as an exchange of a gauge boson between proton and positron. In the following the exchange of neutral current, i.e. the appearance of the positron in the final state is of interest. Except for events with very large momentum transfers, it is sufficient to describe this by the exchange of a photon. The scattering of positrons on protons via one-photon-exchange is shown in Figure 2.1, according to the equation:

$$e(k) + p(P) \rightarrow e'(k') + X(P'),$$

where  $X$  denotes the outgoing hadronic system. In the following the below defined variables are used as indicated in Figure 2.1:

$k$	$= (E_e, \vec{k})$	the four-momentum of the incoming positron $e$ ,
$k'$	$= (E_{e'}, \vec{k}')$	the four-momentum of the scattered positron $e'$ ,
$P$	$= (E_p, \vec{P})$	the four-momentum of the incoming proton $p$ ,
$P'$	$= (E_X, \vec{P}')$	the four-momentum of the outgoing hadronic system $X$ ,
$q$	$= k - k'$	the four-momentum of the exchanged virtual photon $\gamma^*$ ,
$\theta$	$= \angle(\vec{k}, \vec{k}')$	the angle between incoming and scattered positron,
	$m_e, m_p$	the masses of positron and proton, respectively.

#### 2.1.1 Kinematics

The scattering of positrons on protons can be described by the  $ep$  centre-of-mass energy  $\sqrt{s} = 300$  GeV, which is fixed at HERA, and any pair of the following variables:

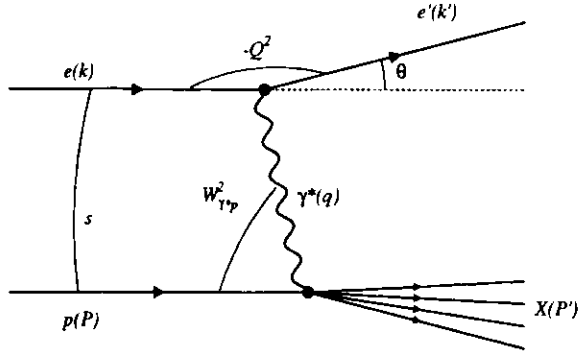


Figure 2.1: Schematic diagram of  $ep$  scattering via one-photon-exchange.

- the four-momentum squared carried by the photon,

$$Q^2 = -q^2 = -(k - k')^2 \approx 4E_e E_e' \sin^2 \frac{\theta}{2} + Q_{min}^2$$

with the kinematical limit  $Q_{min}^2 \approx \frac{m_p^2 y^2}{1-y}$ , (2.1)

- the energy transfer from the positron to the proton,

$$\nu = \frac{q \cdot P}{m_p},$$

- the relative energy transfer from the positron to the proton,

$$y = \frac{q \cdot P}{k \cdot P} = 1 - \frac{E_e'}{E_e} \cos^2 \frac{\theta}{2},$$

- the Bjorken- $x$ ,

$$x = \frac{Q^2}{2q \cdot P} = \frac{Q^2}{2\nu m_p},$$

- and the centre-of-mass energy squared of the  $\gamma^*p$  system

$$W_{\gamma p}^2 = (q + P)^2 = 2y(k \cdot P) - Q^2 + m_p^2 \approx 4yE_e E_e' - Q^2 + m_p^2.$$

The kinematical range of positron-proton scattering at HERA is shown in Figure 2.2 in the  $W_{\gamma p}$ - $Q^2$ -plane. The solid line bounds the kinematically allowed region, where the line at  $W_{\gamma p} = m_p$  corresponds to elastic scattering. The behaviour for constant  $x$  is marked by the dotted lines and for constant  $y$  by the dashed ones.

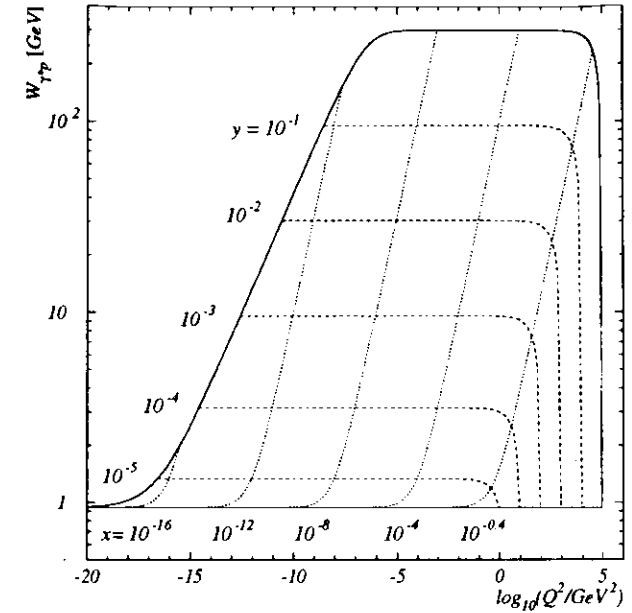


Figure 2.2: The kinematical range at HERA in the  $W_{\gamma p}$ - $Q^2$ -plane. The solid line bounds the kinematically allowed region, where the line at  $W_{\gamma p} = m_p$  corresponds to elastic scattering. The dashed lines correspond to constant  $y$  and the dotted lines to constant  $x$ .

### 2.1.2 The Electromagnetic Cross Section

Any cross section can be determined by

$$d\sigma = \frac{|T|^2 d\rho}{\Phi},$$

where  $d\rho$  is the phase space of the outgoing system,  $T$  is the matrix element of the reaction and  $\Phi$  is the flux of the incoming particles.

In  $ep$  scattering we have in good approximation  $\Phi \approx 2s$ . The phase space in the  $ep$  reaction is described in terms of the scattered positron. Therefore it can be written as:

$$d\rho = \frac{d^3 k'}{(2\pi)^3 2E_e'} = \frac{1}{4(2\pi)^2} dy dQ^2.$$

The matrix element in the one-photon-exchange approximation is given by:

$$|T|^2 = \frac{16\pi^2\alpha^2}{Q^4} L^{\mu\nu} 4\pi m_p W_{\mu\nu}.$$

The leptonic tensor  $L^{\mu\nu}$  describes the positron vertex (after averaging and summing over the spins of the incoming and outgoing lepton, respectively):

$$L^{\mu\nu} = 2 \left( k'^{\mu} k^{\nu} + k'^{\nu} k^{\mu} - \frac{Q^2}{2} g^{\mu\nu} \right). \quad (2.2)$$

The hadronic tensor  $W^{\mu\nu}$  describes the proton vertex and can be written as:

$$W^{\mu\nu} = \frac{1}{4\pi m_p} \sum_{X, \text{spins}} M^{\mu} M^{*\nu} (2\pi)^4 \delta(P' - P - q), \quad (2.3)$$

where the sum runs over all final states  $X$  and the spins of the incoming proton.  $M^{\mu} = \langle X | \mathcal{J}^{\mu} | p \rangle$  is the transition matrix element for the hadronic part of the interaction, where  $\mathcal{J}^{\mu}$  denotes the electromagnetic current.

The conservation of current requires  $q_{\mu} W^{\mu\nu} = q_{\nu} W^{\mu\nu}$  and the vector nature of the electromagnetic current restricts  $W^{\mu\nu}$  to consist only of parity-even terms. The hadronic tensor reduces therefore to:

$$W^{\mu\nu} = W_1(y, Q^2) \cdot \left( -g^{\mu\nu} - \frac{q^{\mu} q^{\nu}}{Q^2} \right) + \left( P^{\mu} + \frac{(P \cdot q) q^{\mu}}{Q^2} \right) \left( P^{\nu} + \frac{(P \cdot q) q^{\nu}}{Q^2} \right) \frac{W_2(y, Q^2)}{m_p^2}, \quad (2.4)$$

introducing two structure functions  $W_1(y, Q^2)$  and  $W_2(y, Q^2)$ .

Evaluating the matrix element using equations (2.2) and (2.4), the differential  $ep$  cross section in  $y$  and  $Q^2$  becomes:

$$\begin{aligned} \frac{d^2\sigma^{ep}}{dydQ^2} &= \frac{1}{2s} \frac{16\pi^2\alpha^2}{Q^4} 4\pi m_p \left[ 2W_1 Q^2 \left( 1 - \frac{2m_p^2}{Q^2} \right) + W_2 \frac{s^2}{m_p^2} \left( 1 - y - \frac{xy m_p^2}{s} \right) \right] \frac{1}{4(2\pi)^2} \\ &= \frac{4\pi\alpha^2}{Q^4} \left[ y \left( 1 - \frac{2m_p^2}{Q^2} \right) x F_1(y, Q^2) + \frac{1}{y} \left( 1 - y - \frac{xy m_p^2}{s} \right) F_2(y, Q^2) \right], \end{aligned} \quad (2.5)$$

where the proton structure functions, defined as:

$$F_1(y, Q^2) = m_p W_1(y, Q^2), \quad F_2(y, Q^2) = \nu W_2(y, Q^2) \quad (2.6)$$

have been introduced.

## 2.2 Photoproduction

Photoproduction is the reaction of real photons on protons. In  $ep$  scattering in the limit of very small  $Q^2$ , the virtuality of the exchanged photon, the process can be related to photoproduction.

### 2.2.1 Relating $ep$ and $\gamma p$ Cross Sections

Directly HERA only offers to measure the  $ep$  cross section. By applying some additional formalism one can convert the  $ep$  into a  $\gamma p$  cross section.

In the following two subsections we restrict ourselves to the proton restframe, where  $\nu$  gives the photon energy, i.e. we have  $q = (\nu, \vec{K})$ , where  $\vec{K}$  is the momentum of the photon. The photon flux is then  $4m_p K$  with  $K = |\vec{K}|$ . The cross section for real photons on protons can therefore be written as:

$$\sigma_T^{\gamma p} = \frac{4\pi^2\alpha}{K} \epsilon_i^{\mu} \epsilon_i^{*\nu} W_{\mu\nu}, \quad (2.7)$$

making use of the hadronic tensor (2.3).  $\epsilon_i$  is the polarization vector of the photon with helicity  $i$ .

To derive the cross section for virtual photons, some additional considerations have to be done. In the virtual case the photons are no longer only transversely polarized, they can also have longitudinal polarization. Defining  $\vec{K}$  to be along the  $Z$ -axis, the polarization vectors are:

$$\text{transversely polarized:} \quad \epsilon_{\pm 1} = \frac{1}{\sqrt{2}} (0, 1, \pm i, 0), \quad (2.8)$$

$$\text{longitudinally polarized:} \quad \epsilon_0 = \frac{1}{\sqrt{Q^2}} (\sqrt{\nu^2 + Q^2}, 0, 0, \nu). \quad (2.9)$$

Another problem is the flux of virtual photons. It is not uniquely defined as in the case of real photons. There exist two approaches: the one due to Gilman [8] treats the virtual photon like any real particle. Therefore the flux is proportional to:

$$K_{\text{Gilman}} = \sqrt{\nu^2 + Q^2} = \nu \sqrt{1 + \frac{4m_p^2}{ys} x}, \quad (2.10)$$

the momentum of the virtual photon. The second and more conventional approach due to Hand [9] requires the momentum  $\vec{K}$  of the virtual photon to be equal to the energy of a real photon needed to give the same centre-of-mass energy, i.e.  $W_{\gamma^* p}^2 = m_p^2 + 2K_{\text{Hand}} m_p$ :

$$K_{\text{Hand}} = \frac{-Q^2 + 2m_p\nu}{2m_p} = \nu(1 - x). \quad (2.11)$$

Both approaches reduce to  $K = \nu$  for  $Q^2 \rightarrow 0$  as required for real photons.

Using equations (2.8) and (2.9) together with the definition of the flux and equation (2.4) for the hadronic tensor, one can evaluate equation (2.7), yielding the total transverse and longitudinal part of the  $\gamma^* p$  cross section:

$$\begin{aligned} \sigma_T^{\gamma^* p} &= \frac{\sigma_{+1}^{\gamma^* p} + \sigma_{-1}^{\gamma^* p}}{2} = \frac{4\pi^2\alpha}{K} W_1 \\ \sigma_L^{\gamma^* p} &= \sigma_0^{\gamma^* p} = \frac{4\pi^2\alpha}{K} \left[ \left( 1 + \frac{\nu^2}{Q^2} \right) W_2 - W_1 \right] \end{aligned}$$

In photoproduction we have typically small Bjorken- $x$  and therefore we can make some useful approximations. In both the Hand and the Gilman convention, equations (2.10) and (2.11),  $K$

is reduced to  $K \rightarrow \nu$ . Further  $\nu^2/Q^2 \gg 1$  in the photoproduction kinematic range and therefore  $1 + \nu^2/Q^2 \approx \nu^2/Q^2$ . This yields:

$$\begin{aligned}\sigma_T^{\gamma^*p} &= \frac{4\pi^2\alpha}{\nu} W_1 = \frac{4\pi^2\alpha}{m_p\nu} F_1, \\ \sigma_L^{\gamma^*p} &= \frac{4\pi^2\alpha}{\nu} \left( \frac{\nu^2}{Q^2} W_2 - W_1 \right) = \frac{4\pi^2\alpha}{Q^2} F_2 - \frac{4\pi^2\alpha}{m_p\nu} F_1,\end{aligned}$$

where the structure functions from (2.6) have been used. Inverting these relations one gets:

$$xF_1 = \frac{Q^2}{8\pi^2\alpha} \sigma_T^{\gamma^*p}, \quad F_2 = \frac{Q^2}{4\pi^2\alpha} (\sigma_T^{\gamma^*p} + \sigma_L^{\gamma^*p}). \quad (2.12)$$

Using the definition (2.1) of  $Q_{mn}^2$  and neglecting  $m_p^2/s$ , equation (2.5) can be rewritten as:

$$\frac{d^2\sigma^{\gamma^*p}}{dydQ^2} = \frac{4\pi\alpha^2}{Q^4} \left[ \left( y - 2\frac{1-y}{y} \frac{Q_{mn}^2}{Q^2} \right) xF_1(y, Q^2) + \frac{1-y}{y} F_2(y, Q^2) \right].$$

Finally, inserting the results given by equation (2.12) yields the wanted relation between  $ep$  and  $\gamma p$  cross sections, valid in the range of small  $x$  and  $Q^2$ :

$$\frac{d^2\sigma^{\gamma^*p}}{dydQ^2} = \frac{\alpha}{2\pi} \frac{1}{Q^2} \left[ \left( \frac{1+(1-y)^2}{y} - 2\frac{1-y}{y} \frac{Q_{mn}^2}{Q^2} \right) \sigma_T^{\gamma^*p}(y, Q^2) + 2\frac{1-y}{y} \sigma_L^{\gamma^*p}(y, Q^2) \right]. \quad (2.13)$$

### 2.2.2 Vector Meson Dominance Model

The first experiments on the scattering of photons on protons done in the 60's showed remarkable similarities between photon-proton and purely hadronic interactions. A possible way of understanding this behaviour was the assumption of a structured nature of the photon. This means, that the photon appears as a superposition of two different states: a bare photon  $|\gamma_B\rangle$ , which represents the photon known from purely electromagnetic interactions, and a hadronic component  $|h\rangle$ , which was expected to be of order  $\sqrt{\alpha}$  smaller than the bare part. That is, the physically observed photons can be expressed as:

$$|\gamma\rangle = \sqrt{Z_3} |\gamma_B\rangle + \sqrt{\alpha} |h\rangle,$$

where  $\sqrt{Z_3}$  secures the correct normalization of  $|\gamma\rangle$ . Conservation laws require that the hadronic states  $|h\rangle$  must have the same quantum numbers as the photon, i.e.  $J^{PC} = 1^{--}$  and  $Q = B = S = 0$ . Phenomenologically, the photoproduction of light vector mesons  $\rho^0$ ,  $\omega$  and  $\phi$  suggest that they are the major contribution to  $|h\rangle$ , as suggested in Figure 2.3. The restrictive assumption, that these vector mesons are the only hadronic representatives of the photon and that the bare photon  $|\gamma_B\rangle$  does not interact with the proton at all, is the hypothesis of the vector meson dominance model (VDM). It is based on Sakurai's theory of a strong interaction mediated by vector fields, describing the coupling strength by a universal constant  $f_V$  [10]. A later generalization included more constituents than  $\rho^0$ ,  $\omega$  and  $\phi$ , which is referred to as generalized vector dominance (GVD) [11].

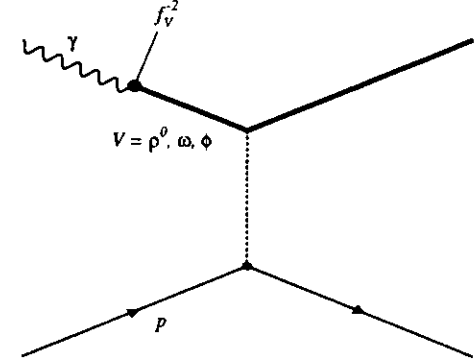


Figure 2.3: Schematic view of the VDM understanding of  $\gamma p$  interactions.

Using the VDM assumptions it is possible to make some quantitative predictions for the  $\gamma p$  cross sections. If we assume  $|h\rangle$  to consist of states of mass  $m$  we have [12]:

$$\sqrt{\alpha} |h\rangle = -(2\pi)^3 \int \frac{dm^2}{m^2 + Q^2} \mathcal{S} |K, m, n\rangle \langle K, m, n | \mathcal{H} | \gamma_B \rangle,$$

where  $|K, m, n\rangle$  is a hadronic state with momentum  $K$  and internal labels  $n$ ,  $|\gamma_B\rangle$  is the hadronic vacuum together with the bare photon of momentum  $K$  and energy  $\nu$ , and  $\mathcal{H}$  is the interaction Hamiltonian density. In this context  $\mathcal{S}$  means the sum and integrals over all suitable labels in  $|K, m, n\rangle$ .

Using the simple VDM assumption, that  $|K, m, n\rangle \sim |V\rangle$ , where  $|V\rangle$  is the appropriate state of one of the vector mesons  $\rho^0$ ,  $\omega$  or  $\phi$  and denoting the  $\gamma \leftrightarrow V$  coupling by the constant  $f_V$ , we finally get (see [12] for the details):

$$\sqrt{\alpha} |h\rangle = \sum_{V=\rho^0, \omega, \phi} \frac{m_V^2}{m_V^2 + Q^2} \cdot \frac{1}{f_V} |V\rangle. \quad (2.14)$$

The determination of the coupling constant  $f_V$  is discussed in Section 2.3.5.

### The $Q^2$ -dependence of the $\gamma^* p$ Cross Section

Let  $M$  be the matrix element for photoabsorption on a proton and  $\mathcal{M}$  that for the absorption of a vector meson by a proton. Then equation (2.14) yields:

$$M = \sum_{V=\rho^0, \omega, \phi} \frac{m_V^2}{m_V^2 + Q^2} \cdot \frac{1}{f_V} \mathcal{M}. \quad (2.15)$$

Using equations (2.3) and (2.7), we have for the transverse and longitudinal  $\gamma^*p$  cross sections in terms of  $M$ , where  $M_{\perp}$  is the matrix element corresponding to the current perpendicular to the photon's four-momentum and  $M_{\parallel}$  is the same for the current parallel to the photon's four-momentum:

$$\begin{aligned}\sigma_T^{\gamma^*p} &= \frac{4\pi^2\alpha}{K} \sum_{X, \text{spins}} |M_{\perp}|^2 \frac{1}{4\pi m_p} (2\pi)^4 \delta(P' - P - q), \\ \sigma_L^{\gamma^*p} &= \frac{4\pi^2\alpha}{K} \frac{Q^2}{\nu^2} \sum_{X, \text{spins}} |M_{\parallel}|^2 \frac{1}{4\pi m_p} (2\pi)^4 \delta(P' - P - q).\end{aligned}$$

The cross sections for the  $Vp$  process are accordingly ( $q = (\nu, \vec{K})$  is used as the vector meson's four-momentum and  $m_V$  as its mass):

$$\begin{aligned}\sigma_T^{Vp} &= \frac{\pi}{K} \sum_{X, \text{spins}} |M_{\perp}|^2 \frac{1}{4\pi m_p} (2\pi)^4 \delta(P' - P - q), \\ \sigma_L^{Vp} &= \frac{\pi}{K} \frac{m_V^2}{\nu^2} \sum_{X, \text{spins}} |M_{\parallel}|^2 \frac{1}{4\pi m_p} (2\pi)^4 \delta(P' - P - q).\end{aligned}$$

Combining these relations using equation (2.15) yields the  $Q^2$  dependence of  $\sigma_T^{\gamma^*p}$  and  $\sigma_L^{\gamma^*p}$ :

$$\sigma_T^{\gamma^*p}(W, Q^2) = \sum_{V=\rho^0, \omega, \phi} \frac{4\pi\alpha}{f_V^2} \left(1 + \frac{Q^2}{m_V^2}\right)^{-2} \sigma_T^{Vp}(W), \quad (2.16)$$

$$\sigma_L^{\gamma^*p}(W, Q^2) = \sum_{V=\rho^0, \omega, \phi} \frac{4\pi\alpha}{f_V^2} \left(1 + \frac{Q^2}{m_V^2}\right)^{-2} \frac{Q^2}{m_V^2} \xi \sigma_T^{Vp}(W), \quad (2.17)$$

where  $W$  denotes the centre-of-mass energy. The factor  $\xi$  is the ratio of the longitudinal to the transverse  $Vp$  cross section and is of  $\mathcal{O}(1)$  [13]. Arguments based on the additive quark model require  $\xi = 1$ . Measurements based on the  $Q^2$ -dependence of the total photoproduction cross section suggest  $\xi = 1$  [14]. Measurements based on helicity of elastically photoproduced vector mesons suggest smaller values [15]. In the following we will keep to the common practice and use  $\xi = 1$ .

### 2.2.3 Classification of the Processes

The processes appearing in photoproduction reactions are usually divided into two subclasses: events with jet-like structures are called hard photoproduction and are not of major importance to the present analysis. The remaining part has usually small transverse momenta, i.e. a soft scale, and is named soft photoproduction. It is described in the following.

#### Soft Photoproduction

The low momentum transfers in soft photoproduction prevent a perturbative calculation of these processes in QCD<sup>1</sup>. The description of these processes has therefore a more phenomenological

<sup>1</sup>Only the production of  $J/\Psi$  mesons could yet be determined via pQCD (see [16]) due to the meson's high mass.

approach. A quite successful ansatz to describe soft  $\gamma p$  interactions is the above discussed vector meson dominance model.

Common to a big part of  $\gamma p$  interactions is the so called soft diffractive behaviour. The naming originates from the analogy to the diffraction of light ("optical model" [17]) observed first in hadron-hadron interactions [18]. This means, that the energy dependence of the process is weak (i.e. the total and differential cross sections vary slowly with energy) and the scattering amplitude has a sharp forward peak. The different event shapes led to the following classification, where  $V$  stands for  $\rho^0, \omega, \phi$ :

- Elastic diffraction:  $\gamma p \rightarrow Vp$ , as shown in Fig. 2.4(a). It is the simplest kind of diffractive interaction and therefore closer to the classical analogon than any other process. It is discussed in detail in Section 2.3.
- Dissociative diffraction. In this type of process at least one of the incoming particles dissociates into a higher mass state  $N$  or  $X$  (with  $m_N > m_p$  or  $m_X > m_V$ , respectively). This class is subdivided into:
  - proton dissociation:  $\gamma p \rightarrow VN$ , as shown in Fig. 2.4(b);
  - photon dissociation:  $\gamma p \rightarrow Xp$ , as shown in Fig. 2.4(c);
  - double dissociation:  $\gamma p \rightarrow XN$ , as shown in Fig. 2.4(d).

The cross section dependence on the mass of the dissociated system is expected to be:

$$\frac{d\sigma}{dm_{X(N)}^2} \sim \frac{1}{(m_{X(N)}^2)^a}$$

with  $a \approx 1$ , which is confirmed by experiment (see e.g. [18]).

The remaining part of reactions is usually referred to as non-diffractive or minimum-bias, usually parametrized as a simple hadronic interaction. Characteristic for this kind of interaction is the impossibility to attach parts of the final state to the incoming photon and proton.

### 2.3 Elastic Vector Meson Photoproduction

One of the most important applications of VDM is the explanation of elastic elastic vector meson photoproduction. In these events the vector meson which the incoming photon fluctuates into, appears in the final state (process (a) in the above listing). At HERA, the vector meson production corresponds to the reaction:

$$e + p \rightarrow e' + V + p' \quad (2.18)$$

as shown in Figure 2.5. Here  $V$  denotes the produced vector meson.

The detection of the vector meson in the final state allows a simplification in the determination of the kinematical variables. In photoproduction at ZEUS the median value of  $Q^2$  is small. Therefore the virtual exchanged photon is emitted with negligible transverse momentum and with longitudinal momentum  $p_{Z\gamma} \approx -E_\gamma$ , where  $E_\gamma$  is the photon energy. Using these assumptions,

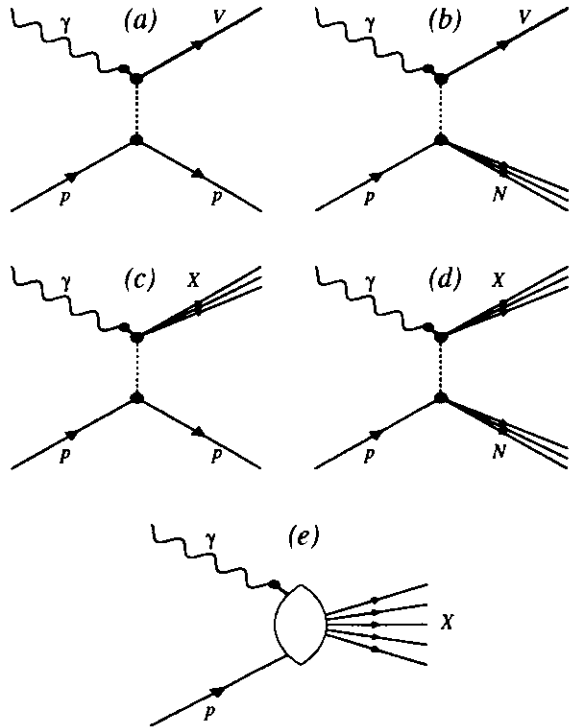


**Figure 2.4:** Classification of the VDM processes: (a) elastic diffraction. (b) proton dissociative diffraction. (c) photon dissociative diffraction. (d) double dissociative diffraction. (e) non-diffractive process.

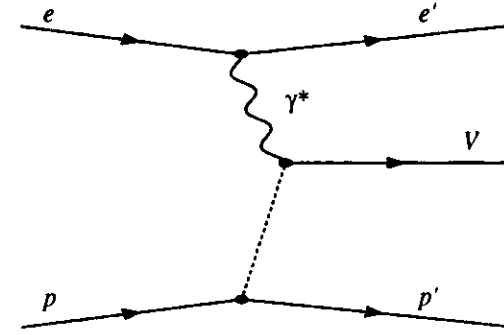


**Figure 2.5:** Schematic diagram of elastic vector meson production in  $ep$  interactions.

$y$  and  $W_{\gamma,p}$  can be expressed by the energy  $E_V$  and the longitudinal and transverse momentum  $p_{zV}$  and  $p_{TV}$  of the vector meson in the laboratory frame, where  $m_V$  is the vector meson mass:

$$W_{\gamma,p}^2 \approx 4E_\gamma E_p \approx 2(E_V - p_{zV})E_p \quad (2.19)$$

$$\begin{aligned} y &\approx E_\gamma/E_e \\ &\approx (E_V - p_{zV})/2E_e \end{aligned} \quad (2.20)$$

Another important variable is the squared momentum transfer at the hadronic vertex  $t = (P - P')^2 = (q - V)^2$ , where  $V$  denotes the four-momentum of the vector meson. Using the above approximations we have:

$$\begin{aligned} t &= -Q^2 - 2q \cdot V + m_V^2 \\ &\approx -2E_\gamma(E_V + p_{zV}) + m_V^2 \\ &\approx -(E_V^2 - p_{zV}^2) + m_V^2 \\ &= -p_{TV}^2 \end{aligned} \quad (2.21)$$

For kinematical reasons, the value  $t = 0$  is not accessible because a minimum momentum transfer is necessary to provide the invariant mass for the transition  $\gamma \rightarrow V$ . Therefore we have:

$$-t \geq \frac{m_V^4}{4\nu^2} \approx \frac{m_V^4 m_p^2}{W^4}$$

In the kinematical range at HERA this lower limit is of order  $10^{-8} \text{ GeV}^2$  and can safely be set to zero in the following.

### 2.3.1 Calculation of the $\gamma p \rightarrow Vp$ Cross Section

In the special case of elastic vector meson photoproduction, the relation between the  $ep$  and the virtual  $\gamma p$  cross section  $\sigma^{\gamma p}$  in equation (2.13) can be further simplified by using the results of Section 2.2.2. The sum in equations (2.16) and (2.17) reduces to the addend corresponding to the produced vector meson:

$$\sigma_T^{\gamma^* p \rightarrow Vp}(W_{\gamma p}, Q^2) = \left(1 + \frac{Q^2}{m_V^2}\right)^{-2} \sigma^{\gamma p \rightarrow Vp}(W_{\gamma p}) \quad (2.22)$$

$$\sigma_L^{\gamma^* p \rightarrow Vp}(W_{\gamma p}, Q^2) \approx \left(1 + \frac{Q^2}{m_V^2}\right)^{-2} \frac{Q^2}{m_V^2} \sigma^{\gamma p \rightarrow Vp}(W_{\gamma p}) \quad (\xi = 1) \quad (2.23)$$

Here

$$\sigma^{\gamma p \rightarrow Vp}(W_{\gamma p}) = \sigma_T^{\gamma^* p \rightarrow Vp}(W_{\gamma p}, Q^2 = 0) = \frac{4\pi\alpha}{f_V^2} \sigma_T^{Vp \rightarrow Vp}(W_{\gamma p}), \quad (2.24)$$

the cross section for the elastic production of a vector meson  $V$  with real photons ( $Q^2 = 0$ ) on protons was introduced. Inserting this into equation (2.13) we have:

$$\frac{d^2\sigma^{ep \rightarrow eVp}}{dydQ^2} = \Phi(y, Q^2) \cdot \sigma^{\gamma p \rightarrow Vp}(W_{\gamma p}),$$

where

$$\Phi(y, Q^2) = \frac{\alpha}{2\pi Q^2} \left[ \frac{1 + (1-y)^2}{y} - \frac{2(1-y)}{y} \left( \frac{Q_{\min}^2}{Q^2} - \frac{Q^2}{m_V^2} \right) \right] \left(1 + \frac{Q^2}{m_V^2}\right)^{-2} \quad (2.25)$$

is called the effective photon flux

The  $\gamma p$  cross section for elastic vector meson photoproduction can therefore be determined by evaluating the electroproduction cross section and dividing it by the effective photon flux integrated over the  $y$  and  $Q^2$  ranges covered by the measurement.

### 2.3.2 Cross Section Dependence on $t$

The elastic production of vector mesons is a diffractive process. This means among others that the forward amplitude has a sharp peak. Experimentally this can be seen in the differential cross section in  $|t|$ , which has a strong fall off with  $|t|$  at small values. The fall off for small  $|t|$  is approximately exponential, which is supported by Regge type parametrizations (see Section 2.4.1):

$$\frac{d\sigma^{\gamma p \rightarrow Vp}}{d|t|} = N e^{-b|t|} \quad (2.26)$$

For larger values of  $|t|$  a slightly modified function may be used:

$$\frac{d\sigma^{\gamma p \rightarrow Vp}}{d|t|} = N e^{-b|t| + c|t|^2} \quad (2.27)$$

The exponential behaviour was indeed measured by various experiments on vector meson production (for a summary see e.g. [3]). The slope parameter  $b$  for  $\rho^0$ ,  $\omega$  and  $\phi$  at those experiments was determined to be of order  $5 \dots 10 \text{ GeV}^{-2}$ .

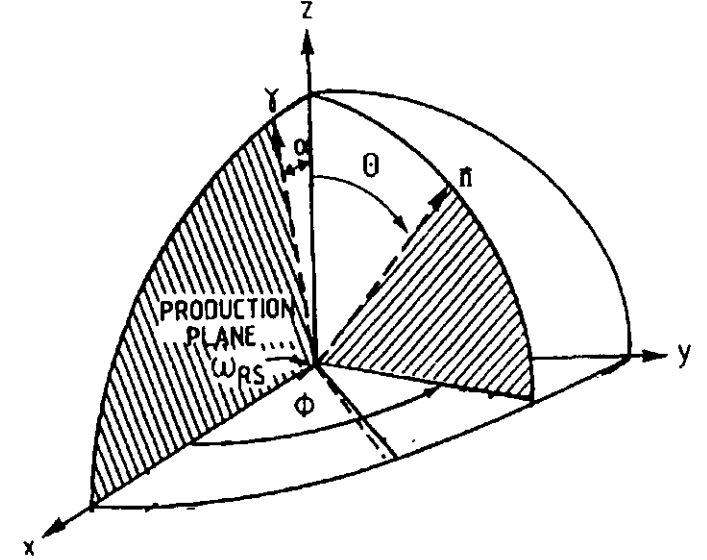


Figure 2.6: Definition of angles in the vector meson restframe used to study the decay [20]  $\vec{n}$  is the analyser of the decay particles (see text).

### 2.3.3 Decay Angular Distributions

The study of the angular distributions of the decay products in the rest frame of vector mesons in elastic photoproduction is a tool for checking production models such as the hypothesis of  $s$ -channel helicity conservation (SCHC), i.e. the fact that the vector meson retains the helicity of the photon. For this study, the coordinate system is defined by:

$$\vec{z} = \frac{-\vec{n}_o}{|\vec{n}_o|}, \quad \vec{y} = \frac{\vec{q} \times \vec{b}}{|\vec{q} \times \vec{b}|}, \quad \vec{x} = \vec{y} \times \vec{z}, \quad (2.28)$$

where  $\vec{n}_o$  is the momentum of the outgoing proton,  $\vec{b}$  the boost axis along the vector meson direction and  $\vec{q}$  the momentum of the incoming photon in the vector meson's rest frame [19]. The angles used for the analysis are the polar and azimuthal angles  $\theta_h$ ,  $\phi_h$  of the analyser in the coordinate system (2.28) as shown in Figure 2.6. If a decay into two particles occurs, the analyser points in the direction of flight of one of the decay particles. For a decay into three particles, the analyser is the normal on the decay plane of the vector meson. The decay angular distribution depends on a third quantity  $\Phi_h$ , which is the angle between the vector meson production plane and the lepton scattering plane. In this analysis neither the outgoing proton nor the outgoing positron is measured. Therefore  $\Phi_h$  is unknown and one has to average over it,  $\cos \theta_h$  and  $\phi_h$  are calculated using the assumption that the photon has  $Q^2 = 0$ . The decay angular distribution



$W(\cos \theta_h, \phi_h)$  in the case of unpolarized incoming positrons and averaged over  $\Phi_h$  can be written in terms of the density matrix elements  $r_{jk}^{04}$  (see Appendix A). Upon averaging over  $\phi_h$  or  $\cos \theta_h$ , respectively one finds for the decay into pseudoscalar particles (upper sign) or for the decay into pseudoscalar and a vectorial particle (lower sign):

$$W(\cos \theta_h) = \frac{3}{4} [1 \mp r_{00}^{04} \pm (3r_{00}^{04} - 1) \cos^2 \theta_h], \quad (2.29)$$

$$W(\phi_h) = \frac{1}{2\pi} [1 \mp 2r_{1-1}^{04} \cos 2\phi_h]. \quad (2.30)$$

In the case of SCHC, the matrix element  $r_{1-1}^{04}$  is expected to be zero. The other matrix element is related to  $R$ , the ratio between the longitudinal and the transverse  $\gamma^*p$  cross section, in case of SCHC by the following equation (see Appendix A):

$$R = \frac{\sigma_{L\gamma^*p}}{\sigma_{T\gamma^*p}} = \frac{1}{\epsilon + \delta} \frac{r_{00}^{04}}{1 - r_{00}^{04}}, \quad (2.31)$$

The present data have  $\epsilon \approx 1$  and  $\delta \approx 0$ , essentially constant over  $W_{\gamma^*p}$  (see Appendix A). For photoproduction events at HERA the longitudinal part of the  $\gamma^*p$  cross section is small and therefore a value of  $r_{00}^{04}$  close to zero is expected.

### 2.3.4 Relation to Hadronic Cross Sections

The cross sections for elastic vector meson photoproduction can be related to hadronic total cross sections using VDM and the optical theorem [1].

The optical theorem allows to relate any elastic cross section to the corresponding total cross section [17]:

$$\left. \frac{d\sigma_{el}}{d|t|} \right|_{t=0} = \frac{1 + \eta^2}{16\pi} \sigma_{tot}^2,$$

where  $\eta$  is the ratio of the real to the imaginary part of the forward scattering amplitude which has been measured to be of the order of 10% [21] and thus can be neglected in the following. Spin effects have been ignored as well. Using the VDM relation between  $\gamma p$  and  $Vp$  cross sections as given by equation (2.24), we have:

$$\left. \frac{\sigma^{\gamma p \rightarrow Vp}}{d|t|} \right|_{t=0} \approx \frac{4\pi\alpha}{f_V^2} \frac{1}{16\pi} (\sigma_{tot}^{Vp})^2. \quad (2.32)$$

Assuming an exponential behaviour of  $\frac{d\sigma}{d|t|} \sim e^{-b|t|}$  as given by equation (2.26), the elastic photoproduction cross section becomes:

$$\sigma^{\gamma p \rightarrow Vp} \approx \frac{1}{b} \left. \frac{\sigma^{\gamma p \rightarrow Vp}}{d|t|} \right|_{t=0} \approx \frac{4\pi\alpha}{f_V^2} \frac{1}{16\pi} \frac{(\sigma_{tot}^{Vp})^2}{b}. \quad (2.33)$$

In the next step we can relate the total  $Vp$  cross sections to those of  $\pi^\pm p$  and  $K^\pm p$  interactions, using the additive quark model [22]:

$$\sigma_{tot}^{p^0} \approx \sigma_{tot}^{-p} \approx \frac{1}{2} (\sigma_{tot}^{\pi^+p} + \sigma_{tot}^{\pi^-p}), \quad (2.34)$$

$$\sigma_{tot}^{\phi p} \approx \sigma_{tot}^{K^+p} + \sigma_{tot}^{K^-p} - \sigma_{tot}^{\pi^-p}. \quad (2.35)$$

The slope  $b$  has to be fixed, too. Again, measurements of  $\pi^\pm p$  and  $K^\pm p$  interactions could be used, assuming  $b(\gamma p \rightarrow \rho^0, \omega p) \approx b(\pi^\pm p)$  and  $b(\gamma p \rightarrow \phi p) \approx b(K^\pm p)$ . While the former approximation fits well to the data of  $\rho^0$  and  $\omega$  photoproduction, the latter is not in good agreement with results from  $\phi$  photoproduction. Thus less precise measurements of the reaction  $\gamma p \rightarrow \phi p$  must be used for  $b(\gamma p \rightarrow \phi p)$  instead. For a detailed discussion see Section 2.4.1.

So finally, the coupling constants have to be determined, which is discussed in the next section.

### 2.3.5 Determination of the $\gamma \leftrightarrow V$ Coupling Constants

The coupling constants  $f_V$  can be determined from  $e^+e^-$  collisions or from photoproduction measurements as described in the following.

#### $e^+e^-$ collisions

The coupling of a virtual photon and a vector meson can be observed using the resonant vector meson production by colliding  $e^+e^-$  beams:

$$e^+e^- \rightarrow \gamma^* \rightarrow V \rightarrow \text{hadrons}. \quad (2.36)$$

The partial width of the resonance, which is equivalent to the  $V \rightarrow e^+e^-$  decay width  $\Gamma(V \rightarrow e^+e^-)$ , is related to the coupling constant  $f_V$  by [3]:

$$\Gamma(V \rightarrow e^+e^-) = \frac{\alpha^2}{3} \left( \frac{f_V^2}{4\pi} \right)^{-1} m_V, \quad (2.37)$$

where  $m_V$  is the mass of the vector meson.

The width  $\Gamma(V \rightarrow e^+e^-)$  as well as  $m_V$  were determined by various collider experiments by measuring the cross section of reaction (2.36). The global mean values as determined by the Particle Data Group (PDG) [23] are given in Table 2.1. The coupling constants were calculated using these values together with equation (2.37). The results are summarized in the central column of Table 2.3.

#### Photoproduction

Measurements of the elastic photoproduction of vector mesons can also be used to derive the photon-vector meson coupling constant.

The coupling constants are given by the above relation (2.32) between the photoproduction cross sections and the hadronic total cross sections. But as the slope  $b$  can be parametrized and the integrated photoproduction cross section is measured more precise than the differential cross section in  $t$ , equation (2.33) is used instead:

$$\frac{f_{\rho^0}^2}{4\pi} = \frac{\alpha}{16\pi} \frac{(\sigma_{tot}^{\pi^+p} + \sigma_{tot}^{\pi^-p})^2}{4b\sigma^{\gamma p \rightarrow \rho^0 p}},$$

$$\frac{f_{\omega}^2}{4\pi} = \frac{\alpha}{16\pi} \frac{(\sigma_{tot}^{\pi^+p} + \sigma_{tot}^{\pi^-p})^2}{4b\sigma^{\gamma p \rightarrow \omega p}}.$$

$$\frac{f_\phi^2}{4\pi} = \frac{\alpha}{16\pi} \frac{(\sigma_{\text{tot}}^{K^+p} + \sigma_{\text{tot}}^{K^-p} - \sigma_{\text{tot}}^{\pi^+p})^2}{b \sigma^{\gamma p \rightarrow \phi p}}$$

The values used for the total  $\pi^\pm p$  and  $K^\pm p$  cross sections were taken from a parametrization of measurements at centre-of-mass energies  $W$  below 20 GeV [2]. The values for the slope  $b$  are taken from  $d\sigma/d|t|$  measurements as discussed in detail in Section 2.4.1. The photoproduction cross sections are taken from measurements for  $W_{\gamma p} > 9$  GeV [24, 25, 26, 27, 28, 29]. All used values as well as the resulting coupling constants are listed in Table 2.2. The weighted means of the coupling constants are listed in the last column of Table 2.3.

### Comparison

When comparing the results from  $e^+e^-$  collisions and from photoproduction, a significant difference between both sets of coupling constants is visible. This effect has been observed earlier [30]. It might be caused by intrinsic uncertainties in VDM – especially if one takes into account that  $e^+e^-$  collisions produce vector mesons on the mass shell while in photoproduction the photons couple to virtual vector mesons – and in addition by the model dependence of the determination of the photoproduction results (assuming the additive quark model and assumptions on the slope  $b$ ).

To be consistent within photoproduction, the corresponding values of the coupling constants, i.e. those given in the last column of Table 2.3, are thus used in the following.

## 2.4 Theoretical Models

### 2.4.1 Regge Theory

#### The Basis of Regge Theory

The basis of Regge theory is the analytical continuation of a scattering amplitude in the complex angular momentum plane [31]. For this purpose, the partial wave formalism is used. It allows to represent any scattering amplitude  $A(s, t)$  by a decomposition according to the angular momentum  $\ell$ :

$$A(s, t) = \sum_{\ell=0}^{\infty} (2\ell + 1) a_\ell(t) P_\ell(z), \quad (2.38)$$

where the  $P_\ell$  are Legendre functions of the first kind as a function of  $z = \cos \theta$ , the cosine of the scattering angle, which itself is a function of  $s$  and  $t$ . The partial wave amplitudes  $a_\ell$  are then given by:

$$a_\ell(t) = \frac{1}{2} \int_{-1}^1 dz P_\ell(z) A(s(z), t). \quad (2.39)$$

The sum in equation (2.38) can be replaced by an integral in the complex  $\ell$  plane along a path  $C_1$ , which encloses the positive part of the real axis (see Figure 2.7):

$$A(s, t) = -\frac{1}{2} \int_{C_1} d\ell (2\ell + 1) a_\ell(t) \frac{P_\ell(z)}{\sin \pi \ell}. \quad (2.40)$$

vector meson	$m_V$	$\Gamma(V \rightarrow e^+e^-)$
$\rho^0$	$768.5 \pm 0.6$ MeV	$6.77 \pm 0.32$ keV
$\omega$	$781.94 \pm 0.12$ MeV	$0.60 \pm 0.02$ keV
$\phi$	$1019.413 \pm 0.008$ MeV	$1.37 \pm 0.05$ keV

**Table 2.1:** The vector meson mass  $m_V$  and the  $e^+e^-$  decay width  $\Gamma(V \rightarrow e^+e^-)$  as global mean of  $e^+e^-$  collision experiments [23] for the light vector mesons  $V = \rho^0, \omega, \phi$ .

vector meson	$\langle W \rangle$	$\sigma^{\gamma p \rightarrow Vp}$	$\sigma^{Vp}$	$b(Vp)$	$\frac{f_V}{4\pi}$
$\rho^0$	9.2 GeV	$9.40 \pm 1.00$ $\mu\text{b}$	23.8 mb	$8.25$ GeV $^{-2}$	$2.72 \pm 0.29$
	11.6 GeV	$9.82 \pm 0.56$ $\mu\text{b}$	23.7 mb	$8.48$ GeV $^{-2}$	$2.52 \pm 0.14$
	12.2 GeV	$8.24 \pm 0.47$ $\mu\text{b}$	23.7 mb	$8.53$ GeV $^{-2}$	$2.99 \pm 0.17$
	14.1 GeV	$9.22 \pm 0.52$ $\mu\text{b}$	23.8 mb	$8.68$ GeV $^{-2}$	$2.64 \pm 0.15$
	14.8 GeV	$8.59 \pm 0.49$ $\mu\text{b}$	23.8 mb	$8.72$ GeV $^{-2}$	$2.83 \pm 0.16$
$\omega$	9.2 GeV	$1.01 \pm 0.29$ $\mu\text{b}$	23.8 mb	$8.25$ GeV $^{-2}$	$25.29 \pm 7.26$
	10.0 GeV	$0.98 \pm 0.20$ $\mu\text{b}$	23.7 mb	$8.33$ GeV $^{-2}$	$25.72 \pm 5.25$
	11.6 GeV	$0.91 \pm 0.24$ $\mu\text{b}$	23.7 mb	$8.48$ GeV $^{-2}$	$27.18 \pm 7.17$
	13.0 GeV	$1.16 \pm 0.14$ $\mu\text{b}$	23.8 mb	$8.59$ GeV $^{-2}$	$21.10 \pm 2.57$
	13.4 GeV	$0.93 \pm 0.16$ $\mu\text{b}$	23.8 mb	$8.62$ GeV $^{-2}$	$26.27 \pm 4.52$
$\phi$	9.2 GeV	$0.61 \pm 0.17$ $\mu\text{b}$	14.1 mb	$6.46$ GeV $^{-2}$	$18.90 \pm 5.61$
	11.6 GeV	$0.65 \pm 0.06$ $\mu\text{b}$	14.7 mb	$6.69$ GeV $^{-2}$	$18.67 \pm 2.67$
	12.2 GeV	$0.65 \pm 0.05$ $\mu\text{b}$	14.8 mb	$6.74$ GeV $^{-2}$	$18.81 \pm 2.44$
	14.1 GeV	$0.66 \pm 0.05$ $\mu\text{b}$	15.2 mb	$6.89$ GeV $^{-2}$	$18.98 \pm 2.46$
	14.8 GeV	$0.63 \pm 0.10$ $\mu\text{b}$	15.3 mb	$6.93$ GeV $^{-2}$	$20.10 \pm 3.82$
	17.2 GeV	$0.74 \pm 0.09$ $\mu\text{b}$	15.7 mb	$7.08$ GeV $^{-2}$	$17.62 \pm 2.83$

**Table 2.2:** Values used to determine  $f_V^2/4\pi$  from measurements of the photoproduction cross section  $\sigma^{\gamma p \rightarrow Vp}$  for the light vector mesons  $V = \rho^0, \omega, \phi$ . Here  $\sigma^{Vp}$  denotes the total  $Vp$  cross section and  $b(Vp)$  the slope of elastic  $Vp$  cross sections.

vector meson	$e^+e^-$ collisions	photoproduction
$\rho^0$	$2.02 \pm 0.10$	$2.69 \pm 0.27$
$\omega$	$23.1 \pm 0.8$	$24.6 \pm 3.8$
$\phi$	$13.2 \pm 0.5$	$18.8 \pm 1.5$

**Table 2.3:** The coupling constants  $f_V^2/4\pi$  for the transition  $\gamma \leftrightarrow V$  for the light vector mesons  $V = \rho^0, \omega, \phi$ . The values given are the results from  $e^+e^-$  collision measurements (2nd column) and photoproduction measurements (last column).

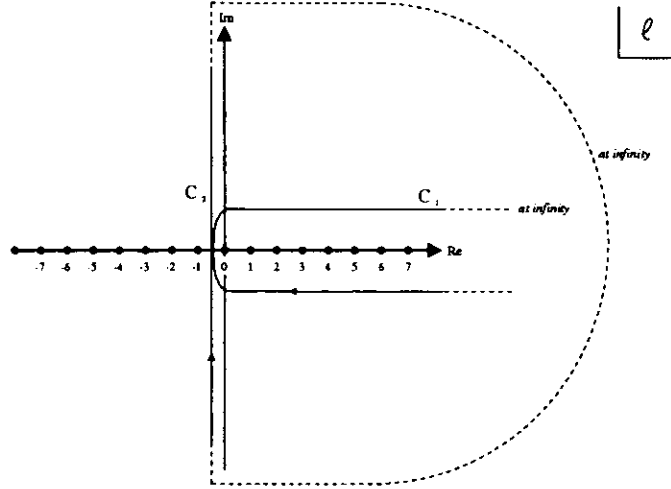


**Figure 2.7:** Integration paths  $C_1$  and  $C_2$  in the complex  $\ell$ -plane as used in equation (2.40) and (2.41).

Using Cauchy's theorem, this reduces to the sum of the residues of the integrand, yielding equation (2.38).

Enlarging now the area covered by the integration path to the whole complex plane with positive real part (path  $C_2$  with  $\text{Re}(\ell) \geq 0$ , see Figure 2.7), poles of  $a_\ell$  will appear in the area surrounded by the path. Let us suppose for simplicity only one pole at  $\ell = \alpha(t)$  with the approximate behaviour  $a_\ell = \beta(t)/(\ell - \alpha(t))$ . Then equation (2.40) becomes:

$$A(s, t) = \pi(2\alpha(t) + 1)\beta(t) \frac{P_{\alpha(t)}(z)}{\sin \pi \alpha(t)} - \frac{1}{2} \int_{C_2} d\ell (2\ell + 1) a_\ell(t) \frac{P_\ell(z)}{\sin \pi \ell}. \quad (2.41)$$

The second term of equation (2.41), called the background integral, behaves like  $\sim s^{-\frac{1}{2}}$  and therefore vanishes for  $s \rightarrow \infty$  [31].

The first term of equation (2.41) is called a Regge pole, a pole in the complex  $\ell$  plane. This contribution:

$$A^{\text{R}}(s, t) = \pi(2\alpha(t) + 1)\beta(t) \frac{P_{\alpha(t)}(z)}{\sin \pi \alpha(t)} \quad (2.42)$$

to the amplitude can itself be decomposed into partial waves using equation (2.39). The partial wave amplitudes of the Regge pole are:

$$\begin{aligned} a_\ell^{\text{R}}(t) &= \frac{1}{2} \int_{-1}^1 dz P_\ell(z) A^{\text{R}}(s, t) \\ &= \frac{(2\alpha(t) + 1)\beta(t)}{(\ell - \alpha(t))(\ell + \alpha(t) + 1)} \stackrel{\ell \rightarrow \alpha(t)}{\sim} \frac{\beta(t)}{\ell - \alpha(t)}, \end{aligned}$$

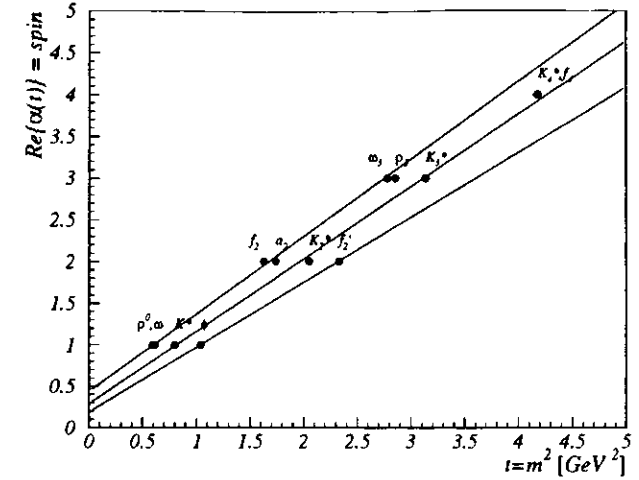


**Figure 2.8:** Chew-Frautschi plot for some mesons. The lines are linear fits and correspond to Regge trajectories. The data were taken from [23].

with  $\ell$  now being an integer again. Decomposing  $\alpha(t)$  into its real and imaginary part:

$$\alpha(t) = \alpha_R(t) + i\alpha_I(t)$$

and defining  $t_r$  to be the point where  $\alpha_R(t_r) = \ell$ , one can approximate:

$$\alpha(t) = \ell + \alpha_R'(t_r)(t - t_r) + \dots + i\alpha_I(t_r) + i\alpha_I'(t_r)(t - t_r) + \dots$$

Therefore  $a_\ell^{\text{R}}$  becomes for  $\alpha_R \approx \ell$ , assuming  $\alpha_I' \ll \alpha_R'$  [31]:

$$a_\ell^{\text{R}}(t) \approx \frac{\beta(t_r)/\alpha_R'(t_r)}{t_r - t - i\alpha_I(t_r)/\alpha_R'(t_r)}$$

This is the Breit-Wigner formula for a resonance of mass  $m_r = \sqrt{t_r}$  and width  $\Gamma_r = \frac{\alpha_I(t_r)}{\alpha_R'(t_r)m_r}$ . Indeed, if one plots the spin versus the squared mass  $t = m^2$  of particles ("Chew-Frautschi plot"), the points seem to line up on trajectories  $\alpha(t)$ , as shown in Figure 2.8 for some known mesons. The Chew-Frautschi plot suggests a linear behaviour of  $\alpha(t)$ . The points were fitted with the approximation:

$$\alpha(t) = \alpha(0) + \alpha' t, \quad (2.43)$$

which is in good agreement with the data. For the highest lying trajectory ( $\rho^0$ ,  $\omega$ ,  $f_2$ , etc.) a linear fit yields [32]:

$$\alpha_{\rho^0, \omega, \dots}(t) = 0.44 + 0.93 \text{ GeV}^{-2} t.$$

Summarizing, the dominant contribution to the scattering amplitude at large  $s$  is from Regge poles and is given by equation (2.42). It can be seen as an interaction mediated by Regge trajectories  $\alpha(t)$  ("Reggeons") formed by resonances.

### Cross Sections

For the determination of a cross section, the scattering amplitude has to be evaluated in the  $s$ -channel region, i.e. for  $t < 0$ . Usually  $|t| \ll s$ , which allows to use the asymptotic behaviour of  $P_{\alpha(t)}$  at large  $s$ :

$$P_{\alpha(t)} \approx e^{-i\pi\alpha(t)} \cdot \left(\frac{s}{s_0}\right)^{\alpha(t)}$$

Therefore equation (2.42) becomes:

$$A^{\mathbf{R}}(s, t) \approx F(t) \cdot \left(\frac{s}{s_0}\right)^{\alpha(t)}, \quad (2.44)$$

where  $F(t)$  includes the part of  $A^{\mathbf{R}}$  not depending on  $s$ .

The differential elastic cross section  $d\sigma_{el}/dt$  can be determined via the scattering amplitude:

$$\frac{d\sigma_{el}}{d|t|} = \frac{|A|^2}{16\pi s^2}. \quad (2.45)$$

The optical theorem [17] gives for the total cross section  $\sigma_{tot}$ :

$$\sigma_{tot} = \frac{1}{s} \text{Im}\{A(t=0)\}. \quad (2.46)$$

Inserting equation (2.44) yields:

$$\sigma_{tot}(s) \sim \left(\frac{s}{s_0}\right)^{\alpha(0)-1} \quad (2.47)$$

and:

$$\frac{d\sigma_{el}}{d|t|} \sim |F(t)|^2 \left(\frac{s}{s_0}\right)^{2\alpha(t)-2}. \quad (2.48)$$

Assuming  $|F(t)|^2 \sim e^{b_0 t}$  for small  $|t|$  [31] and making the linear approximation (2.43), equation (2.48) can be written as:

$$\begin{aligned} \frac{d\sigma_{el}}{d|t|} &\approx N \cdot e^{(2\alpha_0 - 2 + 2\alpha' t) \cdot \ln(s/s_0) + b_0 t} \\ &= \left. \frac{d\sigma_{el}}{d|t|} \right|_{t=0} \cdot e^{-b|t|}, \end{aligned} \quad (2.49)$$

with:

$$b := b_0 + 2\alpha' \ln(s/s_0). \quad (2.50)$$

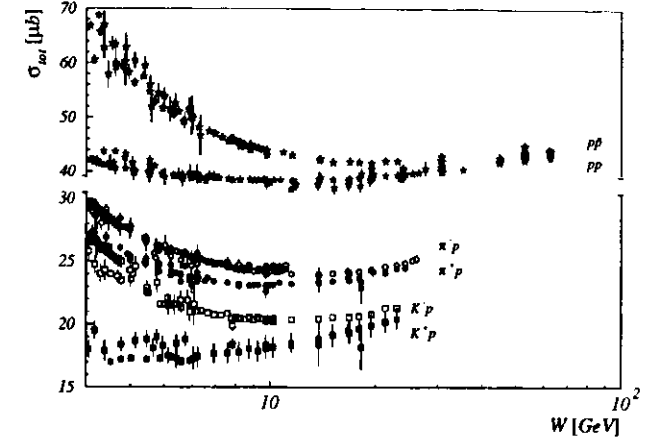


**Figure 2.9:** Total cross sections for different particles on the proton versus the centre-of-mass energy  $W = \sqrt{s}$  [33]. Common is a slight increase with energy above about 10 GeV.

**The Pomeron** Some total high-energy cross sections are plotted in Figure 2.9. They are roughly constant, slightly rising at centre-of-mass energies above about 10 GeV. As can be seen from equation (2.47), explanation by Reggeon exchange requires  $\alpha(0) \approx 1$ , but all trajectories from known particles have  $\alpha(0) < 1$ . Further, the exchanged particle must have the quantum numbers of the vacuum. To cope with this difficulty, a new trajectory was postulated, called the Pomeron  $\mathbb{P}$ , with  $\alpha_{\mathbb{P}}(0) = 1 + \epsilon$  and  $0 < \epsilon \ll 1$ . Assuming again a linear behaviour of the trajectory we have:

$$\alpha_{\mathbb{P}} = 1 + \epsilon + \alpha'_{\mathbb{P}} t.$$

Fits to  $pp$  and  $p\bar{p}$  data with these assumptions using the  $s$  behaviour of  $\sigma_{tot}$  and  $d\sigma/dt$  led to  $\epsilon = 0.08$  and  $\alpha'_{\mathbb{P}} = 0.25 \text{ GeV}^{-2}$  [32], while a recent measurement of the  $p\bar{p}$  total cross section at a large centre-of-mass energy [34] requires a larger value for  $\epsilon$ . A recent re-evaluation of fits similar to those in [32] including new measurements yields an intercept  $\epsilon$  of 0.096; it is claimed that the fits agree with an  $\epsilon$  within 0.07 and 0.11 [35].

### Predictions for Elastic Vector Meson Production

As discussed in Section 2.3.4, the elastic  $\gamma p \rightarrow Vp$  cross section can be determined from the total  $Vp$  cross section, see equation (2.33). The latter is expected to behave as given by equation (2.47). In addition, the total  $Vp$  cross sections can be determined from hadronic cross sections as given by equations (2.34) and (2.35). As experimental results for  $\pi^{\pm}p$  and  $K^{\pm}p$  cross sections exist,

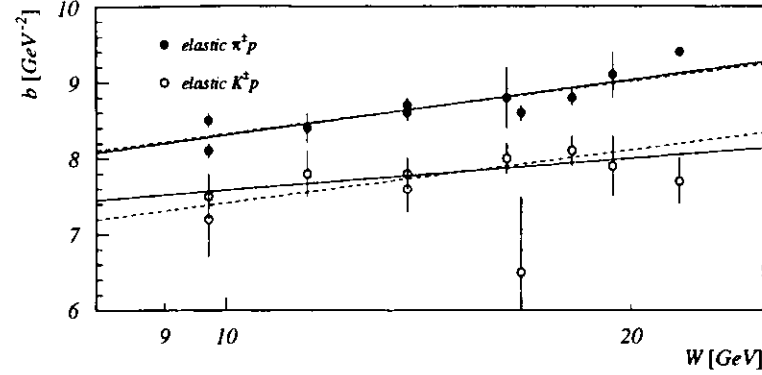


**Figure 2.10:** Exponential slope parameter  $b$  of  $d\sigma/d|t|$  as measured in elastic  $\pi^\pm p$  and  $K^\pm p$  reactions [37]. The solid line shown is a fit to the slope parameter according to equation (2.52) with  $b_0$  and  $\alpha'_{\text{IP}}$  as parameters, while the dashed lines show fits with  $b_0$  as parameters and  $\alpha'_{\text{IP}} = 0.25 \text{ GeV}^{-2}$  as measured in  $pp$  and  $p\bar{p}$  collisions.

one can apply a fit to them, using the behaviour predicted by Regge theory. Fits of the type:

$$\sigma_{\text{tot}}^{AB} = X^{AB} s^\epsilon + Y^{AB} s^{-\eta} \quad (2.51)$$

were applied [2], where the first term corresponds to Pomeron exchange, the second to an exchange of a Reggeon. The exponents  $\epsilon$  and  $\eta$  were not subject to these fits but were fixed using the result from fits to  $pp$  and  $p\bar{p}$  data for  $\sqrt{s} > 10 \text{ GeV}$ :  $\epsilon = 0.0808$  and  $\eta = 0.4525$ .

The Regge prediction given by equation (2.50) is used for the slope parameter  $b$ . Together with the assumption  $s_0 = 1/\alpha'_{\text{IP}}$  [36] and setting  $W_{\gamma p}^2 = s$  one has, if Pomeron exchange dominates:

$$b = b_0 + 2\alpha'_{\text{IP}} \ln(\alpha'_{\text{IP}} W_{\gamma p}^2). \quad (2.52)$$

The value of  $b_0$  can be estimated assuming  $b(\gamma p \rightarrow \rho^0, \omega p) \approx b(\pi^\pm p)$  and  $b(\gamma p \rightarrow \phi p) \approx b(K^\pm p)$  and using measurements of elastic  $\pi^\pm p$  and  $K^\pm p$  cross sections. Measurements of  $d\sigma/d|t|$  for these processes [37] at centre-of-mass energies between 9.7 and 21.7 GeV yielded the slope parameters  $b$  shown in Figure 2.10. They were fitted with a function according to equation (2.52) as shown by the solid lines in Figure 2.10, yielding

$$\left. \begin{aligned} b_0 &= 6.60 \pm 0.37 \text{ GeV}^{-2} \\ \alpha'_{\text{IP}} &= 0.26 \pm 0.04 \text{ GeV}^{-2} \end{aligned} \right\} \text{for } \pi^\pm p$$

$$\left. \begin{aligned} b_0 &= 6.78 \pm 0.88 \text{ GeV}^{-2} \\ \alpha'_{\text{IP}} &= 0.15 \pm 0.10 \text{ GeV}^{-2} \end{aligned} \right\} \text{for } K^\pm p$$

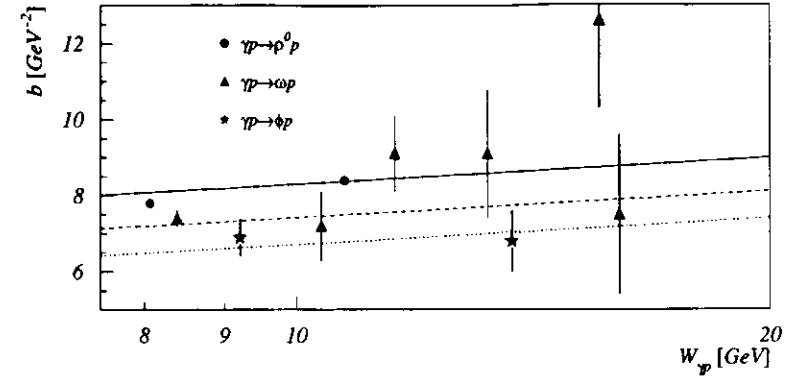


**Figure 2.11:** Exponential slope parameter  $b$  of  $d\sigma/d|t|$  as measured in the reaction  $\gamma p \rightarrow Vp$  with  $V = \rho^0, \omega, \phi$ . The lines describe the behaviour given by equation (2.52). The solid line was fixed by the  $b_0$  derived from  $\pi^\pm p$  measurements, while the dashed line was fixed by the  $b_0$  derived from  $K^\pm p$  measurements. The dotted line was fixed by the  $\phi$  photoproduction results.

which is in good agreement with the above given value of  $\alpha'_{\text{IP}} = 0.25 \text{ GeV}^{-2}$ . As the latter value is much more precise than that from the  $\pi^\pm p$  and  $K^\pm p$  measurements, a fit with fixed  $\alpha'_{\text{IP}} = 0.25 \text{ GeV}^{-2}$  was applied as shown in Figure 2.10 by the dashed lines, yielding:

$$b_0 = 6.72 \pm 0.04 \text{ GeV}^{-2} \text{ for } \pi^\pm p \quad (2.53)$$

$$b_0 = 5.81 \pm 0.09 \text{ GeV}^{-2} \text{ for } K^\pm p \quad (2.54)$$

For comparison, the slopes predicted by the latter fit are compared with results from the photoproduction of the light vector mesons  $V = \rho^0, \omega, \phi$  [25, 26, 27, 28, 29] in Figure 2.11. The behaviour given by equation (2.52) and fixed by the  $b_0$  from equation (2.53) agrees well with the results from the photoproduction of  $\rho^0$  and  $\omega$  mesons and thus are used in the following. The expected similarity between  $\phi$  photoproduction and  $K^\pm p$  data (dashed line) is not seen. Therefore the mean of the  $\phi$  photoproduction measurements [28, 29] has to be used, which is less precise:

$$b_0 = 5.1 \pm 0.5 \text{ GeV}^{-2} \text{ for } \gamma p \rightarrow \phi p. \quad (2.55)$$

The results of the fits to the total cross section, using equations (2.33), (2.34) and (2.35) and  $s = W_{\gamma p}^2$  together with the results given by equations (2.53) and (2.55) and the  $f_V$  as given by the last column of Table 2.3, yield:

$$\sigma^{\gamma p \rightarrow \rho^0 p} = \frac{(5.07 W_{\gamma p}^{0.1616} + 11.83 W_{\gamma p}^{-0.9050})^2}{6.0 + \ln W_{\gamma p}}, \quad (2.56)$$

$$\sigma^{\gamma p \rightarrow \omega p} = \frac{(1.768W_{\gamma p}^{0.1616} + 3.93W_{\gamma p}^{-0.9050})^2}{6.0 + \ln W_{\gamma p}}, \quad (2.57)$$

$$\sigma^{\gamma p \rightarrow \phi p} = \frac{(1.42W_{\gamma p}^{0.1616} - 0.22W_{\gamma p}^{-0.9050})^2}{4.4 + \ln W_{\gamma p}}, \quad (2.58)$$

with  $\sigma$  being in  $\mu\text{b}$  and  $W_{\gamma p}$  in GeV. These predictions are expected to hold for  $W_{\gamma p} > 10\text{ GeV}$ . The cross sections are plotted versus  $W_{\gamma p}$  in Figure 2.12 (solid lines) together with some measurements of  $\sigma^{\gamma p \rightarrow V p}$  at low energy [33] and recent HERA measurements [5, 6, 38, 39].

The parametrizations of the  $\pi^\pm p$  and  $K^\pm p$  cross sections used to derive equations (2.56), (2.57) and (2.58) have two essential defects: they do not give any estimate of the uncertainty of the fits and they do not take into account recent measurements of hadronic cross sections which suggest a higher value of the Pomeron intercept than used in [2]. As discussed above, a recent analysis of  $\bar{p}p$  and  $pp$  data including also these new measurements yields  $\epsilon = 0.096$  [35]. They also claim that the fits give a good  $\chi^2$  in the range  $0.07 < \epsilon < 0.11$ . Thus the fits according to equation (2.51) were repeated for  $\pi^\pm p$  and  $K^\pm p$  data [33] using  $\epsilon = 0.096$  and the previous  $\eta$ -value ( $\eta = 0.4525$ )<sup>2</sup>. The values  $\epsilon = 0.07$  and  $\epsilon = 0.11$  were also fitted to give an estimate of the uncertainty of the model<sup>3</sup>. The results of the fits, taking into account that  $X^{AB} = X^{\bar{A}\bar{B}}$ , are listed in Tables 2.4 and 2.5 together with the  $\chi^2$  of the fit. The number of degrees of freedom was 115 for  $\pi^\pm p$  data and 61 for  $K^\pm p$  data. The results are plotted together with the data versus  $W = \sqrt{s}$  in Figure 2.13.

Using these parametrizations, the cross sections of elastic vector meson photoproduction can be determined again. The results are plotted in Figure 2.12 as dashed lines. The shaded areas show the uncertainty estimated by varying  $\epsilon$  in the range  $[0.07, 0.11]$ .

#### 2.4.2 The Model of Wu et al.

##### The Basis of the Model

The model by Wu et al. describes the diffractive scattering of two hadrons. The attempt is to base the description on general considerations from quantum field theory only. In this model, one of the particles is seen from the other as a "thin pancake", having the following characteristics [40]:

- It has a black core with a radius which expands logarithmically with  $s$ . The absorption in this core is essentially complete.
- A grey or partially absorptive fringe surrounds the core having a radius of order unity (independent of  $s$ ).

The amplitude for the elastic diffractive scattering of a hadron  $h$  on the proton is then given by:

$$A_h^W(s, t) = \frac{is}{2\pi} \int d\mathbf{p} e^{-i\mathbf{q}\cdot\mathbf{p}} \left(1 - e^{-\Omega_h(s, \mathbf{p})}\right), \quad (2.59)$$

<sup>2</sup>The contribution of the term  $s^{-\eta}$  from Reggeon exchange is negligible at high  $s$  and the prediction thus does not depend considerably on the choice of  $\eta$ .

<sup>3</sup>Though the  $\pi^\pm p$  and  $K^\pm p$  data seem to exclude already the value  $\epsilon = 0.07$  it was nevertheless used to provide an error estimate on the lower side of  $\epsilon$  for photoproduction cross sections.

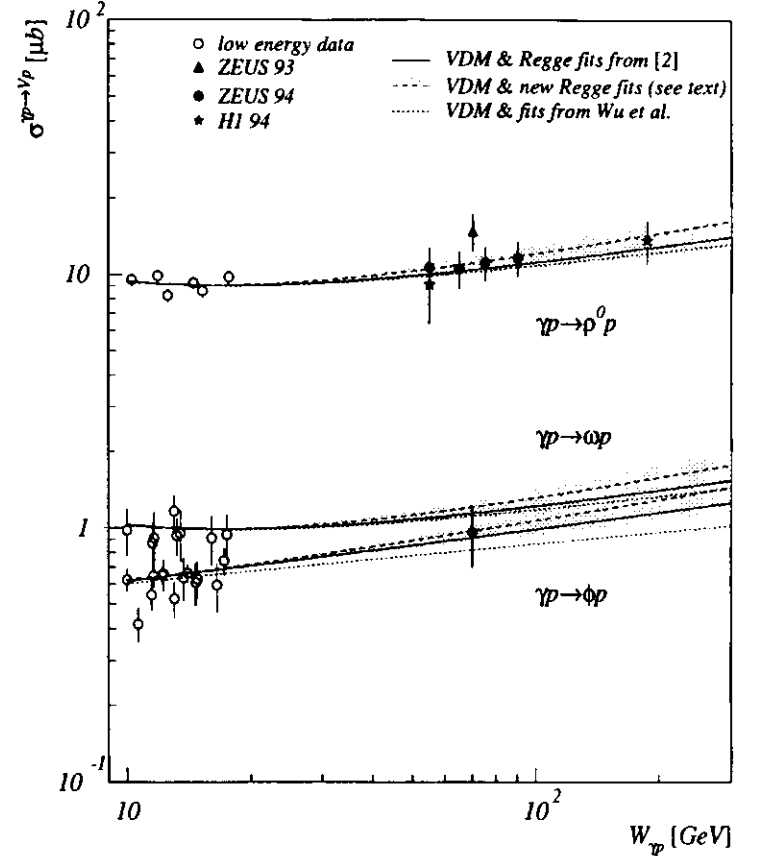


**Figure 2.12:** Predictions for  $\gamma p \rightarrow V p$  cross sections versus  $W_{\gamma p}$  together with some results from measurements at low  $W_{\gamma p}$  [33] and recent measurements of H1 [38] and ZEUS [5, 6, 39]. Solid lines: predictions from Regge type fits to hadronic data from [2] in combination with VDM; dashed lines: re-evaluated Regge type fits to hadronic data (see text) in combination with VDM where the shaded area gives the uncertainty on the cross section estimated by the uncertainty of the Pomeron intercept; dotted lines: prediction from the model of Wu et al. fitted to hadronic data in combination with VDM.

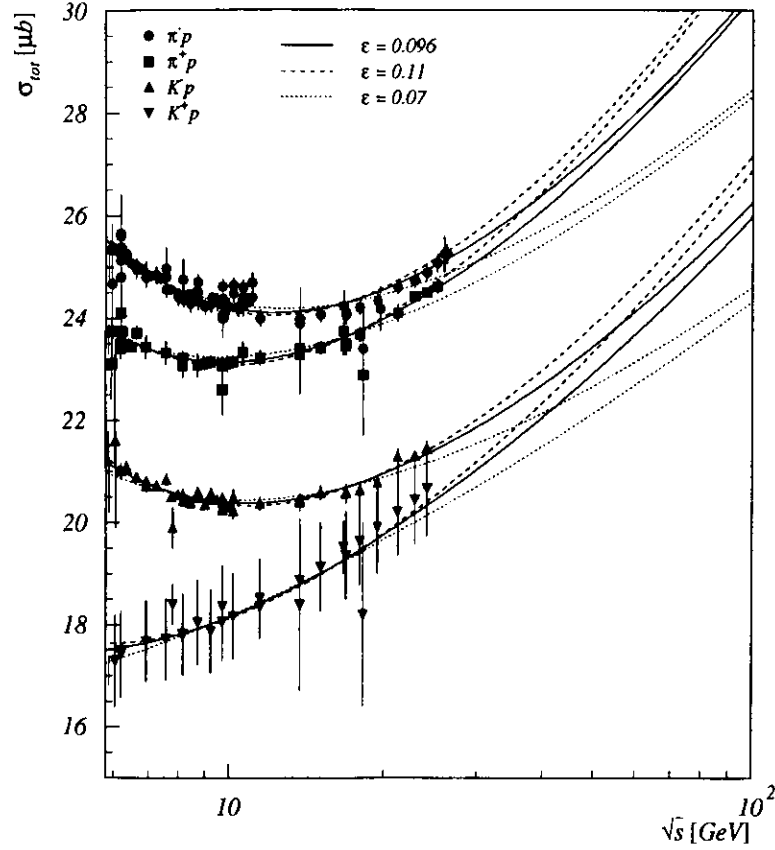


Figure 2.13: Results from fits to  $\pi^\pm p$  and  $K^\pm p$  data according to equation (2.51) for different values of the Pomeron intercept  $\alpha_{\mathbb{P}}(0) = 1 + \epsilon$  as shown by the curves compared to the data (symbols).

$\epsilon$	$X^{\pi^\pm p}$	$Y^{\pi^\pm p}$	$\chi^2$
0.07	$14.67 \pm 0.03$	$32.46 \pm 0.27$ $24.03 \pm 0.33$	133
0.096	$12.30 \pm 0.02$	$40.70 \pm 0.25$ $32.15 \pm 0.32$	111
0.11	$11.19 \pm 0.02$	$44.84 \pm 0.25$ $36.23 \pm 0.31$	139

Table 2.4: Results from fits to  $\pi^\pm p$  data according to equation (2.51) for different values of the Pomeron intercept  $\alpha_{\mathbb{P}}(0) = 1 + \epsilon$ . The upper row for  $Y^{\pi^\pm p}$  is the result for  $\pi^- p$  while the lower one gives that for  $\pi^+ p$ .

$\epsilon$	$X^{K^\pm p}$	$Y^{K^\pm p}$	$\chi^2$
0.07	$12.73 \pm 0.04$	$23.10 \pm 0.41$ $4.80 \pm 0.78$	66
0.096	$10.65 \pm 0.03$	$30.73 \pm 0.39$ $12.70 \pm 0.77$	35
0.11	$9.67 \pm 0.03$	$34.56 \pm 0.38$ $16.67 \pm 0.76$	30

Table 2.5: Results from fits to  $K^\pm p$  data according to equation (2.51) for different values of the Pomeron intercept  $\alpha_{\mathbb{P}}(0) = 1 + \epsilon$ . The upper row for  $Y^{K^\pm p}$  is the result for  $K^- p$  while the lower one gives that for  $K^+ p$ .

with  $t = -q^2$ . The opacity parameter of the ‘‘pancake’’ is:

$$\Omega_h(s, \mathbf{p}) = -f_h \left( E e^{-\frac{t}{2}} \right)^c e^{-\lambda(p^2 + x_{oh}^2)^{1/2}},$$

where  $E$  is the energy of particle  $h$  in the proton rest frame,  $c$ ,  $\lambda$  are some universal constants and  $f_h$ ,  $x_{oh}$  are constants depending on the particle  $h$ . Equation (2.59) can be reduced to [41]:

$$A_h^W(s, t) = i s \int_0^\infty J_0(p\sqrt{-t}) \left( 1 - e^{-\Omega_h(s, \mathbf{p})} \right) p dp,$$

where  $J_0$  is the Bessel function of order zero. The constants were fixed using measurements of  $\pi^\pm p$ ,  $K^\pm p$ ,  $pp$  and  $p\bar{p}$  reactions [40].

Total hadronic cross sections can thus be determined using equation (2.46) together with the above amplitude. To allow for contributions from non-diffractive processes to the cross section, a background term proportional to  $s^{-1/2}$  has to be considered [40]:

$$\sigma_{tot} = a_h s^{-1/2} + \frac{1}{s} \text{Im}\{A_h^W(t=0)\}, \quad (2.60)$$

where  $a_h$  are constants again fixed by hadronic measurements.

#### Predictions for Elastic Vector Meson Production

Using equations (2.33), (2.34) and (2.35), the cross section for elastic photoproduction of vector mesons can be derived from the above model. Again, the results from fits to  $d\sigma/d|t|$  as given by

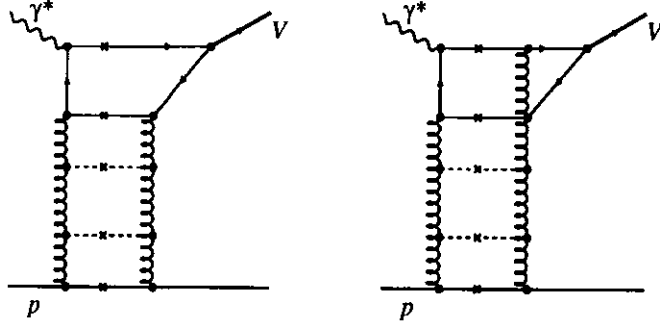


**Figure 2.14:** Feynman diagrams of the gluon ladders used for the perturbative calculation of elastic vector meson production [16].

equations (2.53) and (2.55) are used. Together with the values of  $f_V$  as given by the last column of Table 2.3, the cross sections for elastic photoproduction of vector mesons were derived from equation (2.60). They are shown in Figure 2.12 (dotted lines) as a function of  $W_{\gamma p}$ .

### 2.4.3 The Model of Ryskin

The Ryskin model describes elastic vector meson production using perturbative QCD techniques. It was first developed for elastic  $J/\psi$  photoproduction [16]. In this model, the photon interacts with the proton as a  $q\bar{q}$  pair. The Pomeron mediating this interaction is described as a gluon ladder as shown in Figure 2.14.

In the leading-log approximation used here, the whole system of ladder diagrams is used. Thus the amplitude is proportional to the gluon momentum density in the proton  $xG$ . The cross section was evaluated to:

$$\frac{d\sigma^{\gamma^* p \rightarrow V p}}{dt} = [F_N^{2G}(t)]^2 \frac{\alpha_s \Gamma_{e^+}^V m_V^3}{3\alpha} \pi^3 \left[ \bar{x}G(\bar{x}, \bar{q}^2) \frac{2\bar{q}^2 p_T^2}{(2\bar{q}^2)^3} \right]^2 \left( 1 + \frac{Q^2}{m_V^2} \right), \quad (2.61)$$

with the electromagnetic width of the vector meson decay,  $\Gamma_{e^+}^V$ , and the electromagnetic and strong coupling constants,  $\alpha$  and  $\alpha_s$ . The variables  $\bar{x}$ , the fraction of the proton's momentum carried by the two gluons, and  $\bar{q}^2$ , the squared four-momentum of the gluons, have been used,

which are defined as:

$$\bar{x} = \frac{m_V^2 + Q^2 + p_T^2}{W_{\gamma p}^2}$$

and:

$$\bar{q}^2 = \frac{m_V^2 + Q^2 + p_T^2}{4}$$

$F_N^{2G}(t)$  in equation (2.61) can be approximated by the electromagnetic proton form factor which is given by  $F_N^{em}(t) = \frac{1}{(1-t/0.71 \text{GeV}^2)^2}$  [16].

The evaluation of equation (2.61) requires a hard scale (a large mass  $m_V$  or more general  $\bar{q} \gg 0$ ) which is true for  $J/\psi$  photoproduction. As this is not fulfilled for the photoproduction of the light vector mesons  $\rho^0$ ,  $\omega$  and  $\phi$ , equation (2.61) is not expected to hold necessarily.



## Chapter 3

# Experimental Conditions

### 3.1 HERA

The hadron electron ring accelerator HERA [42] is the first and only particle collider providing high energy collisions of electrons (positrons) with protons. It has a total circumference of 6.3 km. The beams collide at two interaction points in the centre of the H1 [43] and ZEUS detectors, the latter being described below. In 1994 and 1995 the electron (positron)<sup>1</sup> beam is used with an energy of 27.5 GeV, while the proton beam has an energy of 820 GeV, providing a centre-of-mass energy of  $\sqrt{s} = 300$  GeV.

The particles are stored in bunches which collide in intervals of 96 ns. In 1994, typically 153 colliding bunches were stored, together with 17 unpaired proton and 15 unpaired positron (electron) bunches. In 1995, typically 174 colliding bunches were stored, together with 6 unpaired proton and 15 unpaired positron bunches. Aside the  $ep$  collisions reactions of particles of either beam with remaining gas in the beam pipe occur ("beam-gas interactions"). To estimate the background from these reactions, the unpaired bunches were used.

### 3.2 The ZEUS Detector

ZEUS is a multi-task detector designed to measure  $ep$  interactions at HERA. The detector in longitudinal and cross section is shown in Figures 3.1 and 3.2. The coordinate system has positive  $Z$  in the direction of flight of the beam protons and the  $X$ -axis is horizontal, pointing towards the centre of HERA. The nominal interaction point is at  $X = Y = Z = 0$ .

The main parts of the ZEUS detector relevant to this analysis are:

- An assembly of tracking chambers in the inner part, surrounded by
- the high-resolution calorimeter,
- the hadron-electron separator implemented in the calorimeter,

<sup>1</sup>Since summer 1994 positrons instead of electrons have been used

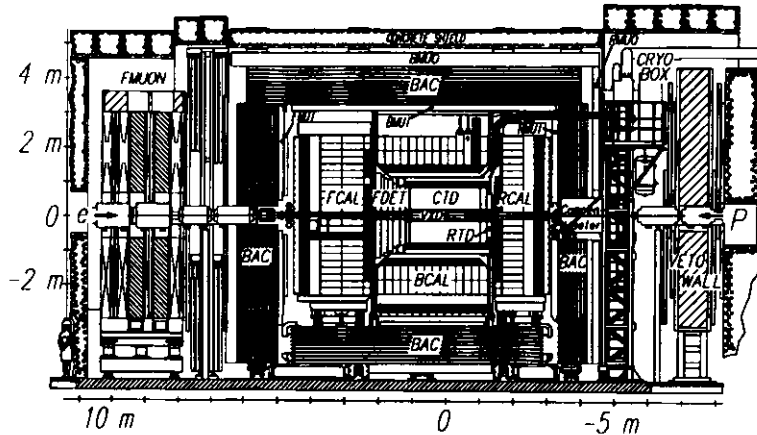


Figure 3.1: View of the ZEUS detector in longitudinal section.

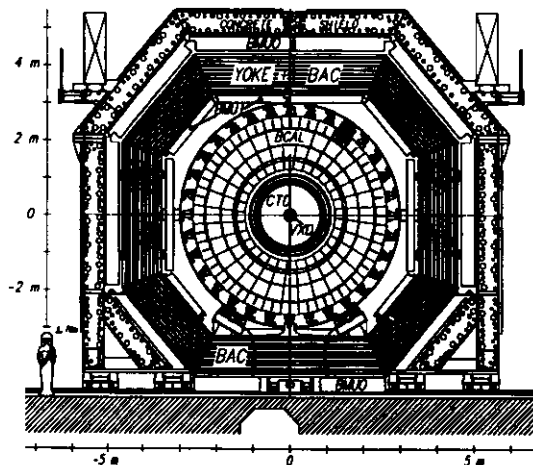


Figure 3.2: View of the ZEUS detector in cross section.

- a luminosity detector,
- background monitors,
- a veto wall.

These components are described in the following. A detailed description of the complete detector can be found elsewhere [44].

### 3.2.1 The Calorimeter

The ZEUS calorimeter (CAL) is a sampling calorimeter built of alternating layers of depleted uranium and plastic scintillator [45]. It is a so called compensating calorimeter, i.e. the energy response on electrons and hadrons is the same. This was achieved by adjusting the relative thickness of uranium and scintillator layers.

The calorimeter is divided into three parts, the forward (FCAL), barrel (BCAL) and rear (RCAL) calorimeter. They cover the polar angle regions of  $2.6^\circ$  to  $36.7^\circ$ ,  $36.7^\circ$  to  $129.1^\circ$ , and  $129.1^\circ$  to  $176.2^\circ$ , respectively. This gives a solid angle coverage of 99.8% in the forward and 99.5% in the rear region. Each part consists of modules, which are transversely divided into towers. The towers are longitudinally subdivided into an electromagnetic (EMC) and a hadronic (HAC) section. A view of an FCAL module showing its structure is shown in Figure 3.3. The smallest unit in the calorimeter is a cell. The transverse size of a cell in the EMC is  $5 \times 20 \text{ cm}^2$  in FCAL and BCAL or  $10 \times 20 \text{ cm}^2$  in RCAL. HAC cells have a transverse size of  $20 \times 20 \text{ cm}^2$ .

The resolution of the calorimeter was obtained from test beam data. For electrons it is  $\sigma_E/E = 0.18/\sqrt{E}$  and for hadrons it is  $\sigma_E/E = 0.35/\sqrt{E}$ , where  $E$  is in GeV.

Due to material between the interaction point and the surface of CAL, the energy measured by CAL is systematically smaller than the original particle energy. In order to measure the energy loss, in 1995 presamplers in front of FCAL and RCAL were implemented [46]. Each consists of a layer of  $20 \times 20 \text{ cm}^2$  scintillator pads. Particles showering already in the material in front of the F/RCAL lead to an enhanced particle multiplicity, thus allowing, in combination with the CAL information, a correction of the energy measurement.

### 3.2.2 The Hadron Electron Separator

The hadron electron separator (HES) was designed to identify electrons in hadronic showers in the CAL, using the different shower behaviour of electrons and hadrons [47].

The longitudinal size of an electromagnetic shower can be parametrized in units of the radiation length  $X_0$ . The average radiation length in the EMC section of CAL is  $X_0 = 0.74 \text{ cm}$  [45]. The longitudinal size of a hadronic shower is given in terms of the hadronic interaction length  $\lambda$ , the average interaction length of the EMC section of CAL being  $\lambda = 21.0 \text{ cm}$  [45]. Therefore electromagnetic and hadronic showers can in principle be distinguished by their longitudinal extension, though misidentification is possible due to statistical fluctuations and overlaps. The HES measures the energy deposited by charged particles near the maximum of an electromagnetic shower, thus providing information about the longitudinal shape, allowing the desired electron-hadron distinction.

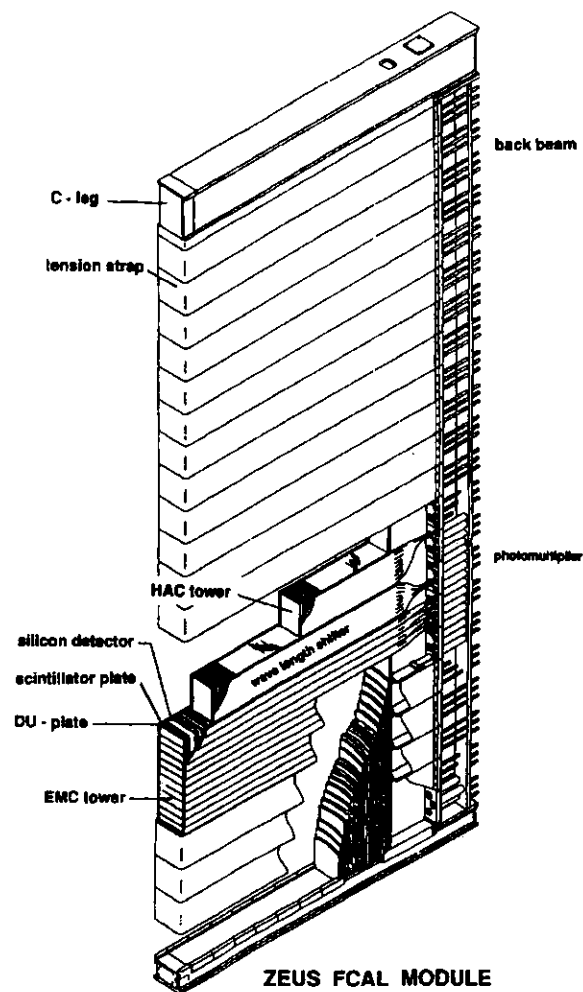


Figure 3.3. View of an FCAL module.

The HES is located in the CAL at a depth of  $3.3X_0$ , which is in the EMC section of RCAL. In 1994 and 1995, only the rear part (RHES), implemented in the RCAL, was operational. The RHES in RCAL as seen from the interaction point is shown in Figure 3.4. It covers an approximately circular area of about  $10\text{m}^2$ .

The RHES consists of  $400\mu\text{m}$  thick silicon detectors. These silicon detectors ("pads") have an active area of  $28.9 \times 30.5\text{mm}^2$ . The cross section of a pad is shown in Figure 3.5. The RHES pads are mounted in pairs on support structures ("skis"). Three of these skis fit into one RCAL module. Thus  $6 \times 3$  pads fit into one RCAL cell of  $20 \times 10\text{cm}$ . The geometrical structure of RHES in RCAL is illustrated in Figure 3.6.

### 3.2.3 Tracking Devices

Charged particles produced in  $ep$  interactions in ZEUS are measured by various tracking devices. Those relevant to this analysis are: the vertex detector (VXD) [49], the central tracking detector (CTD) [50] and the rear tracking detector (RTD) [51].

The VXD is a drift chamber surrounding the outer walls of the beam pipe. It is divided into 120 cells, each equipped with 12 sense wires. The wires are running parallel to the  $Z$ -axis. The purpose of the VXD is to determine the primary as well as secondary vertices and to improve the momentum resolution of the tracking system.

The CTD is a cylindrical wire chamber surrounding the VXD. The wires are arranged in nine cylindrical layers ("superlayers"), each layer being divided into several cells. Five of the superlayers have wires parallel to the  $Z$ -axis, while four have a small angle, chosen such that the resolution in the polar and azimuthal angle is almost equal (about  $1\text{mrad}$ ). The CTD covers a range in the polar angle  $\theta$  of  $15^\circ < \theta < 164^\circ$ .

The RTD is a planar drift chamber located at the rear end of the CTD. It consists of three layers of drift cells, each having six sense wires. The cells are mounted such that the wire direction is rotated by  $120^\circ$ . The RTD provides an angular resolution of about  $1\text{mrad}$  and extends the covered polar angular region to the rear:  $162^\circ < \theta < 170^\circ$ .

All three chambers work in a solenoidal magnetic field of  $1.43\text{T}$ . Their combined information is used to determine momentum, charge and energy loss  $dE/dx$  of charged particles, as well as the position of the primary vertex of any event. The momentum resolution is  $\sigma_{p_T}/p_T = \sqrt{(0.005 \cdot p_T)^2 + (0.016)^2}$ . The resolution in the position of the primary vertex is  $1.4\text{cm}$  in  $Z$  and  $0.2\text{cm}$  in the transverse plane.

### 3.2.4 Luminosity Measurement

The luminosity of  $ep$  collisions at ZEUS is determined via the Bethe-Heitler bremsstrahlung process [52]:

$$ep \rightarrow e\gamma p.$$

The cross section of this process is well known from QED calculations. Therefore a precise measurement of the photon rate allows a precise determination of the luminosity.

The photon of the Bethe-Heitler process, emitted under a small angle with respect to the beam axis, escapes the proton beam pipe through a Cu-Be window at  $Z = -92.5\text{m}$  and is detected in

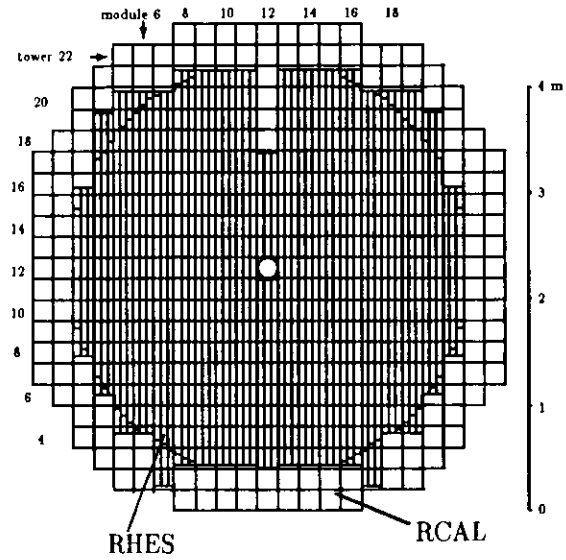


Figure 3.4: A schematic view of the RHES in RCAL.

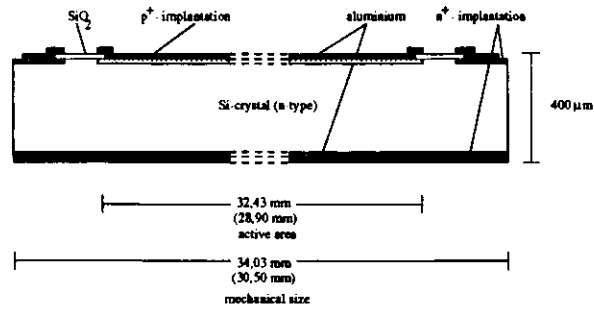


Figure 3.5: Structure of a silicon pad. The given dimensions correspond to the  $y$ -direction ( $x$ -direction) [48]

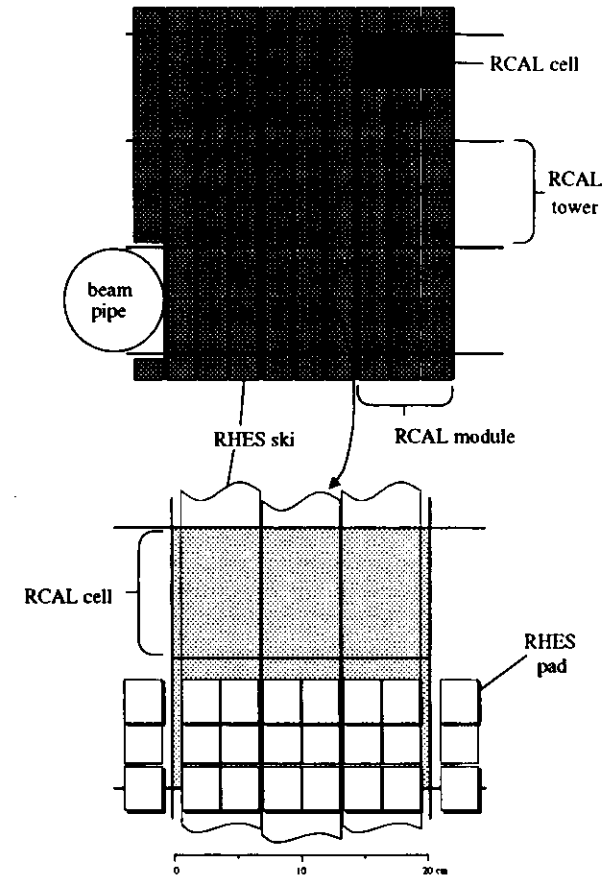


Figure 3.6: Geometrical structure of RHES.

a lead scintillator sampling calorimeter at  $Z = -106$  m.

### 3.2.5 Background Monitors and Veto Wall

Background monitors ("C5-counter") [53] are located at  $Z = -3.15$  m to detect background from interactions of the proton beam with remaining gas in the beam pipe ("p-gas interaction"). The C5-counter is an assembly of scintillators separated by lead sheets positioned orthogonal to the beam pipe. To reject noise and very low energetic particles, signals are accepted only if they occur in the scintillators on both sides of a lead sheet. The timing information of these signals is used to distinguish p-gas interactions from ep collisions.

The veto wall (VW) [54] is located at  $Z = -7.27$  m. It is a  $800 \times 900 \times 87$  cm<sup>3</sup> iron wall which is sandwiched by two layers of scintillator. The VW shields the main detector against p-gas background entering the interaction region. If particles are not completely absorbed, the timing information from signals in the two scintillator sheets is again used to identify and reject the corresponding p-gas event.

### 3.3 The Trigger for ZEUS

In addition to ep collisions several background reactions occur in HERA. The most important sources are: interaction of the beams with remaining gas molecules in the beam pipe and cosmic rays. As the rate of the ep collisions is small compared to that of the background, a trigger system is needed to select those events which are of interest to the physics analysis [55].

The ZEUS trigger is divided into three levels. It reduces the rate at the input of 10 to 100 kHz to an output rate of about 5 Hz. As the events occur in time intervals of 96 ns, the data are stored in 5  $\mu$ s buffers, the so called pipelines, to allow the trigger to decide within this time.

The first level trigger (FLT) is a hardware trigger. Each component providing information at this level has its own trigger. They send their decision to the global first level trigger (GFLT) which makes a decision based on the global information. It must reduce the rate to values below 1 kHz. If the GFLT accepts, the buffers are read and the event is passed to the second level trigger (SLT). Again, each component has its own trigger system using transputers working on an enlarged sample of the measured information. Similar to the FLT, the results are combined at the global second level trigger (GSLT). It reduces the rate to at most 100 Hz. If an event is kept by the GSLT, it is passed to the event builder, which combines the complete information from the various components into a single event record. This is passed to the third level trigger (TLT), which makes a decision based on the complete information. The events accepted by the TLT are written to tape.

## Chapter 4

### Identification of Neutral Pions

The observation of the  $\omega$  meson, which is the topic of the next chapter, is carried out via the major decay mode into  $\pi^+\pi^-\pi^0$ . While the charged pions are easily detected in the tracking chambers, the identification of the neutral pion needs a more elaborate procedure.

The  $\pi^0$  meson is a particle decaying only electromagnetically. The mean life time is small ( $8.4 \pm 0.6 \times 10^{-17}$  s, [23]). Its mass is approximately  $m_{\pi^0} = 135$  MeV. In this analysis the  $\pi^0$  meson is identified via its major decay mode,  $\pi^0 \rightarrow \gamma\gamma$ , which has a branching ratio of  $98.798 \pm 0.032\%$  [23]. Thus the  $\pi^0$  is identified by a pair of photons with an invariant mass in the region of  $m_{\pi^0}$ . The photons are detected using the RCAL and the RHES. The necessary preparation of the RHES and RCAL signals is described in Section 4.1. The  $\pi^0$  reconstruction itself is explained in Section 4.2.

#### 4.1 Preparation of RHES and RCAL Signals

In order to use the signals of RCAL and RHES for the  $\pi^0$  identification, cells or pads with signals above a certain threshold are separately combined into clusters. Here a *local* clustering is considered, i.e. an algorithm creating clusters that contain the shower of one or as few as possible particle(s) rather than clusters that contain the showers of jets (*global* clustering).

##### 4.1.1 RCAL

###### Clustering

RCAL clusters ("condensates") contain adjacent RCAL cells; adjacent cells are defined to share at least one side with each other. The clustering is performed in the following steps [56]:

1. RCAL EMC cells with an energy greater than 80 MeV and HAC cells with an energy greater than 120 MeV are placed in a list sorted by their energy. Cells identified as noisy in a data quality analysis are excluded from this list.
2. The first cell in this list, i.e. that with the highest energy, serves as a seed for the first condensate.

3. All cells in the above list adjacent to the seed are included into this condensate. The seed cell as well as its neighbours are marked as being added to a condensate in the list.
4. Cells in the list adjacent to the previous neighbour cells are added to the condensate and marked correspondingly in the list. Cells used in previous steps are not used again. This step is repeated until no further neighbours can be found.
5. The list is scanned for the most energetic cell not used in any condensate which is used as a seed for a new condensate. The procedure starting at the 3rd step is repeated, excluding all cells marked as already used.
6. Step 5 is repeated until all cells in the list are assigned to a condensate.

The sum of the energy of the cells of a condensate is considered as the energy of the condensate itself. Condensates with a total EMC energy less than 100 MeV and a total HAC energy less than 200 MeV are discarded in order to reject signals from the radioactivity of the uranium. As electromagnetic showers induced by photons usually deposit energy only in the EMC section of the calorimeter, condensates with an EMC energy less than 90% of the total energy are not considered for the  $\pi^0$  analysis.

### Position Reconstruction

For the reconstruction of the position of an RCAL condensate, a  $3 \times 3$  sub-cluster is selected around the cell with the maximum energy  $E_{max}$ . The energy in the three horizontal or vertical strips are summed up according to the following scheme:

$E_{y_1} \rightarrow$			
$E_{y_2} \rightarrow$		$E_{max}$	
$E_{y_3} \rightarrow$			
	$\uparrow$	$\uparrow$	$\uparrow$
	$E_{x_1}$	$E_{x_2}$	$E_{x_3}$

For the reconstruction of the  $x$  position of the condensate, the imbalance values<sup>1</sup> of the cells are used to determine the  $x$  position  $x_i$  ( $i = 1 \dots 3$ ) of the three vertical strips [57]. Then the weights:

$$w_{x_i} = \max \left( 0, \log \frac{E_{x_i}}{\sum_{i=1}^3 E_{x_i}} + 2.5 \right)$$

are used to derive the  $x$ -position of the condensate:

$$x = \frac{\sum_{i=1}^3 x_i \cdot w_{x_i}}{\sum_{i=1}^3 w_{x_i}}$$

<sup>1</sup>Each cell is read out by two photomultipliers. The imbalance is defined as the difference between the energy measured by the two photomultipliers.

For the determination of the  $y$ -position, a slightly different approach was used [57]:

$$y = y_{max} + p_1 \left( p_2 \left( \frac{w_{y_1} - w_{y_2}}{\sum_{i=1}^3 w_{y_i}} \right) \right),$$

where  $y_{max}$  is the position of the cell with  $E_{max}$  and the  $p_i$  denote polynomials of fourth order. Here the weights:

$$w_{y_i} = \max \left( 0, \log \frac{E_{y_i}}{\sum_{i=1}^3 E_{y_i}} + 5 \right)$$

were used.

### 4.1.2 RHES

#### Signal Reconstruction

The signals from the RHES pads are processed by amplifiers and a pulse former, the latter improving the signal-to-noise ratio [48]. A typical output signal from the pulse formers is shown in Figure 4.1 as a function of time. For storage, the signal is sampled in three time intervals of a distance of 96 ns such that the second sample is approximately taken at the maximum of the signal. The rise time of the pulse former of 180 ns is chosen such that it is slightly smaller than the time of two scan intervals. The three signals  $s_1$ ,  $s_2$  and  $s_3$  are then digitized and given to the trigger and eventbuilder, so that they can be used for signal reconstruction.

If the form of the pulse is known as function  $p(t)$ , any  $s_i$  can give the amplitude  $A$ :

$$s_i = A \cdot p((i-1)\Delta T),$$

where  $\Delta T = 96$  ns is the time interval between the  $s_i$ . Using more than one value is more precise as the effects of electronic noise can be suppressed. Thus all three scan values are used in a weighted sum to reconstruct the amplitude [58]:

$$A = \frac{\sum_{i=1}^3 s_i p((i-1)\Delta T)}{\sum_{i=1}^3 p^2((i-1)\Delta T)}$$

The amplitude of a signal is proportional to the energy deposited in the pad. The calibration of the amplitude, which is given in ADC counts, is done as follows [48]: the preamplifiers which are following each RHES pad are fed back by a calibrated capacity such that a certain amount of charge released by a particle in the diode produces a well known output voltage of the preamplifiers. The conversion of this output voltage to ADC counts, i.e. the calibration of the remaining electronics, is the done by measuring the signal from test pulses. As the charge released by a minimum ionizing particle is well known the energy can be given in units m.i.p., the energy deposited by a minimum ionizing particle. The calibration was checked by measuring the signals from halo muons which are expected to deposit an energy of 1 m.i.p.. The result showed a reasonable agreement with the above procedure though in some towers an over-calibration is visible [59].

The mean energy deposit for a shower induced by photons as a function of the photon energy as measured by RCAL has been measured with the sample of photons from the decay  $\omega \rightarrow$

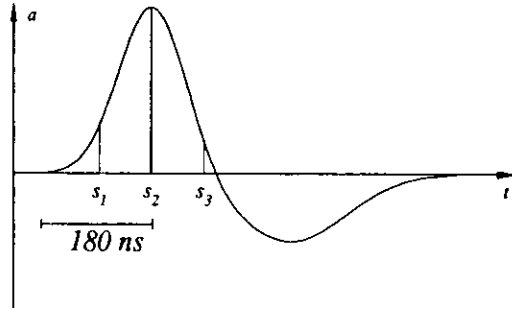


**Figure 4.1:** Typical output signal  $a$  from the RHES amplifiers as a function of time  $t$  [48]. The signal has a rise time of 180 ns. The RHES signal is reconstructed by the three scan values  $s_1$ ,  $s_2$  and  $s_3$ , which are taken in time intervals of 96 ns.

$\pi^+\pi^-\pi^0(\pi^0 \rightarrow \gamma\gamma)$  (see Section 5.1 for the selection criteria) and is shown in Figure 4.2. A fit with a straight line yields a slope of  $7.6 \pm 1.0$  m.i.p./GeV. The offset at the origin is due to the fact that only those photons were selected which indeed produced a signal in RHES; in this case the photon started already to shower and thus deposits at least 2 m.i.p. in RHES, which is in good agreement with the offset given by the fit:  $2.0 \pm 0.5$  m.i.p. For comparison, an electron is expected to deposit 8.5 m.i.p. per 1 GeV [48].

### Clustering

The creation of clusters in RHES is similar to that of RCAL. The RHES is close to the maximum of an electromagnetic shower, so that the limited transverse extension of a shower can be taken into account. The Molière radius is approximately 2 cm. Hadronic showers typically start behind the RHES<sup>2</sup>, yielding a small transverse extension, too. Thus RHES clusters can be limited in size; a size of  $3 \times 3$  RHES pads is chosen. The clustering is performed in the following steps:

1. RHES pads with an energy greater than 1 m.i.p. are placed in a list sorted by their energy. Pads which were recognized as noisy or dead in a data quality analysis are excluded from this list
2. The pad with the highest energy serves as a seed for the first cluster and is removed from the list.

<sup>2</sup>The probability of a hadronic shower to start in the part of RCAL in front of RHES is approximately 9%.

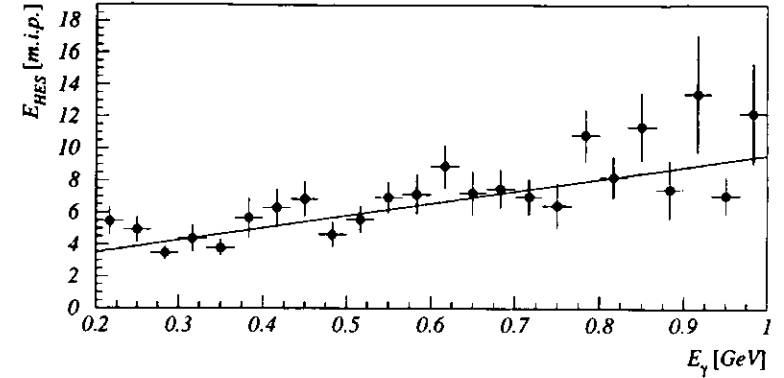


**Figure 4.2:** Energy  $E_{HES}$  deposited in RHES versus the energy  $E_\gamma$  measured by RCAL for photons. The curve is a fit with a straight line.

3. All pads in a  $3 \times 3$  area around the seed are included into this cluster and removed from the list.
4. The 2nd and 3rd steps are repeated, beginning now with the most energetic pad in the list after having removed those pads already used in a cluster. This is repeated until all pads in the list are assigned to any cluster.

The sum of the energy of the pads in a cluster is considered as the energy of the cluster itself.

### Position Reconstruction

To reconstruct the position of a particle hitting RCAL, the RHES allows to increase the precision due to its small dimensions. If only a single pad is hit, a position resolution of  $3\text{ cm}/\sqrt{12} \approx 0.9\text{ cm}$  will be achieved. In case of several pads being hit, the above clusters are formed and the position is reconstructed as explained in the following.

As already mentioned, the lateral extension of an electromagnetic shower is small. Therefore most of the information is already considered if one takes into account only the central pad together with its neighbours in  $x$  or  $y$  direction with the highest energy, respectively. The ratio:

$$R = \frac{E_{\text{central}}}{E_{\text{central}} + E_{\text{neighbour}}}$$

was measured with electrons in ZEUS [60]. Here  $E_{\text{central}}$  is the energy of the pad in the centre of the cluster (i.e. the pad with the highest energy) and  $E_{\text{neighbour}}$  is the energy of the most

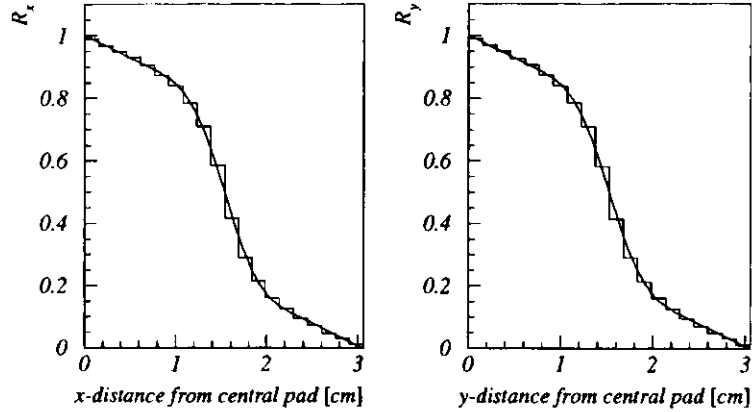


**Figure 4.3:** The energy ratio  $R$  of the central to its most energetic neighbouring diode versus the position for RHES clusters in  $x$  and  $y$  direction [60].

energetic neighbour pad in  $x$  or  $y$  direction. Assuming a position dependence of  $R$  proportional to  $\tanh x$  (or  $\tanh y$ ) and an equal distribution of the electrons over the distance of two pads, the ratio could be unfolded, yielding a relation between  $R$  and the distance of the hit to the central diode, as shown in Figure 4.3. These distributions were fitted with a tanh function in the central part and a linear function at the edges. This yielded for  $R$  in  $x$  and  $y$  direction [60]:

$$R_x = \begin{cases} -0.39 \cdot \tanh(2.49 \text{ cm}^{-1} \cdot x) + 0.50 & |x| < 0.69 \text{ cm} \\ -0.15 \text{ cm}^{-1} \cdot x + 0.77 & |x| > 0.69 \text{ cm} \end{cases} \quad (4.1)$$

and

$$R_y = \begin{cases} -0.43 \cdot \tanh(1.34 \text{ cm}^{-1} \cdot y) + 0.50 & |y| < 0.69 \text{ cm} \\ -0.16 \text{ cm}^{-1} \cdot y + 0.75 & |y| > 0.69 \text{ cm} \end{cases} \quad (4.2)$$

Inversion of the functions (4.1) and (4.2) together with the position of the central diode thus gives the position of the whole cluster. It was shown that the position resolution of 5 mm can be achieved for electrons above an energy of 5 GeV [60]. The algorithm was checked using electrons from the conversion of photons in the beampipe identified by the CONVERT2 finder [68] with an energy of the order of 1 GeV. The agreement with the extrapolated position information from the tracking chambers was good.

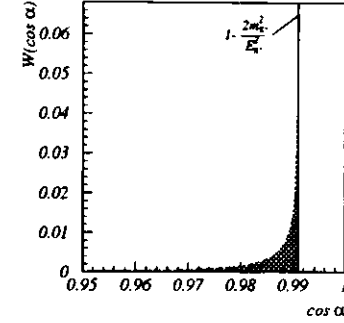


**Figure 4.4:** The probability distribution  $W$  of the cosine of the opening angle  $\alpha$  between the two photons in the decay  $\pi^0 \rightarrow \gamma\gamma$  for a  $\pi^0$  with energy  $E_{\pi^0} = 2 \text{ GeV}$ .

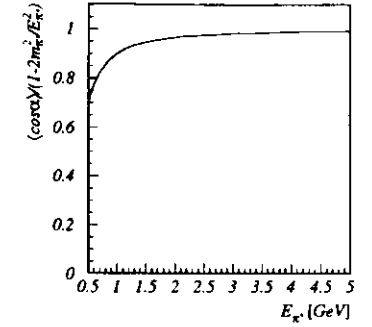


**Figure 4.5:** Average cosine of the opening angle ( $\cos \alpha$ ) in the  $\pi^0 \rightarrow \gamma\gamma$  decay divided by the maximum given by equation (4.3) as a function of  $E_{\pi^0}$ .

#### 4.1.3 Combining RCAL and RHES

To combine the RCAL condensates with the RHES clusters, the  $x$  and  $y$  position of the RCAL condensates is extrapolated to the RHES plane ( $z = -152 \text{ cm}$ ). All RHES clusters within a distance of 15 cm from the position of an RCAL condensate are assigned to the latter. RCAL condensates without any assigned RHES cluster and RHES clusters which were not assigned to any RCAL condensate are considered as noisy and discarded for the  $\pi^0$  analysis. RCAL condensates with  $n$  RHES clusters are considered as created by  $n$  particles which could not be separated by RCAL but by RHES.

## 4.2 Reconstruction of the $\pi^0$

Using the energy information of the RCAL condensates and the position information of the RHES clusters (which is more precise than that from the RCAL condensates), the invariant mass of this system can be calculated assuming that the RCAL-RHES signals are induced by showers from photons. The  $\pi^0$  meson was identified on the basis of this invariant mass.

One of the difficulties despite a clear identification of a photon signal is the separation of the two photons. The opening angle between the two photons  $\alpha$  has a lower limit, which is given by:

$$\cos \alpha \leq 1 - \frac{2m_{\pi^0}^2}{E_{\pi^0}^2}, \quad (4.3)$$

where  $E_{\pi^0}$  is the energy of the  $\pi^0$  meson. The probability distribution of the cosine of the opening



angle,  $W(\cos \alpha)$  as shown in Figure 4.4 demonstrates that in most of the decays the opening angle  $\alpha$  is quite close to its limit. In fact, as shown in Figure 4.5, the mean value of  $\cos \alpha$  is close to the upper limit given by equation (4.3) for most of the  $\pi^0$  energies. Thus the opening angle between the photons behaves approximately as given by the right hand side of equation (4.3), i.e. decreases with increasing energy, making a separation of the signals from the two photons in case of high energy more difficult or even impossible. Thus three cases are distinguished in the following:

- The showers induced by the two photons from the  $\pi^0$  decay can be separated in RCAL. Due to the coarse structure of RCAL the opening angle is restricted to relatively large values, which corresponds to small  $\pi^0$  energies. This case is discussed in Section 4.2.1.
- The showers induced by the two photons from the  $\pi^0$  decay can be separated only in the RHES. The mechanical dimensions of the RHES pads are smaller than those of the RCAL cells. Thus higher  $\pi^0$  energies are accessible with this method. This case is discussed in Section 4.2.2.
- The showers induced by the two photons from the  $\pi^0$  decay can be separated neither by RCAL nor by RHES. This corresponds to larger  $\pi^0$  energies. Due to the missing separate position information, a reconstruction of the invariant mass of the two photons and an identification of the  $\pi^0$  is impossible. This case is therefore not investigated.

#### 4.2.1 Low-Energy $\pi^0$ Mesons

In the case of  $\pi^0$  mesons with relatively small energies, the opening angle  $\alpha$  is expected to be large enough so that the decay photons can be separated in RCAL. The size of an RCAL cell is  $20 \times 10 \text{ cm}^2$ , so that the minimum distance between two condensates is  $\sqrt{20^2 + 10^2} \text{ cm} \approx 22.4 \text{ cm}$ . Assuming equality in equation (4.3), the corresponding opening angle<sup>3</sup> is equivalent to  $E_{\pi^0} \approx 2 \text{ GeV}$ . Thus for  $E_{\pi^0} < 2 \text{ GeV}$  one expects to find two RCAL condensates each with one assigned RHES cluster, where each RCAL-RHES cluster belongs to one of the decay photons.

Using now the position information from the RHES clusters and the vertex position from charged tracks one can determine  $\alpha$ . Together with the energy of the RCAL condensates  $E_{CAL_1}$  and  $E_{CAL_2}$ , the invariant mass of the two photons is given by:

$$m_{\gamma\gamma} = \sqrt{2 \cdot E_{CAL_1} E_{CAL_2} (1 - \cos \alpha)}. \quad (4.4)$$

The shape of the reconstructed  $m_{\gamma\gamma}$  for a  $\pi^0$  meson at 1 GeV is shown in Figure 4.6(a) assuming an energy resolution of the RCAL-EMC of  $0.18\sqrt{E} \cdot 1 \text{ GeV}$ , where  $E$  is the cluster energy (see Section 3.2.1), and a position resolution of the RHES of 0.9 cm (see Section 4.1.2). For comparison, Figure 4.6(b) shows the contribution from the position resolution (i.e. assuming an infinitely precise energy measurement), which is obviously negligible against the contribution from the energy resolution. Thus the width of the peak is expected to be a function of energy only. Figure 4.6(c) shows the Gaussian width  $\sigma$  of the  $m_{\gamma\gamma}$  peak as a function of the  $\pi^0$  energy  $E_{\pi^0}$ .

<sup>3</sup>Assuming a direction of flight of the  $\pi^0$  perpendicular to the RCAL surface.

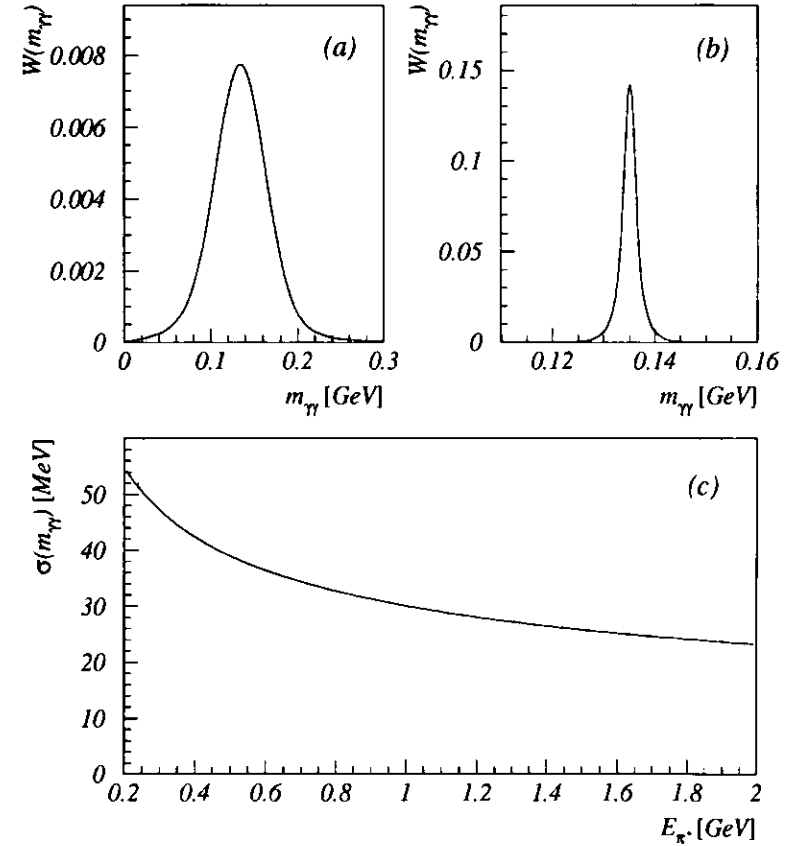


**Figure 4.6:** (a): Expected shape of  $m_{\gamma\gamma}$  reconstructed from the decay of a  $\pi^0$  meson with an energy of 1 GeV using equation (4.4) and assuming an energy and position resolution as given in the text. (b): Contribution from the position resolution to the shape of  $m_{\gamma\gamma}$  with an enlarged vertical scale. (c): Energy behaviour of the width  $\sigma$  of the  $m_{\gamma\gamma}$  peak.

### 4.2.2 High-Energy $\pi^0$ Mesons

For larger  $\pi^0$  energies, i.e. for  $E_{\pi^0} > 2 \text{ GeV}$ , it is expected that the showers of the photons merge into one RCAL cluster, but due to the smaller dimensions they can still be separated by RHES. The minimum necessary distance of two RHES pads to be separated by the clustering algorithm is 6cm. The corresponding opening angle<sup>3</sup> is equivalent to  $E_{\pi^0} \approx 7 \text{ GeV}$  assuming equality in equation (4.3). Thus one can find  $\pi^0$  mesons in the range  $2 < E_{\pi^0} < 7 \text{ GeV}$  by looking for RCAL condensates with two assigned RHES clusters.

The RHES position information allows again to determine  $\alpha$ . In contradiction to the above case, only the sum of the energy of the photons, i.e. the  $\pi^0$  energy, is available as only one RCAL condensate containing the showers of both photons could be created and the energy information of RHES is not reliable enough. Thus an assumption has to be made about the distribution of  $E_{\pi^0}$  between the photons. As the energy of each photon is uniformly distributed between zero and the  $\pi^0$  energy, no distinguished value is available. Assuming  $E_\gamma = \frac{1}{2} E_{\pi^0}$ , equation (4.4) becomes:

$$m_{\gamma\gamma} = E_{CAL} \cdot \sqrt{\frac{1}{2}(1 - \cos\alpha)}, \quad (4.5)$$

where  $E_{CAL}$  denotes the energy of the RCAL condensate (i.e. corresponds to  $E_{\pi^0}$ ).

To visualize the effect of this simplification, the decay of  $\pi^0$  mesons with an energy of 3 GeV was simulated. The energy of the decay photons was smeared by a Gaussian according to the RCAL-EMC energy resolution (see above). For simplicity, the contribution of the position resolution was neglected as it is small (see above). The reconstructed mass  $m_{\gamma\gamma}$  is shown in Figure 4.7. The solid line shows the result from equation (4.4), while the dashed line shows the approximation by equation (4.5). The peak in the mass distribution derived by the latter ansatz is obviously shifted to higher masses and an extended tail at high masses is visible. The relative shift of the peak mass value with respect to  $m_{\pi^0}$  as a function of the  $\pi^0$  energy is shown in Figure 4.8.

### 4.2.3 Application to Data

The two methods for the reconstruction of a  $\pi^0$  meson were applied to a sample of events being candidates of  $ep$  scattering with  $Q^2 \gg 0^4$ . To remove background, only those RCAL-RHES clusters were subject to the reconstruction which were at least 20cm away from the entry point of any track pointing onto the RCAL or RHES surface. The resulting spectrum of the invariant two-photon mass  $m_{\gamma\gamma}$  as reconstructed by the method described in Section 4.2.1 is shown in Figure 4.9(top). A peak in the region of the  $\pi^0$  mass is visible as well as a huge amount of background, mainly due to combinatorial effects and due to particles misidentified as photons. The peak value of  $m_{\gamma\gamma}$  is shifted to a value below  $m_{\pi^0}$ . This is caused by inactive material between the RCAL and the interaction point making the measured energy of the photons systematically smaller. The effect is discussed below.

The bottom plot of Figure 4.9 shows  $m_{\gamma\gamma}$  as reconstructed by the method described in Section 4.2.2 after requiring an RHES energy of at least 3 m.i.p. for each cluster to reject hadronic background. As the energy of the photons tagged by this method is quite high, the loss in effi-

<sup>4</sup>The data were selected by the "DIS neutral current bit". The selection criteria were essentially a requirement of an electron candidate and some general kinematic cuts on variables like  $E - p_z$ .

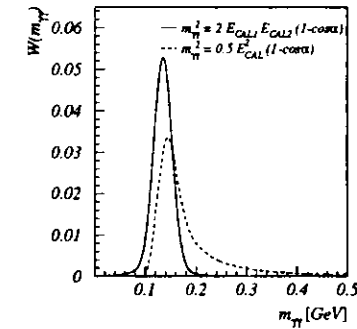


**Figure 4.7:** Invariant mass  $m_{\gamma\gamma}$  of the photons from a  $\pi^0$  decay, reconstructed via equation (4.4) (solid line) or via equation (4.5) (dashed line) for  $\pi^0$  mesons of 3 GeV.

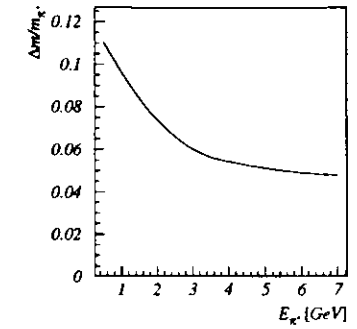


**Figure 4.8:** Relative shift in the peak mass value with respect to  $m_{\pi^0}$  as a function of the  $\pi^0$  energy  $E_{\pi^0}$  for the  $\pi^0$  reconstruction according to equation (4.5).

ciency due to this cut is small. Different to the low-energy method, the amount of combinatorial background is small as only few wrong combinations are possible due to the small considered geometrical area.

### 4.2.4 Correction of the Energy of the Photons

As shown above, the value of the peak in the  $m_{\gamma\gamma}$  spectrum is shifted with respect to the  $\pi^0$  mass. This is expected if the photons from the decay loose energy in material between the interaction point and the RCAL which makes the energy measured by RCAL systematically too small. Components like the CTD contribute to this inactive material. The amount of inactive material in front of RCAL in units of a radiation length and as a function of the polar angle  $\theta$  in ZEUS coordinates is shown in Figure 4.10. It was derived from the ZEUS detector simulation. To compensate for the energy loss in the inactive material, a correction must be applied. Two possible ways are discussed in the following.

#### Correction with Monte Carlo Information

As the true energy of photons is available in Monte Carlo simulations, they allow to determine the energy loss in the inactive material as a function of the measured energy and the amount of inactive material. The ratio of measured to true energy of a photon detected in RCAL was determined using a Monte Carlo of elastic  $\omega$  photoproduction (see Chapter 5). For visualisation, the result for an RCAL region preceded by approximately one radiation length of inactive material is shown in Figure 4.11. Obviously, the loss for high energies is small while it increases to more

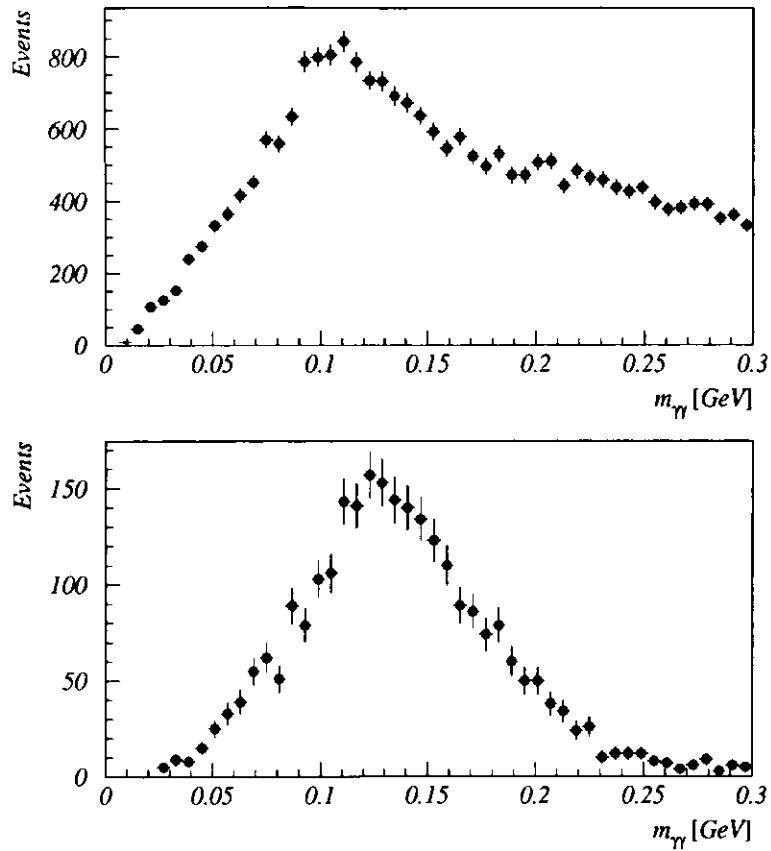


**Figure 4.9:** Spectrum of the invariant two-photon mass  $m_{\gamma\gamma}$  as reconstructed by the method described in Section 4.2.1 (top) and Section 4.2.2 (bottom). The latter is shown after requiring an RHES energy of at least 3 m i.p. for each cluster while the former is shown after requiring an RCAL energy of at least 200 MeV for each cluster.

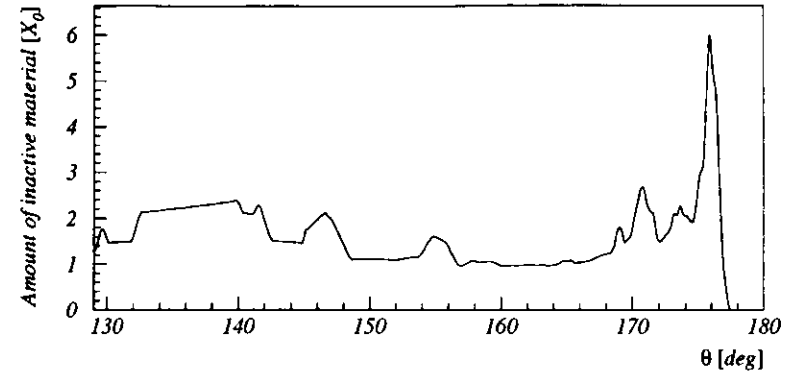


**Figure 4.10:** Inactive material in front of RCAL measured in radiation lengths as a function of the polar angle  $\theta$ .

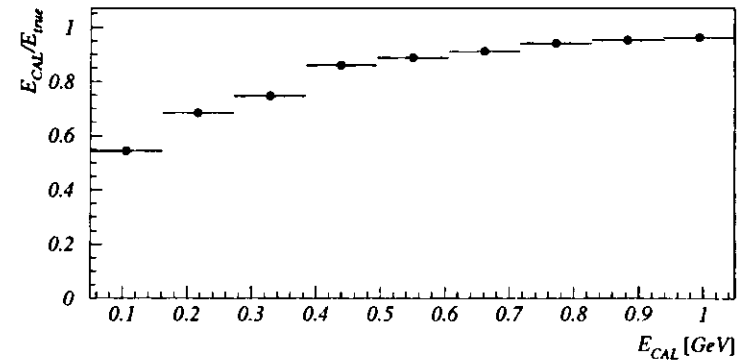


**Figure 4.11:** Fraction of energy measured by RCAL with respect to the incident particle energy as function of the measured photon energy  $E_{CAL}$ . The values were derived from Monte Carlo selecting a region of RCAL preceded by approximately one radiation length of inactive material.

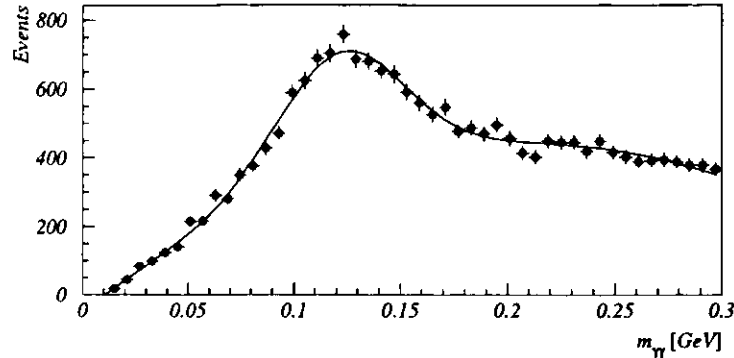


**Figure 4.12:** Spectrum of the invariant two-photon mass  $m_{\gamma\gamma}$  as reconstructed by the method described in Section 4.2.1 with an energy correction according to equation (4.6). The line is the result of a fit with a Gaussian plus a second order polynomial.

than 50% for energies below 100 MeV. These results were parametrized as a function of the measured energy  $E_{CAL}$  in GeV and the amount of inactive material  $X$  in radiation lengths, yielding:

$$\frac{E_{CAL}}{E_{true}} = \min\left((0.39 + 1.59E_{CAL} - 1.56E_{CAL}^2 + 0.54E_{CAL}^3)(1.083 - 0.083X), 1\right), \quad (4.6)$$

where  $E_{true}$  is the generated energy of the photon in the Monte Carlo. The data shown in Figure 4.9(top) were corrected according to equation (4.6) yielding the spectrum shown in Figure 4.12. A fit with a combined Gaussian and a second order polynomial yielded a Gaussian mean of  $123 \pm 1$  MeV. The difference of the mean to the  $\pi^0$  mass is a consequence of an underestimate of the inactive material in Monte Carlo and therewith an insufficient correction of the data.

#### Correction with the Presampler

The above described correction method has two disadvantages:

- the correction is only an average over all measured photons and thus does not take into account the fluctuations in the showers in the inactive material;
- the correction depends on the amount of dead material as given by the detector simulation, which does not necessarily reproduce the reality.

Thus a presampler consisting of scintillator tiles was installed in front of RCAL and FCAL (see Section 3.2.1). The enhanced particle multiplicity which appears if a particle showers already in

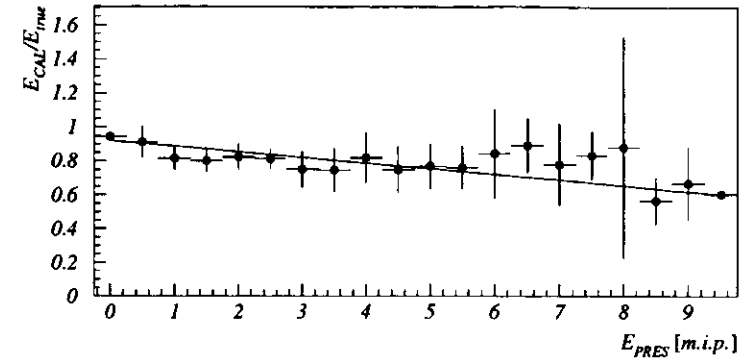


**Figure 4.13:** Fraction of energy measured by RCAL with respect to the incident particle energy as function of the energy measured in the presampler  $E_{PRES}$ . The values were derived from Monte Carlo. The curve is the result from a linear fit.

material in front of the RCAL is measured by this presampler and can be used for a correction of the energy. This allows an individual correction for each particle and depends only partially on the detector simulation.

The above mentioned Monte Carlo simulations were again used to determine the fraction of energy measured by RCAL as a function of the particle multiplicity given by the presampler (in units m.i.p.) for photons. The result is shown in Figure 4.13. The points were fitted with:

$$\frac{E_{CAL}}{E_{true}} = P_0 + P_1 E_{PRES}, \quad (4.7)$$

where  $E_{CAL}$  is the energy measured by RCAL,  $E_{PRES}$  the energy (or particle multiplicity) measured by the presampler and  $E_{true}$  the incident photon energy given by the Monte Carlo. The fit yielded:

$$\begin{aligned} P_0 &= 0.92 \pm 0.01, \\ P_1 &= -0.033 \pm 0.001 \text{ m.i.p.}^{-1}. \end{aligned}$$

The data shown in Figure 4.9(top) were corrected according to equation (4.7) yielding the spectrum shown in Figure 4.14. A fit with a combined Gaussian and a second order polynomial yielded a Gaussian mean of  $133 \pm 1$  MeV which is in good agreement with  $m_{\pi^0}$ .

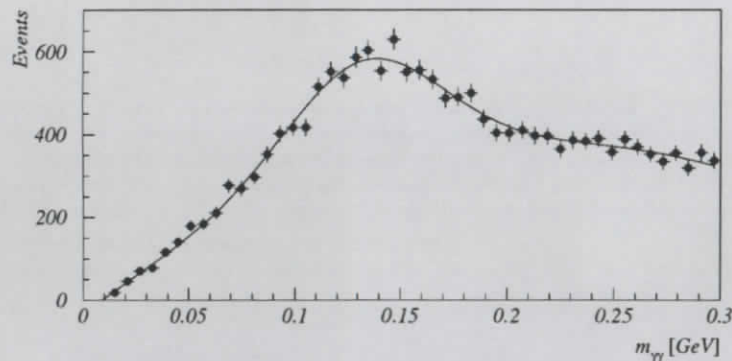


**Figure 4.14:** Spectrum of the invariant two-photon mass  $m_{\gamma\gamma}$  as reconstructed by the method described in Section 4.2.1 with an energy correction according to equation (4.7). The line is the result of a fit with a Gaussian plus a second order polynomial.

## Chapter 5

# Elastic Photoproduction of $\omega$ Mesons

This chapter deals with the measurement of the photoproduction of  $\omega$  mesons using the reaction  $ep \rightarrow e\omega p$  with the ZEUS detector at HERA. Parts of the material were released previously [61, 62].

The  $\omega$  meson was observed via its decay into  $\pi^+\pi^-\pi^0$  ( $\pi^0 \rightarrow \gamma\gamma$ ) in the kinematic range  $70 < W_{\gamma p} < 90$  GeV and  $p_T^2 < 0.6$  GeV<sup>2</sup>. For these events the scattered positron was not observed in the detector, thereby restricting  $Q^2$  to values smaller than 4 GeV<sup>2</sup>. The kinematically given lower limit (2.1) is  $Q_{min}^2 = 10^{-9}$  GeV<sup>2</sup>. The median  $Q^2$  is about  $10^{-4}$  GeV<sup>2</sup>.

### 5.1 Event Selection and Reconstruction

The data presented in this chapter were taken in 1994 and correspond to a total integrated luminosity of 3.2 pb<sup>-1</sup>. Due to technical reasons only the positron runs are used, corresponding to an integrated luminosity of 2.6 pb<sup>-1</sup>. The criteria to select events from the reaction  $ep \rightarrow e\omega p$  on trigger level and on offline level are discussed below as well as the methods used to reconstruct the  $\omega$  via its decay into  $\pi^+\pi^-\pi^0$  ( $\pi^0 \rightarrow \gamma\gamma$ ).

#### 5.1.1 Trigger

There are two possible bits in the sample of the soft photoproduction events to select  $\omega$  candidates: The  $\omega$  bit and the  $\rho$  bit, the latter differing from the  $\omega$  bit only by a tighter cut on the mass of any pair of tracks and on the total number of tracks at the TL. The selection criteria of both trigger bits applied in the three levels of the trigger are (different values of the  $\omega$  bit at the TL are given in parentheses):

- FLT:
  - at least 464 MeV deposited in the electromagnetic section of the RCAL,
  - less than 1250 MeV deposited in the FCAL towers surrounding the beam pipe,
  - at least one good track candidate found in the CTD,

- reject events with hits in the C5 or the veto wall, if timing consistent with that of a  $p$ -gas collision occurring upstream of the interaction point.
- SLT:
  - total energy in FCAL less than 5 GeV,
  - total energy in BCAL less than 5 GeV,
  - reject events with calorimeter timing indicating that the event has occurred upstream of the interaction point.
- TLT:
  - number of vertices equal to one and number of reconstructed tracks less than or equal to four (five),
  - the absolute  $Z$  value of the reconstructed vertex must be within 66 cm,
  - the invariant mass of any pair of the tracks must be less than 1.5 GeV (2.5 GeV), assuming pions masses,
  - tighter cuts on the calorimeter timing.

The rate of events passing this trigger was about 1 Hz. To reduce the rate, only every 2nd to 6th (run-dependent) event was saved and written to tape.

Due to this prescale applied at both bits, the effective integrated luminosity  $\mathcal{L}$  can be increased by using both bits. The relative difference in efficiency between both is less than 1% in the final  $\omega$  selection after all offline cuts (which are described below). Therefore the two bits can safely be assumed to be equal and thus can be used together, which is done in the following. The effective prescale  $P_{tot}$  of the combination of the two bits is given by:

$$P_{tot} = (P_1^{-1} + P_2^{-1} - P_1^{-1} \cdot P_2^{-1})^{-1},$$

where  $P_1$  and  $P_2$  are the prescale factors of the  $\omega$  and  $\rho$  bits, respectively. The effective prescale averaged over all runs is  $\langle P_{tot} \rangle \approx 2.9$ . The data sample corresponds by this to an effective integrated luminosity of  $\mathcal{L} = 894 \pm 13 \text{ nb}^{-1}$ .

### 5.1.2 Selection Criteria

The final sample of  $\omega$  events was selected by imposing the following offline requirements:

- Two tracks with opposite charges associated to a common vertex and no further tracks.
- A well reconstructed  $\pi^0$  candidate from two clusters (as defined in Section 5.1.3) in RCAL and RHES, with at most one additional cluster, as described in detail below.
- No clusters in BCAL or RCAL with energy greater than 200 MeV and more than 20 cm away from the extrapolated position of either of the two tracks. The cut was not applied to the clusters in the RCAL associated to the  $\pi^0$  candidate. This cut rejects events with additional neutral particles.

- Transverse momentum of each track greater than 100 MeV and pseudorapidity<sup>1</sup>  $\eta \geq -2.0$ , to restrict the data to a region of good track reconstruction efficiency.
- Total energy in FCAL less than 1 GeV, in order to limit the contamination by proton dissociative events ( $\gamma p \rightarrow \omega N$ ).

In total, 1103 events were selected.

### 5.1.3 Reconstruction of the $\pi^0$

For the reconstruction of the  $\pi^0$  via the decay photon pair, signals in RCAL and RHES were used as described in Chapter 4

RCAL clusters are objects consisting of adjacent calorimeter cells (see Section 4.1.1). For the present data, clusters were usually formed by one cell. To reject background from uranium radioactivity, a minimum cell energy of 100 MeV was required. This should be compared with the mean measured photon energy of 500 MeV with a standard deviation of 210 MeV, which is reproduced by the simulations described below.

RHES clusters consist of at most  $3 \times 3$  adjacent silicon pads (see Section 4.1.2). Most (63%) of the clusters consisted of a single pad. A cut on the signal from any RHES pad with less than 1 m.i.p. was applied to reject noise. The mean RHES signal for this data sample was 4.2 m.i.p. with a standard deviation of 2.5 m.i.p.

RHES clusters were assigned to RCAL clusters as described in Section 4.1.3. RCAL clusters less than 20 cm away from the extrapolated impact point of a charged track were excluded, thus restricting the sample to clusters produced by neutral particles. Events with exactly two of these neutral RCAL-RHES clusters were then selected, allowing at most one additional cluster in RCAL with no corresponding RHES cluster and an energy of less than 200 MeV. These two RCAL-RHES clusters were required to have an energy deposition in the electromagnetic part of the calorimeter only.

All reconstructed  $\pi^0$  mesons had a small energy, so that essentially all were reconstructed by the method of Section 4.2.1. In fewer than 0.5% of the events RCAL clusters were associated with more than one RHES cluster, i.e. corresponding to the reconstruction method described in Section 4.2.2. Even less frequent were events in which the two decay photons were assigned to one RHES cluster.

The energy correction for losses in the material between the interaction point and the RCAL based on Monte Carlo information as described in Chapter 4.2.4 was used. With the corrected RCAL energies and the RHES position information the two-cluster invariant mass  $m_{\gamma\gamma}$  was calculated using equation (4.4). The spectrum for data and the below described Monte Carlo simulation is plotted in Figure 5.1. A fit with the sum of a Gaussian and a second order polynomial yields a mean of the Gaussian of  $\langle m_{\gamma\gamma} \rangle = 124 \pm 1 \text{ MeV}$  and a standard deviation of  $28 \pm 1 \text{ MeV}$  for the data and a mean of the Gaussian of  $\langle m_{\gamma\gamma} \rangle = 136 \pm 1 \text{ MeV}$  and a standard deviation of  $27 \pm 1 \text{ MeV}$  for the Monte Carlo. While the standard deviations are in good agreement, the difference in the mean of the data distribution with respect to the  $\pi^0$  mass is a consequence of an insufficient correction due to the incomplete description of low energy electromagnetic showers in the Monte

<sup>1</sup>The pseudorapidity is defined as  $\eta = -\ln(\tan \frac{\theta}{2})$ , where  $\theta$  is the polar angle in the ZEUS coordinate system.

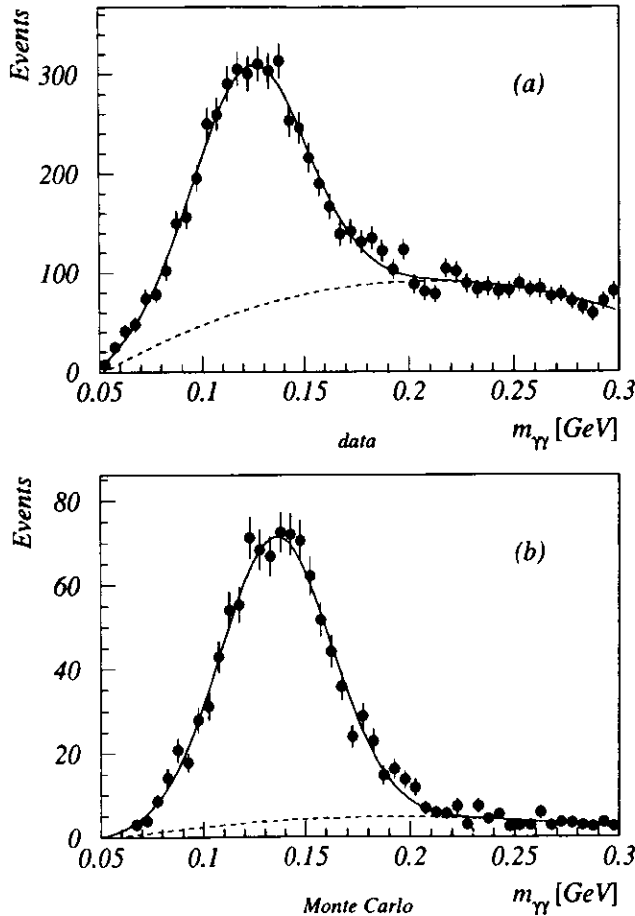


Figure 5.1: Invariant mass distributions of the two photons for (a) data and (b) Monte Carlo. The full line is the result of the fit explained in the text. The dashed line indicates the background as determined by the fit.

Carlo simulation. Events with  $84 < m_{\gamma\gamma} < 164$  MeV, i.e. a mass within  $1.5\sigma$  of  $\langle m_{\gamma\gamma} \rangle$ , were selected.

To improve the resolution in the four-momentum and invariant mass of the  $\pi^+\pi^-\pi^0$  system, the invariant mass of the two photons was constrained to the  $\pi^0$  mass. Since the  $\pi^0$  energies are small, only large opening angles  $\alpha$  between the decay photons occur. As the angle  $\alpha$  is well determined due to the precise position measurement of RHES, the resolution in  $m_{\gamma\gamma}$  is dominated by the energy resolution of RCAL (see Section 4.2.1). Thus only the energies were modified in the procedure. The modified values  $E_{1fit}$ ,  $E_{2fit}$  of the corrected energies  $E_1$ ,  $E_2$  of the RCAL clusters were determined by minimizing the quantity:

$$\chi^2(E_{1fit}, E_{2fit}) = \frac{(E_1 - E_{1fit})^2}{\sigma_{E_1}^2} + \frac{(E_2 - E_{2fit})^2}{\sigma_{E_2}^2}, \quad (5.1)$$

using the constraint:

$$\sqrt{2 \cdot E_{1fit} E_{2fit} \cdot (1 - \cos \alpha)} = m_{\pi^0},$$

where  $\sigma_{E_i}(\text{GeV}) \propto \sqrt{E_i(\text{GeV})}$  are the corresponding energy resolutions of the RCAL.

#### 5.1.4 Reconstruction of the $\omega$

To determine the invariant mass of the  $\pi^+\pi^-\pi^0$  system and the relevant kinematical quantities, the four-momentum  $p_{3\pi}$  of the  $\pi^+\pi^-\pi^0$  system was obtained by adding up the momentum of the two tracks, assuming the pion mass, and the momentum of the  $\pi^0$ .

The invariant mass  $m_{3\pi}$  as obtained from  $p_{3\pi}$  using the energies  $E_1$  and  $E_2$  and applying the cut on  $m_{\gamma\gamma}$  only is shown in Figure 5.2. A peak at the mass of the  $\omega$  meson is already visible. Using the values  $E_{1fit}$  and  $E_{2fit}$  as defined by equation (5.1) to reconstruct the invariant mass  $m_{3\pi}$  one gets a more significant peak at the  $\omega$  mass as shown in Figure 5.3. Thus the fitted energies  $E_{1fit}$  and  $E_{2fit}$  are used for the evaluation of  $p_{3\pi}$  in the following.

The quantities  $W_{pp}$  and  $p_T$  were then derived from  $p_{3\pi}$ . Due to the small  $Q^2$  of the events, equation (2.19) could be used. The analysis was restricted to the range  $70 < W_{pp} < 90$  GeV, where the acceptance is almost flat. Furthermore the region  $p_T^2 < 0.6$  GeV<sup>2</sup> was selected, to limit the background contamination due to proton dissociation.

## 5.2 Acceptance Calculation and Monte Carlo Simulation

### 5.2.1 Determination of the FLT Efficiency

Because of the small energy of the decay products of the  $\omega$ , the cut on the energy measured in the EMC section of the RCAL dominates the FLT efficiency of the searched  $\omega$  events. Due to the uncertain amount of dead material, the insufficiently simulated different calorimeter response to  $\pi^+$  and  $\pi^-$  and an uncertainty in the CAL energy scale at the FLT, it is not clear whether the efficiency of the cut on the RCAL-EMC energy is correctly simulated in the Monte Carlo sample. Therefore an alternative way was used to determine the efficiency of the RCAL-EMC-cut which is partially based on data.

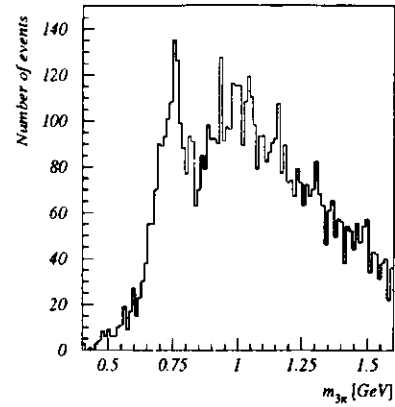


Figure 5.2: Mass of the  $\pi^+\pi^-\pi^0$  system with a cut on  $m_{\gamma\gamma}$ .

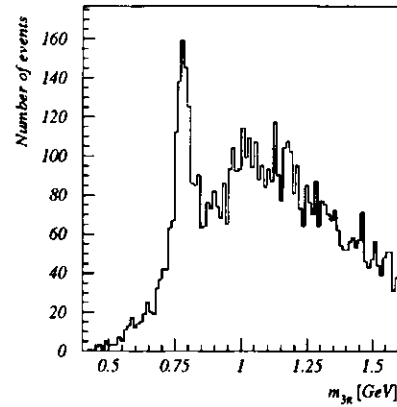


Figure 5.3: Mass of the  $\pi^+\pi^-\pi^0$ -system after correcting the photon energies and constraining  $m_{\gamma\gamma}$  to the  $\pi^0$  mass.

As elastic  $\rho^0$ -photoproduction delivers a huge number of events, the pions from the  $\rho^0$ -decay can be used as a "test beam" as follows [39]: The RCAL is divided into four regions at FLT level as indicated in Figure 5.4. The energy deposited in these four regions of the RCAL as measured at FLT level is stored separately while any pair of RCAL-EMC cells measuring more than 464 MeV at FLT level is able to trigger the corresponding cut. If therefore one selects events where the two decay-pions have hit opposite FLT-regions in the RCAL, an unequivocal assignment of the tracks to the RCAL quarters and thus to the FLT decision of the quarters can be made. After requiring that one of the pions triggered, the decision caused by the other pion is therefore irrelevant to the acceptance of the event and thus statistically independent. The efficiency of the RCAL-EMC cut for  $\pi^+$  ( $\pi^-$ ) mesons is then determined as the ratio of the number of events in which both pions fulfilled the trigger condition to the number of events in which at least the  $\pi^-$  ( $\pi^+$ ) fulfilled the trigger condition. Figure 5.5 shows the results for  $\pi^+$  and  $\pi^-$  separately as a function of the measured momentum  $p$ .

The points were fitted in the restricted range of  $0.4 \leq p \leq 2.5$  GeV with a function of the type:

$$\epsilon(p) = P_1 \cdot (1 - e^{P_2 \cdot (p - P_3)}).$$

As the dependence on azimuthal and polar angle of the ZEUS coordinate system is weak, the average over both angles for the fit parameters are used:

Results for  $\pi^+$ :

$$\begin{aligned} P_1^{\pi^+} &= 0.579 \pm 0.033 \\ P_2^{\pi^+} &= -1.779 \pm 0.396 \text{ GeV}^{-1} \\ P_3^{\pi^+} &= 0.267 \pm 0.088 \text{ GeV} \end{aligned}$$

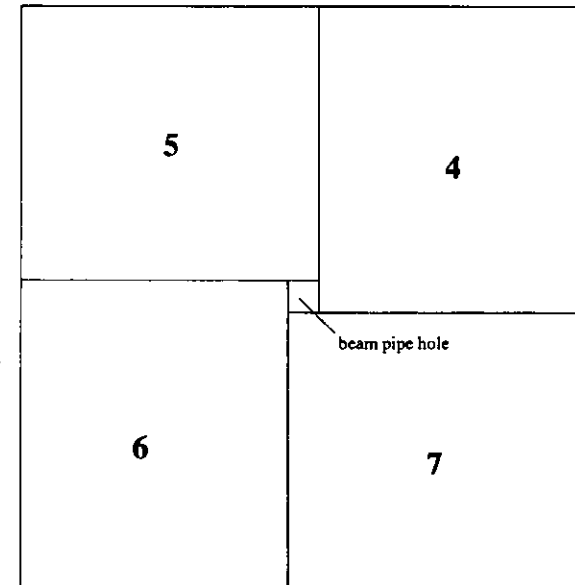


Figure 5.4: Schematic picture of the regions into which the RCAL is divided to store the FLT readout.



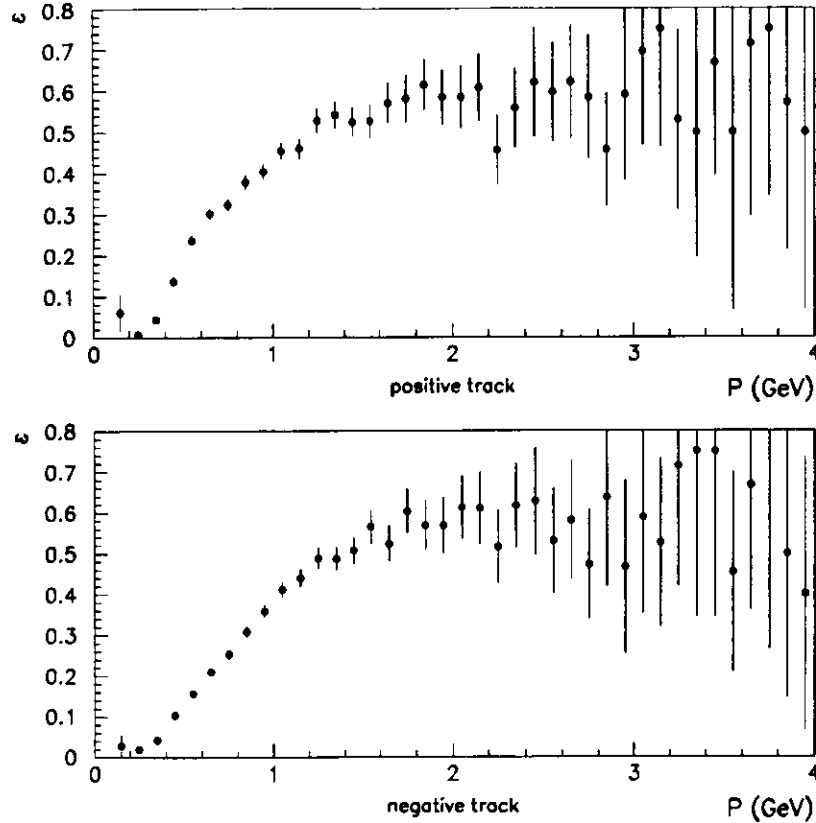


Figure 5.5. FLT-efficiencies of  $\pi^+$  (top) and  $\pi^-$  (bottom) as a function of the measured momentum  $p$  derived from elastic  $\rho^0$  production data [39].

Results for  $\pi^-$ :

$$\begin{aligned} P_1^{\pi^-} &= 0.604 \pm 0.050 \\ P_2^{\pi^-} &= -1.282 \pm 0.311 \text{ GeV}^{-1} \\ P_3^{\pi^-} &= 0.306 \pm 0.051 \text{ GeV} \end{aligned}$$

The maximum efficiency is different from one as there is a certain probability for hadrons to start their shower only in the HAC section of RCAL and thus do not deposit enough energy in the EMC to trigger the event. Looking at this quantitatively, the probability density  $p$  for a hadron to shower at a depth  $x$  in material with a hadronic interaction length  $\lambda$  is [58]:

$$p(x) = \frac{1}{1.22\lambda} e^{-\frac{x}{1.22\lambda}}$$

The probability of a hadron to shower within the RCAL-EMC (which has a depth of  $0.9\lambda$ ) is thus:

$$P_{EMC} = \int_0^{0.9\lambda} p(x) dx = 1 - e^{-\frac{0.9}{1.22}} \approx 0.52.$$

One therefore expects 52% of the  $\pi^\pm$  to start their shower in the EMC and therewith to be able to trigger the RCAL FLT cut. The above results for  $P_1$  are in good agreement with this expectation.

As the  $\omega$  sample could not give sufficient statistics to derive the FLT-efficiency for photons in the same way, this was done using Monte Carlo events from the simulations described below. The algorithm used for this determination is equivalent to the above used for the pions from  $\rho^0$  decay.

The resulting efficiency of a photon pointing to RCAL to trigger the event as a function of the photon energy  $E$  measured in the calorimeter is shown in Figure 5.6. The points were fitted with a function of the type

$$\epsilon(E) = (1 - e^{P_1(E-P_2)}) \cdot (1 - e^{P_3(E-P_4)})$$

with the following result:

$$\begin{aligned} P_1^\gamma &= -23.9 \pm 7.9 \text{ GeV}^{-1} \\ P_2^\gamma &= 0.438 \pm 0.004 \text{ GeV} \\ P_3^\gamma &= -1.8 \pm 2.5 \text{ GeV}^{-1} \\ P_4^\gamma &= -0.3 \pm 1.3 \text{ GeV} \end{aligned}$$

Finally, to apply the correction, the RCAL-EMC-cut was omitted in the Monte Carlo sample while the data were weighted using the above efficiency parametrizations. As the charged pions do not always enter the RCAL, their contribution to the weight was only applied if the corresponding track points into the RCAL. To ensure that no extremely high weight due to a small efficiency occurs, a logical or of cuts on the momentum  $p_{\pi^+}$  and  $p_{\pi^-}$  of the tracks and on the energies  $E_{\gamma_i}$  of the clusters was applied as follows:

$$\begin{aligned} p_{\pi^+} &> 0.3 \text{ GeV}/c \text{ or} \\ p_{\pi^-} &> 0.4 \text{ GeV}/c \text{ or} \\ E_{\gamma_i} &> 0.44 \text{ GeV} \quad (i = 1, 2). \end{aligned}$$

The difference to the usual method (complete simulation of the RCAL cut by Monte Carlo) is 4%.

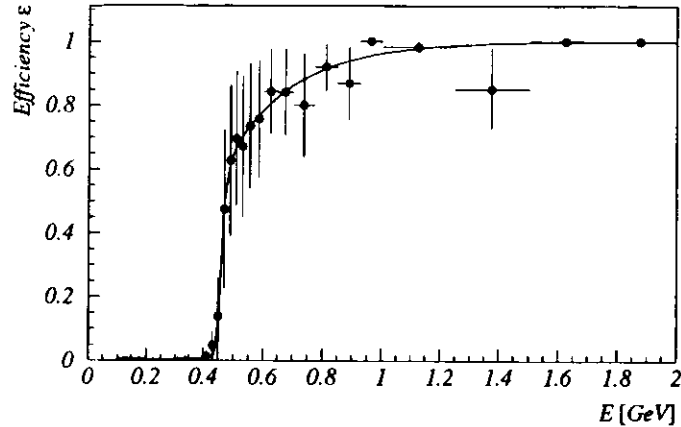


**Figure 5.6:** Efficiency of the RCAL-EMC-cut at the FLT level for photons as a function of the measured energy  $E$  derived from elastic  $\omega$  photoproduction Monte Carlo.

### 5.2.2 Monte Carlo Simulation

The Monte Carlo generators PYTHIA [63] and DIPSI [64] were used to evaluate the acceptance<sup>2</sup>. The former simulates the  $\gamma p$  interaction based on VDM and Regge theory (see Sections 2.2.2 and 2.4.1), while the  $Q^2$  spectrum is generated using the ALLM parametrization [65] of the  $ep$  cross section. The latter uses a model by Ryskin [16], describing vector meson production in terms of a fluctuation of the photon into a  $q\bar{q}$  pair, which interacts with the proton via a Pomeron exchange (see Section 2.4.3). The effective  $W_{\gamma p}$  dependence of the  $\gamma p$  cross section for the events generated was of the type  $\sigma \propto W_{\gamma p}^{0.2}$ . Neither model contains initial or final state radiation. The effect of radiative corrections on the cross section has been estimated to be smaller than 4% [5]. A recent analysis gives an even smaller limit of 2% [66].

The events were generated in the kinematic range  $60 \leq W_{\gamma p} \leq 100$  GeV and  $Q_{min}^2 \leq Q^2 \leq 4$  GeV<sup>2</sup>. In order to adjust the Monte Carlo calculation to the data, the differential cross section  $d\sigma/d|t|$  (see Section 5.6.2) was calculated using the default parameters of PYTHIA and the Monte Carlo events were then re-weighted with the measured slope parameter. The angular distribution of the decay pions was assumed to be that implied by SCHC.

The PYTHIA Monte Carlo sample shows agreement between the reconstructed and generated values of  $W_{\gamma p}$  and  $p_T^2$ . The relative resolution in  $W_{\gamma p}$  is 6% and the resolution in  $p_T^2$  is better than  $0.04$  GeV<sup>2</sup>. They are both dominated by the resolution in the energy measurement of the  $\pi^0$  decay photons.

<sup>2</sup>Except for the RCAL-EMC efficiency, see above.

reduction	efficiency is reduced to	relative reduction	number of events
trigger	30%	30%	$\sim 1.1 \cdot 10^6$
cut on number of tracks	16.5%	55%	$\sim 4.4 \cdot 10^5$
$\pi^0$ reconstruction	1.3 %	8%	6452
remaining cuts	0.89%	68%	1103

**Table 5.1:** Reduction of the efficiency with the different steps in the analysis and the corresponding reduction of the number of events in the data sample.

### Acceptance

The acceptance as a function of four essential quantities,  $W_{\gamma p}$ ,  $p_T^2$  and the helicity angles  $\cos \theta_h$  and  $\phi_h$  for both generators is shown in Figure 5.7. The drop of the acceptance with increasing  $W_{\gamma p}$  or with decreasing  $p_T^2$  is due to one or more of the  $\omega$  decay products escaping detection in the rear region close to the beam pipe. Conversely, with decreasing  $W_{\gamma p}$  the energy of the photons from the  $\pi^0$  decay falls below the value of the cut on the calorimeter energy, thus decreasing the acceptance.

The acceptance evaluated with PYTHIA was used for the cross section determination. The average acceptance in the region  $70 < W_{\gamma p} < 90$  GeV and  $|t| < 0.6$  GeV<sup>2</sup> is 0.89%. It is dominated by the  $\pi^0$  reconstruction; the reduction of the efficiency with the different steps in the analysis is shown in Table 5.1 together with the number of events in the data sample remaining after each step.

A determination of the elastic cross section for  $\gamma p \rightarrow \phi p$  using the decay  $\phi \rightarrow \pi^+ \pi^- \pi^0$  was used as a consistency check (see Section 5.6.1). Also in this case the acceptance was determined using PYTHIA. SCHC was assumed, where the different decay modes of the  $\phi$  meson ( $\phi \rightarrow \rho \pi$  ( $\rho \rightarrow \pi \pi$ ) and  $\phi \rightarrow \pi \pi \pi$  (non-resonant)) were taken into consideration, and the events were weighted according to the measured  $t$  distribution for this reaction [6]. The average acceptance in the region  $70 < W_{\gamma p} < 90$  GeV and  $|t| < 0.6$  GeV<sup>2</sup> is 1.5%.

### Comparison to Data

To check whether the Monte Carlo simulations describe the data well, a comparison of the distributions of  $W_{\gamma p}$ ,  $p_T^2$ ,  $\cos \theta_h$  and  $\phi_h$  was done. The corresponding plots are shown in Figure 5.8 for data (solid circles), PYTHIA Monte Carlo (solid line) and DIPSI Monte Carlo (dashed line). As one can see, the agreement is reasonable.

The acceptance of this analysis is dominated by the  $\pi^0$  reconstruction efficiency. Therefore the RCAL and RHES energy spectra in data and Monte Carlo were compared, yielding a good agreement as shown in Figure 5.9.

### Model Dependence

The model dependence of the Monte Carlo samples was estimated by changing the distributions of  $Q^2$ ,  $W_{\gamma p}$ ,  $t$  and the  $\omega$  decay angles. For the estimate of the dependence on the  $t$ -distribution the slope parameter  $b$  was changed within its statistical uncertainty as given in Section 5.6.2 yielding

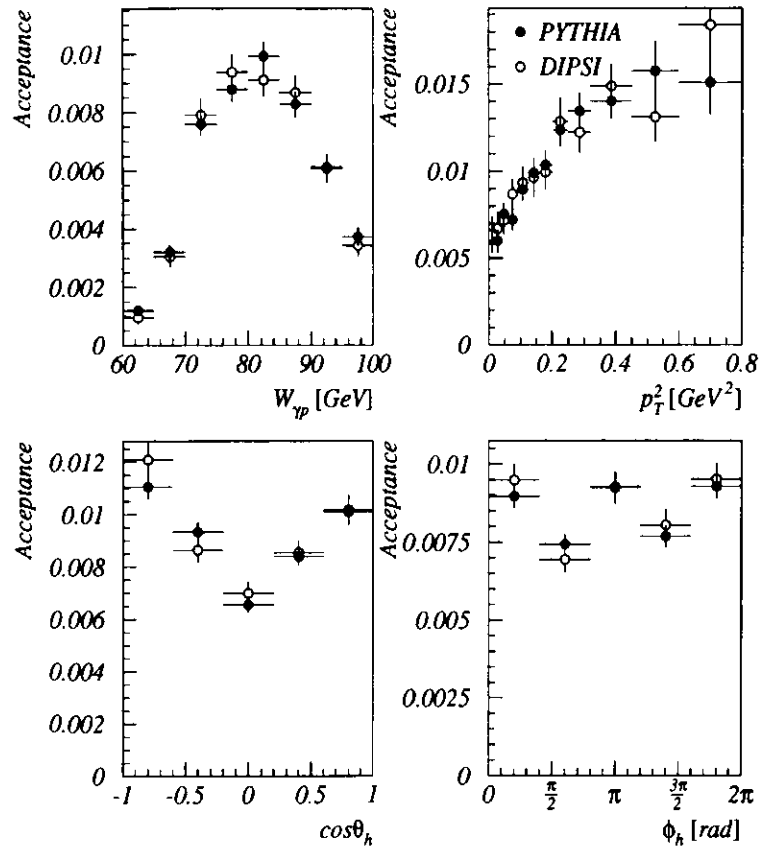


**Figure 5.7:** The acceptance as function of  $W_{yp}$ ,  $p_T^2$ ,  $\cos\theta_h$  and  $\phi_h$  for PYTHIA (solid circles) and DIPSI (open circles).

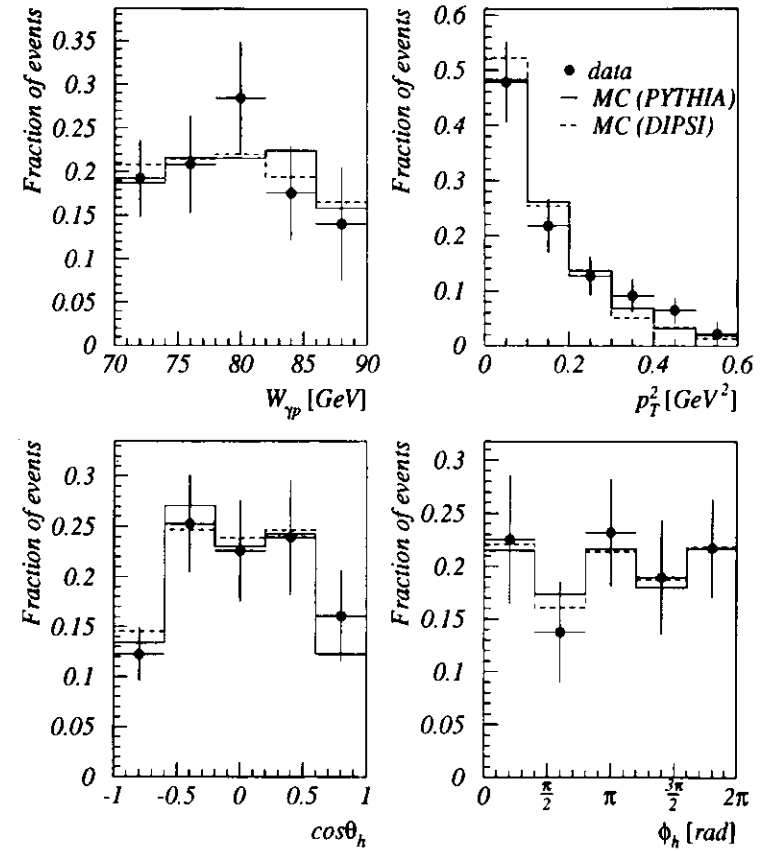


**Figure 5.8:** Comparison of the measured  $W_{yp}$ ,  $p_T^2$ ,  $\cos\theta_h$  and  $\phi_h$  distributions between data and the two Monte Carlo generators.

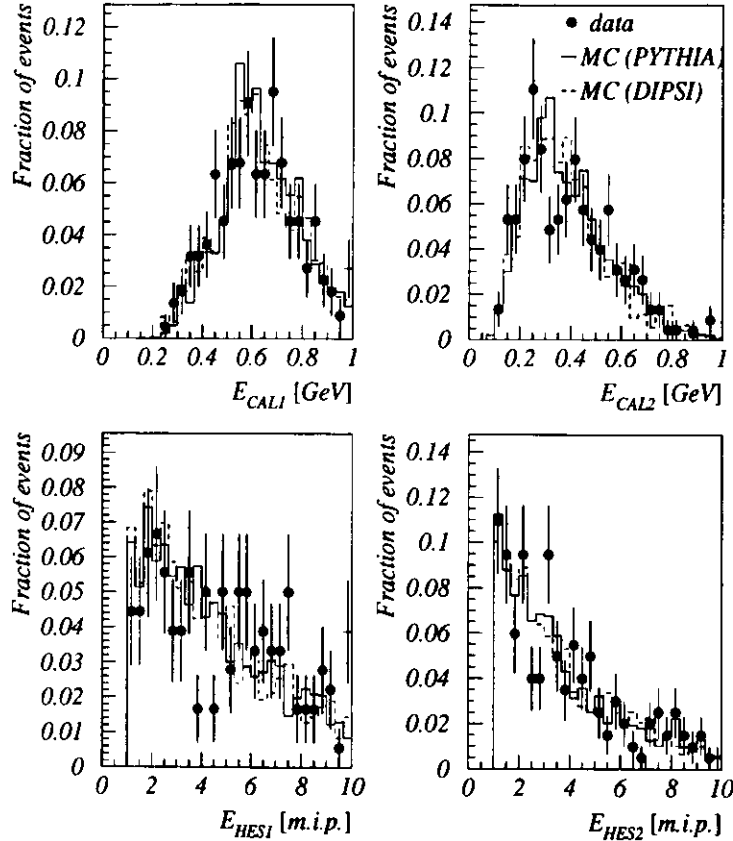


**Figure 5.9:** Comparison of the RCAL and RHES energy distributions  $E_{CAL1,2}$  and  $E_{HES1,2}$  of the two clusters between data and the two Monte Carlo generators.

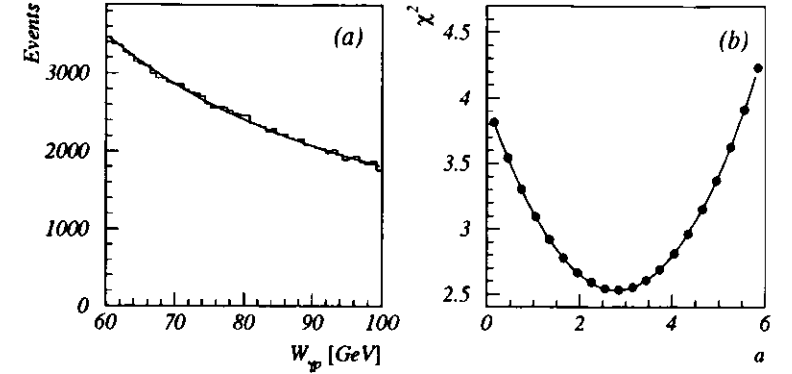


**Figure 5.10:** Dependence of the Monte Carlo simulation on the slope of  $W_{yp}$ : (a) demonstrates that the default Monte Carlo  $W_{yp}$  distribution on generator level can be described by a  $W_{yp}^{-\alpha}$  dependence (as given by the solid line). (b) shows the  $\chi^2$  given by equation (5.2) as a function of the  $W_{yp}$ -slope  $\alpha$  in the Monte Carlo. The solid line is a fit with a second order polynomial.

a change in the cross section of 2%. The decay angular distributions were changed by varying the matrix elements  $r_{00}^{04}$  and  $r_{1-1}^{04}$  within their statistical uncertainty as given in Section 5.6.3, each yielding a change in the cross section of 1%.

For the  $W_{yp}$  distribution no measured parameter was available. Thus the Monte Carlo spectrum was parametrized with a parameter  $\alpha$  according to a power-like dependence, i.e. proportional to  $W_{yp}^{-\alpha}$  as shown in Figure 5.10(a). Then the difference of the reconstructed  $W_{yp}$  values between data and Monte Carlo events was determined as a  $\chi^2$ -function of  $\alpha$ . The  $\chi^2$  was defined as [67]:

$$\chi^2(\alpha) = \sum_{\mu} \frac{(d_{\mu} - c_N m_{\mu}(\alpha))^2}{\sigma_{\mu}^2(\alpha)}, \quad (5.2)$$

where  $d_{\mu}$  is the number of data events in the  $W_{yp}$ -bin  $\mu$ ,  $m_{\mu}(\alpha)$  is the number of Monte Carlo events determined with parameter  $\alpha$  in the corresponding bin and  $c_N$  is a normalisation factor to ensure  $\sum_{\mu} d_{\mu} = c_N \sum_{\mu} m_{\mu}(\alpha)$ . The sigma - in the case of negligible Monte Carlo errors and unweighted data events - is given by  $\sigma_{\mu}^2 = c_N m_{\mu}$  [67]. The resulting  $\chi^2$  with the number of degrees of freedom being equal to three is shown in Figure 5.10(b). It fixes the slope to  $\alpha = 2.8 \pm 2.3$ . Variation of the  $W_{yp}$  distribution in the Monte Carlo samples according to the above statistical error of a yielded a change in the cross section of 1%.

The behaviour of the  $Q^2$  distribution could not be fixed by the data as the scattered positron is not measured in this analysis. Nevertheless, there is some uncertainty in the description of the  $Q^2$  spectrum: the behaviour as given by the flux in equation (2.25) depends on the VDM parameter

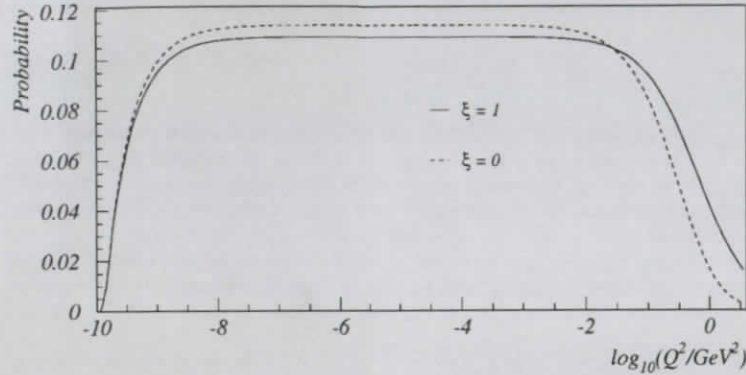


**Figure 5.11:** Probability distribution for  $\log_{10} Q^2$  as given by VDM for  $\xi = 1$  (solid line) and  $\xi = 0$  (dashed line).

$\xi$ . In the determination of the flux  $\xi$  was assumed to be one – which essentially reproduces the  $Q^2$  spectrum of the PYTHIA Monte Carlo –, but  $\xi$  could be smaller as discussed in Section 2.2.2. The probability distribution for  $Q^2$  changes accordingly as shown in Figure 5.11. Therefore the model dependence on  $Q^2$  was estimated by varying the  $Q^2$  spectrum in the Monte Carlo such that it would fit the case of  $\xi = 0$  and determining the effective photon flux accordingly. The corresponding change in the cross section was 2%.

## 5.3 Background

### 5.3.1 Photoproduction with Photon Dissociation

Photoproduction events with photon dissociation, where parts from the photon dissociative final state are lost in the beam pipe forming a state consisting of two charged particles and two neutral particles of an invariant mass in the region of  $m_\omega$ , are a possible source of background. To describe the behaviour of this background Monte Carlo events of the reaction  $\gamma p \rightarrow Xp$ , where  $X$  is a hadronic state produced by the dissociation of the photon, were generated using the PYTHIA generator in the kinematical range  $40 \leq W_{\gamma p} \leq 300 \text{ GeV}$  and  $Q_{min}^2 \leq Q^2 \leq 4 \text{ GeV}^2$ .

In approximately 17% of these events an  $\omega$  occurred in the final state. The efficiency of reconstructing only the  $\omega$  meson is  $10^{-5}$ . Therefore the contribution of this type of reaction to the resonant signal is negligible. Photon dissociation is only visible as smooth mass spectrum below the omega peak and is discussed in Section 5.5.2.

### 5.3.2 Photoproduction with Proton Dissociation

The main source of background is the inelastic reaction  $\gamma p \rightarrow \omega N$ , where  $N$  is a hadronic system produced by the dissociation of the proton. Many of these events could not be distinguished from the elastic scattering as the particles from the hadronization of the state  $N$  are often lost in the beam pipe. This background was statistically removed using the results of [5]. They use proton dissociative events identified by a significant energy deposit in the FCAL together with a PYTHIA Monte Carlo simulation of the reaction  $\gamma p \rightarrow \rho^0 N$  with a cross section of the form  $d^2\sigma/dtdm_N^2 \propto e^{-b|t|}/m_N^2$  ( $m_N$  being the mass of the state  $N$ ), with  $b = 4.5 \text{ GeV}^{-2}$  and  $\beta = 2.5$ . The latter allows an estimate of the total number of proton dissociative events  $N_{inel}$ , including those not identified by an FCAL energy deposit as given by the following equation [5]:

$$N_{inel} = \left\{ \frac{N(E_{FCAL} < 1 \text{ GeV})}{N(E_{FCAL} > 1 \text{ GeV})} \right\}_{MC} \cdot N(E_{FCAL} > 1 \text{ GeV})_{data}.$$

The resulting fraction of elastic events was parametrized as a function of  $p_T^2$ :

$$\frac{N_{el}}{N_{el} + N_{inel}} = 0.935 - 0.319 \text{ GeV}^{-2} p_T^2, \quad (5.3)$$

where  $N_{el}$  is the number of elastic events. The relative uncertainty on the correction was assumed to be the same as in [5], i.e. is given by the uncertainty on the parameters  $\beta$  and  $b$  of the Monte Carlo. A similar determination using the present data was not possible due to statistical limitations. The fraction of elastic  $\omega$  events as given by the above parametrization was applied as a weight to each measured event; its effect is to lower the cross section by  $16 \pm 9\%$ . The correction was extrapolated to  $p_T^2 = 0.6 \text{ GeV}^2$  from the range of the measurement presented in [5].

Another analysis of this background using  $\rho^0$  photoproduction reactions was carried out using a method based on the data of the FCAL energy and the signals in detectors in the forward region close to the beam pipe ("proton remnant tagger" PRT and "leading proton spectrometer" LPS), the latter allowing a distinction of elastic and proton dissociative events even if no significant energy was deposited in FCAL [39]. The resulting fraction of inelastic events was again parametrized as a function of  $p_T^2$ :

$$\frac{N_{inel}}{N_{el} + N_{inel}} = \frac{1}{A e^{-b p_T^2} + 1},$$

with:

$$\begin{aligned} A &= 7.34_{-2.85}^{+5.98}, \\ b &= 4.79 \pm 1.56 \text{ GeV}^{-2}. \end{aligned}$$

The corresponding effect on the cross section is a reduction by  $27 \pm 10\%$ .

### 5.3.3 Beam-Gas Interactions

Contamination from interactions of the proton or positron beam with the residual gas in the beam pipe was estimated from the unpaired bunches to be below 2%.

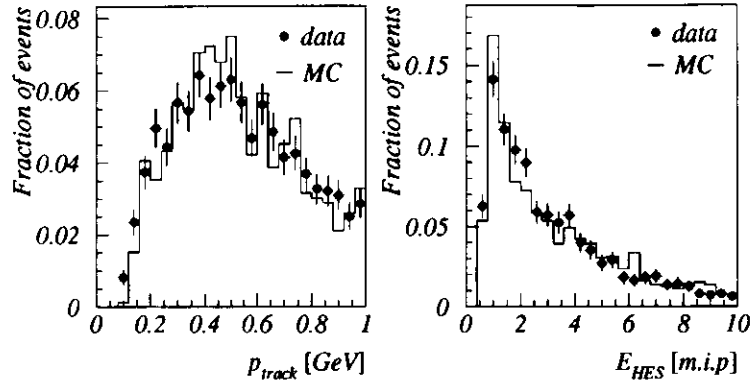


**Figure 5.12:** Track momentum (left) and HES energy spectrum (right) for conversion electrons. The dots are data while the histograms show Monte Carlo events.

## 5.4 Systematics

### 5.4.1 Checking the Cut on the RHES Energy

#### Conversion Electrons

As electrons have almost the same shower behaviour as photons, electrons from the conversion of photons in the beampipe identified by the CONVERT2 finder [68] were selected for a systematic study with well identified particles at sufficient statistics. The spectrum of the momentum of the tracks as well as the energy spectrum in the RHES for the conversion electrons with a momentum below 1 GeV is shown in Figure 5.12. A good agreement between data and Monte Carlo is visible. Applying a cut on the RHES energy of 1 mip, the efficiency in the data is  $84 \pm 3\%$ , while the same for Monte Carlo events results in an efficiency of  $88 \pm 3\%$ . Therefore the use of the RHES cut in the omega reconstruction in data is well reproduced by the Monte Carlo.

#### Photons from $\omega$ Production

Due to the slightly different shower behaviour of photons and electrons and as the amount of dead material in front of the calorimeter is not completely well known, the above might not represent the case of photons well enough. Therefore a second check using photons instead of electrons was done. Compared to the analysis using conversion electrons, it has the disadvantage of low statistics and relatively high contamination with events not from a  $\pi^0$  decay.

To this purpose the  $\omega$  analysis was run in a slightly different way, using no RHES and obtaining the full information about the photons from the  $\pi^0$  decay from the calorimeter alone. A cut on the number of condensates not associated with charged tracks exactly equal to two was applied. Assigning now existing RHES clusters to the two calorimeter condensates gives information about the efficiency of the cut on the RHES energy for photons: A fit to the three-pion mass spectrum requiring only the analysis cuts given in Section 5.1.2 plus a cut on the three-pion mass ( $|m_{3\pi} - m_\omega| < 0.1$  GeV) and additionally requiring that both calorimeter condensates should have an assigned RHES cluster with at least 1 m.i.p., respectively, and dividing the numbers of found  $\omega$  candidates gives the wanted efficiency. In data it was found to be  $39 \pm 5\%$ , while the same procedure on Monte Carlo events gives  $38 \pm 2\%$ , where the error given is only statistical. The values are in good agreement and therefore the simulation of the RHES spectrum in Monte Carlo events is in accordance to the data.

### 5.4.2 Systematic Errors

Most contributions to the systematic error were estimated by changing the various cuts applied in the analysis. The following list describes this:

- cut on the energy of the RCAL condensates  $E_{CAL}$  changed from 100 MeV to 150 MeV;
- cut on the energy  $E_{3rd}$  of the third unused condensate in RCAL (if present) changed from 200 to 500 MeV;
- cut on the energy of the RHES clusters  $E_{HES}$  changed from 1 m.i.p to 1.5 m.i.p;
- cut on the energy of the RHES clusters  $E_{HES}$  changed from 1 m.i.p to 0.8 m.i.p only in Monte Carlo to account for a possible over-calibration of 20% in the data (see Section 4.1.2);
- cut on the invariant mass of the two photon system  $m_{\gamma\gamma}$  changed from 40 MeV around the peak to 30 MeV and 50 MeV; the maximum of the changes in the cross section was used;
- cut on the pseudorapidity of the tracks  $\eta$  changed from  $-2.0$  by  $\pm 0.1$ ,
- cut on the transverse momentum of the tracks  $p_{Ttrack}$  changed from 100 to 150 MeV;
- cut on the reconstructed  $W_{\gamma p}$  changed by 6% according to the resolution either in both Monte Carlo and data or only in Monte Carlo (the latter estimating effects of miscalibration).

Further sources of the systematic error have been taken into account:

- the relative error in the subtraction of proton dissociative reactions<sup>3</sup>  $\gamma p \rightarrow \omega N$  and the effect of radiative corrections were adopted from [5];
- the model dependence of the acceptance determination was estimated by changing the distributions of  $Q^2$ ,  $W_{\gamma p}$ ,  $t$  and the  $\omega$  decay angles in the Monte Carlo simulation within the statistical uncertainties allowed by the data (see Section 5.2.2).

<sup>3</sup>The amount of proton dissociative events contained in the sample as a function of  $p_T^2$  was assumed to be that obtained in the  $\rho^0$  analysis [5], see Section 5.3.2.

- the uncertainty of the trigger efficiency was estimated using the uncertainty on the parameters of the fits on the efficiency of the RCAL-EMC-cut as given in Section 5.2.1;
- the systematic error in the luminosity measurement is discussed in [69].

The quantitative results of these checks are discussed together with the determination of the cross sections in Section 5.6.

## 5.5 Analysis of the Mass Spectrum

### 5.5.1 Evaluation of the Number of Events

The spectrum of the invariant mass of the  $\pi^+\pi^-\pi^0$  system  $m_{3\pi}$  after all offline cuts and the fit constraining the  $\gamma\gamma$  mass according to equation (5.1) is shown in Figure 5.13(a). In addition to the  $\omega$  signal, a second one is visible, which is due to the elastic photoproduction of the  $\phi$  meson,  $\gamma p \rightarrow \phi p$  ( $\phi \rightarrow \pi^+\pi^-\pi^0$ ). For comparison, the invariant mass as given by the Monte Carlo simulations for the reaction  $\gamma p \rightarrow \omega p$  and  $\gamma p \rightarrow \phi p$  is shown in Figure 5.13(b). The spectra were fitted with the function:

$$f(m_{3\pi}) = g_1(m_{3\pi}) + g_2(m_{3\pi}) + \zeta(m_{3\pi}), \quad (5.4)$$

where  $g_1$ ,  $g_2$  are convolutions of a non-relativistic Breit-Wigner function<sup>4</sup> with a Gaussian to describe the  $\omega$  and  $\phi$  resonances.  $\zeta$  is a third order polynomial representing the background, mainly due to contamination under the  $\pi^0$  peak and to inelastic processes in which a  $\pi^0$  is produced (see below). The fitted values of the  $\omega$  and  $\phi$  masses in data are  $778 \pm 3$  MeV and  $1020 \pm 9$  MeV, respectively, compatible with those of the Particle Data Group (PDG) [23]. The corresponding values of the Gaussian standard deviations are  $32 \pm 4$  MeV and  $26 \pm 11$  MeV, respectively; they are a measure of the resolution of the apparatus. The results of the fits to the two Monte Carlo samples are:  $781 \pm 2$  MeV and  $1016 \pm 3$  MeV for the masses and  $32 \pm 2$  MeV and  $27 \pm 3$  MeV for the standard deviations. The agreement with the data is good.

The number of  $\omega$  and  $\phi$  candidates observed after background subtraction was determined by integrating the fitted Breit-Wigner functions within the kinematic limits. This yielded  $N_\omega = 172 \pm 17$  and  $N_\phi = 38 \pm 15$ .

### 5.5.2 Background Below the Resonances

#### Description of the Mass Distribution

Below the peaks of the  $\omega$  and  $\phi$  resonances, the spectrum of the invariant mass of the  $\pi^+\pi^-\pi^0$  system  $m_{3\pi}$  shows a continuum. Two sources are assumed to produce a continuum like this:

- (a) Events without a  $\pi^0$  resonance, visible as continuous background in the spectrum of the invariant mass of the two neutral clusters,  $m_{\gamma\gamma}$ . This can be studied using data, namely

<sup>4</sup>The widths of the Breit-Wigner functions were fixed to the measured values [23] rather than being subject to the fit.

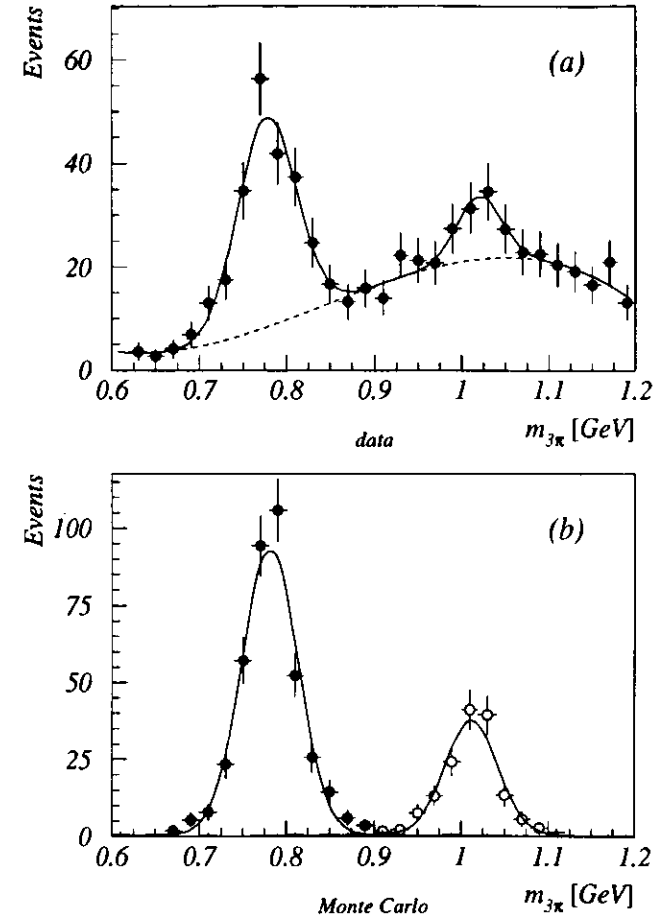


**Figure 5.13:** Invariant mass distribution of the  $\pi^+\pi^-\pi^0$  system after all offline cuts and the fit based on equation (5.1). (a) shows the data, (b) Monte Carlo events from  $\gamma p \rightarrow \omega p$  (solid circles) and  $\gamma p \rightarrow \phi p$  (open circles). The full line is a fit based on equation (5.4); the dashed line indicates the background as determined by the fits.

the non-resonant tail in the  $m_{\gamma\gamma}$  spectrum. Figure 5.14 shows the spectrum of the invariant mass of the  $\pi^+\pi^-\gamma\gamma$  system  $m(\pi^+\pi^-\gamma\gamma)$  for all offline cuts, except replacing the cut  $84 \leq m_{\gamma\gamma} \leq 164$  MeV by  $m_{\gamma\gamma} \geq 200$  MeV.

- (b) Photoproduction events with photon dissociation. To describe the behaviour of this background, the above described Monte Carlo events for the reaction  $\gamma p \rightarrow Xp$  were used. Reconstructing these events in the same way as the data yields an  $m(\pi^+\pi^-\gamma\gamma)$  spectrum as shown in Figure 5.15. Thereby a distinction between events with and without a detected  $\pi^0$  was made. In the following, only the events with a  $\pi^0$  are used to avoid double counting with the events already contained in background (a).

To adjust the background  $m_{3\pi}$  spectra to the data, two regions were defined where no contributions from either of the  $\omega$  and  $\phi$  resonances are expected: (1)  $600 \leq m_{3\pi} \leq 700$  MeV and (2)  $1100 \leq m_{3\pi} \leq 1200$  MeV. In region (1) the contribution from background (b) is negligible. Therefore this part was used to adjust background (a), requiring the number of events in sample (a) and the data to be equal. This results in a scaling of (a) of 0.47. An estimate of the non-resonant part of events below the  $\pi^0$  peak in the  $m_{\gamma\gamma}$  spectrum results in a number of events of about 0.55 times the number of events with  $m_{\gamma\gamma} \geq 200$  MeV, which is in reasonable agreement with the above scaling. To adjust background (b), the number of events of this sample is required to be equal to the difference of the number of events in data and in the adjusted spectrum of (a) in region (2). The necessary scaling of background (b) is 5. As the effective photon flux is 0.133 for the reaction  $\gamma p \rightarrow Xp$  in the generated kinematic range, this corresponds to a cross section of  $\sigma^{\gamma p \rightarrow Xp} \approx 17 \mu\text{b}$ . It is in agreement with measurements of the cross section ( $\sigma^{\gamma p \rightarrow Xp} = 13 \pm 3 \mu\text{b}$  or  $23 \pm 11 \mu\text{b}$ ) [70].

To visualize how well these models of the continuous  $m_{3\pi}$  background fit to the data, the spectrum of type (b) was smoothed, as the small statistics causes large fluctuations. The sum of the number of events of this spectrum and the spectrum of type (a) in comparison with the data is shown in Figure 5.16. The agreement is good.

### Number of Events

To check whether the approach by the fit given in equation (5.4) is in agreement with the above description of the background, the following was done: as the statistical reliability of the description of background (b) is quite bad and the contribution to the spectrum in the lower  $m_{3\pi}$  range is small, the investigated  $m_{3\pi}$ -region was restricted to  $m_{3\pi} \leq 900$  MeV. This allows the use of background (a) only. Now background and signal regions were distinguished, which were defined as

- (1) background:  $600 \leq m_{3\pi} \leq 700$  MeV or  $860 \leq m_{3\pi} \leq 900$  MeV and
- (2) signal:  $700 \leq m_{3\pi} \leq 860$  MeV.

Adjusting then the number of events of background (a) to the data in the background region yielded a slightly higher scaling than before (0.58). The subtraction of the number of events in data and the adjusted background gave then the number of  $\omega$  events:  $N_\omega(\text{subtr.}) = 175 \pm 16$ . This is in good agreement with the above result from the fit.

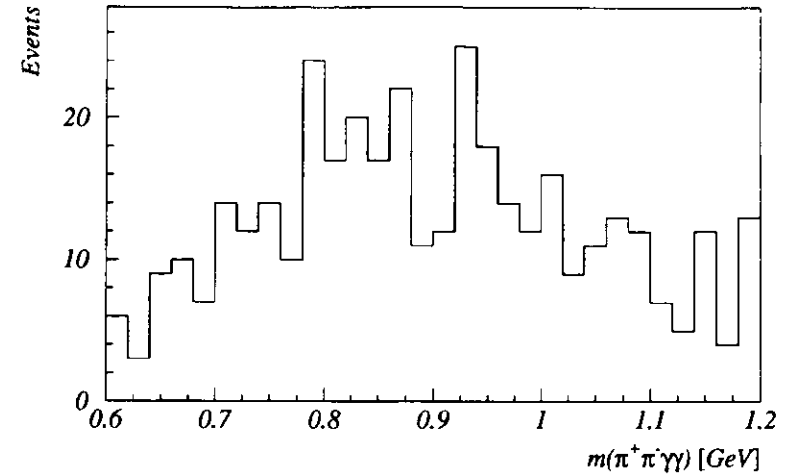


Figure 5.14: Mass spectrum  $m(\pi^+\pi^-\gamma\gamma)$  for the background of type (a) from data with  $m_{\gamma\gamma} \geq 200$  MeV.

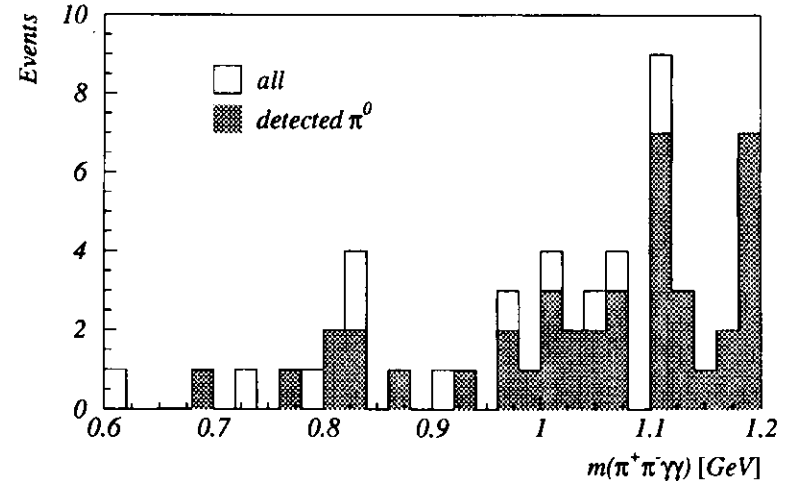
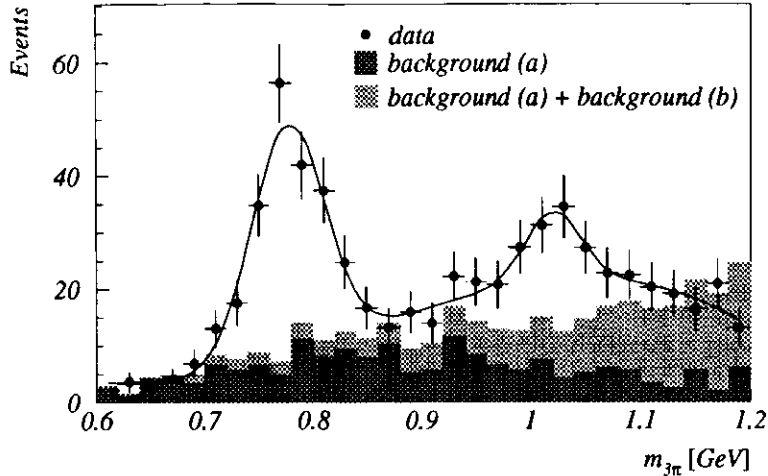


Figure 5.15: Spectrum of  $m(\pi^+\pi^-\gamma\gamma)$  for the background of type (b) as given by the Monte Carlo for  $\gamma p \rightarrow Xp$  as described in the text. The hatched histogram shows the fraction of events with a detected  $\pi^0$ .





**Figure 5.16:** The backgrounds of type (a) and type (b) (histograms) compared to the data (solid circles) via the  $m_{3\pi}$  spectrum.

## 5.6 Results

### 5.6.1 Elastic $\gamma p \rightarrow \omega p$ Cross Section

The elastic  $\gamma p \rightarrow \omega p$  cross section is given by:

$$\sigma^{\gamma p \rightarrow \omega p} = \frac{N_\omega}{\epsilon \Phi \mathcal{L} B},$$

where  $N_\omega$  is the total number of observed events after the statistical subtraction of the inelastic background as given in Section 5.5.1,  $\epsilon$  is the total acceptance as given in Section 5.2.2,  $\mathcal{L}$  is the effective integrated luminosity as given in Section 5.1.1 and  $\Phi = 0.0203$  is the effective photon flux as given by equation (2.25) after integration over the selected  $W_{\gamma p}$  and  $Q^2$  ranges. The branching ratio of the  $\omega \rightarrow \pi^+ \pi^- \pi^0$  ( $\pi^0 \rightarrow \gamma\gamma$ ) decay is  $B = B_{\omega \rightarrow 3\pi} \cdot B_{\pi^0 \rightarrow \gamma\gamma} = 0.877$  [23]. In the region of  $|t| < 0.6 \text{ GeV}^2$ , and averaged over the range  $70 < W_{\gamma p} < 90 \text{ GeV}$ , the cross section is:

$$\sigma^{\gamma p \rightarrow \omega p} = 1.21 \pm 0.12(\text{stat.}) \pm 0.23(\text{syst.}) \mu\text{b}.$$

The systematic error was obtained by adding in quadrature the individual contributions listed in the second column of Table 5.2; the dominant ones are from the acceptance calculation and the inelastic background subtraction.

The resulting elastic  $\gamma p \rightarrow \omega p$  cross section at an average energy of  $(W_{\gamma p}) = 80 \text{ GeV}$  is shown in Figure 5.17 together with previous results from fixed target experiments [20, 25, 26, 27, 28, 29, 71, 72, 73, 74, 75, 76]. The  $W_{\gamma p}$  dependence of the cross sections in the range  $10 < W_{\gamma p} < 100 \text{ GeV}$

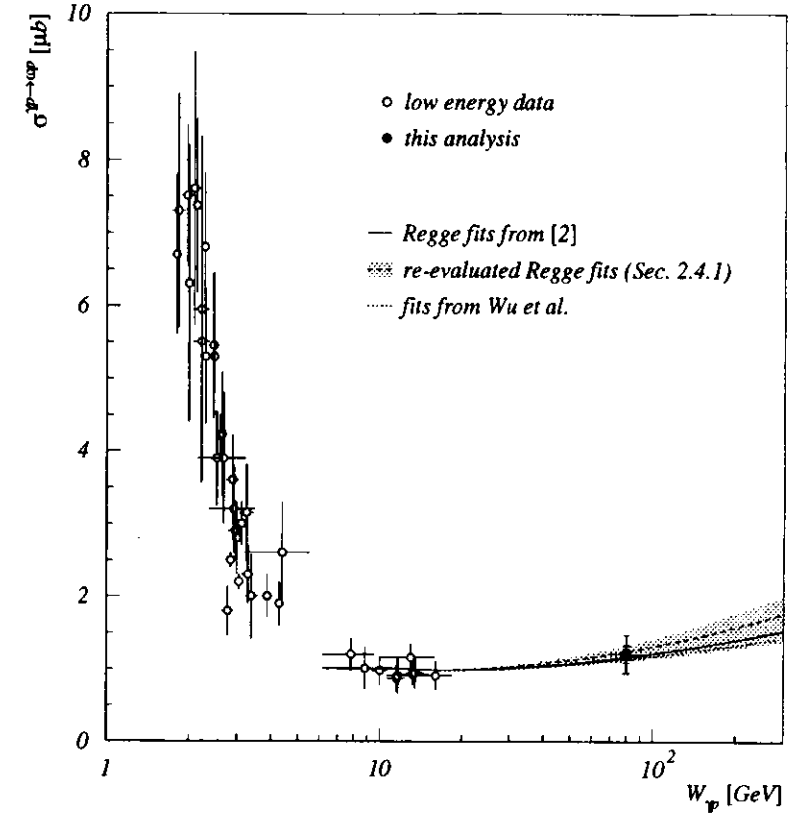


**Figure 5.17:** The elastic  $\gamma p \rightarrow \omega p$  cross section measured in this analysis (solid circle) compared with the results of fixed target experiments [20, 25, 26, 27, 28, 29, 71, 72, 73, 74, 75, 76] (open circles). For the measurement of this analysis the inner part of the vertical error bar shows the statistical error, while the outer one shows the statistical and systematic errors added in quadrature. The horizontal bars indicate the  $W_{\gamma p}$  range covered by the measurements. The solid line is a parametrization based on Regge fits to hadronic data of [2], while the dashed line is a re-evaluation of these fits (see Section 2.4.1) where the shaded area gives the uncertainty on the cross section estimated by the uncertainty of the Pomeron intercept. The dotted line is based on a parametrization of hadronic data from Wu et al. (see Section 2.4.2).

check	$\sigma^{\gamma p \rightarrow \omega p}$	$b$	$A$
cut on $E_{CAL}$	3%	8%	7%
cut on $E_{3rd}$	2%	6%	11%
cut on $E_{HES}$	7%	6%	8%
calibration of $E_{HES}$	4%	1%	5%
cut on $m_{\gamma\gamma}$	9%	1%	1%
cut on $\eta_{Track}$	3%	1%	1%
cut on $p_{Track}$	3%	1%	1%
cut on $W_{\gamma p}$	3%	1%	1%
inel. backgr. subt.	11%	-	11%
rad. corrections	4%	-	4%
luminosity	1.5%	-	1.5%
model dependence	3%	4%	9%
trigger efficiency	6%	0%	6%
total	19%	13%	22%

Table 5.2: List of the various contributions to the systematic error in  $\sigma^{\gamma p \rightarrow \omega p}$ ,  $b$  and  $A$ .

is found to be weak, as predicted by fits to hadronic cross sections (see Sections 2.4.1 and 2.4.2). A distinction between the different models is not possible.

As a consistency check, the elastic  $\gamma p \rightarrow \phi p$  cross section was determined, using  $B = B_{\phi \rightarrow 3\pi} \cdot B_{\pi^0 \rightarrow \gamma\gamma} = 0.154$  [23] and  $\Phi = 0.0207$ , resulting in  $\sigma^{\gamma p \rightarrow \phi p} = 0.9 \pm 0.3(\text{stat.}) \mu\text{b}$ . This value agrees with  $\sigma^{\gamma p \rightarrow \phi p} = 0.96 \pm 0.19^{+0.21}_{-0.18} \mu\text{b}$  determined using the reaction  $\gamma p \rightarrow \phi p$  ( $\phi \rightarrow K^+ K^-$ ) in the kinematic range  $60 < W_{\gamma p} < 80 \text{ GeV}$  and  $|t| < 0.5 \text{ GeV}^2$  [6].

### 5.6.2 Differential Cross Section $d\sigma^{\gamma p \rightarrow \omega p}/d|t|$

In order to derive the differential cross section  $d\sigma^{\gamma p \rightarrow \omega p}/d|t|$ , the fit to the mass spectrum described in Section 5.5.1 was repeated in bins of  $p_T^2$ . Equation (2.21) could in principle be used to derive the  $t$  distribution from this. But this approximation is only valid for small  $Q^2$ , large values of  $Q^2$  cause  $p_T^2$  to be larger than  $|t|$ ; in fact one has  $p_T^2 \geq |t|$ , where equality occurs for  $Q^2 = 0$ . Thus instead of correcting with the acceptance shown in Figure 5.7, a bin-by-bin correction, given by the ratio of the generated  $|t|$  and the reconstructed  $p_T^2$  distribution in the PYTHIA Monte Carlo sample, was used to derive the measured  $|t|$  distribution. The effect of the correction for the difference between  $p_T^2$  and  $|t|$  is shown in Figure 5.18 as a function of  $|t|$ ;  $F$  denotes the fraction of number of events with generated  $p_T^2$  being in the bin range to those with  $|t|$  being in the bin range as given by the PYTHIA Monte Carlo sample.

The resulting  $d\sigma^{\gamma p \rightarrow \omega p}/d|t|$  is shown in Figure 5.19(a), where the points are positioned at the mean value of  $|t|$  in each bin rather than the centre of each bin. The data were fitted in the range  $0 < |t| < 0.6 \text{ GeV}^2$  using the functional form:

$$\frac{d\sigma^{\gamma p \rightarrow \omega p}}{d|t|} = A \cdot e^{-b|t|}, \quad (5.5)$$

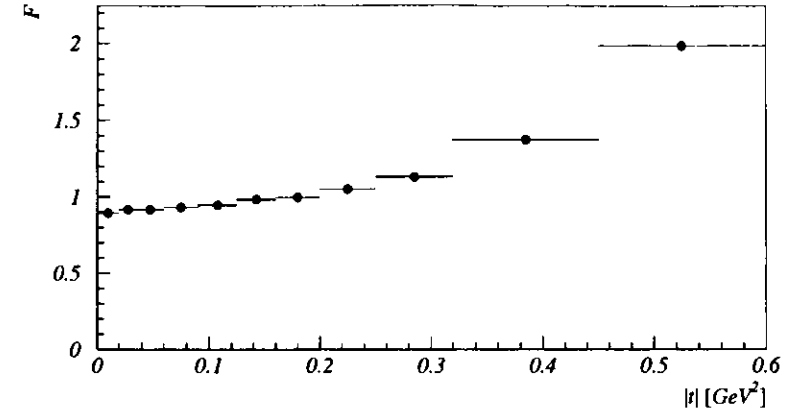


Figure 5.18: Correction function  $F$  describing the conversion of the  $p_T^2$  distribution into one in  $|t|$ .

yielding:

$$A = 10.7 \pm 2.2(\text{stat.}) \pm 2.3(\text{syst.}) \frac{\mu\text{b}}{\text{GeV}^2},$$

$$b = 10.0 \pm 1.2(\text{stat.}) \pm 1.3(\text{syst.}) \text{GeV}^{-2}.$$

The systematic error in  $A$  is dominated by the uncertainty on the acceptance (sensitivity to cuts and model dependence); the single contributions are listed in the last column of Table 5.2. The dominant contribution to the systematic error in  $b$  is also the uncertainty on the acceptance; the single contributions are listed in the third column of Table 5.2.

The slope  $b$  is compared in Figure 5.19(b) with the results of previous experiments [20, 25, 26, 28, 29, 72, 73]. From a study of diffractive hadronic processes, assumed to be mediated by Pomeron exchange, Regge theory yields the dependence of the slope  $b$  as given by equation (2.52) with  $\alpha'_P = 0.25 \text{ GeV}^{-2}$ . The line shown in Figure 5.19(b) represents the dependence according to equation (2.52), with  $b_0$  chosen such that it passes through the ZEUS point. This behaviour is in good agreement with the data points at high energies ( $W_{\gamma p} > 10 \text{ GeV}$ ), where equation (2.52) is expected to hold.

### 5.6.3 Decay Angular Distributions

The polar and azimuthal angles  $\theta_h$  and  $\phi_h$  of the normal to the  $\omega$  meson decay plane in the  $s$ -channel helicity frame were used to determine elements of the  $\omega$  spin-density matrix as described

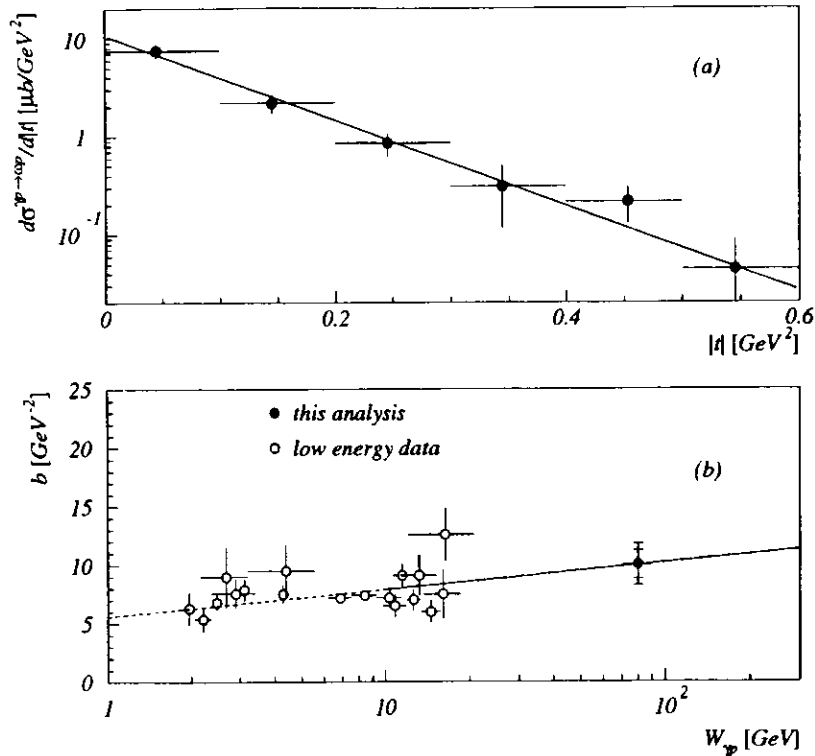


**Figure 5.19:** (a) The differential cross section  $d\sigma^{\gamma p \rightarrow \omega p}/d|t|$ ; the line shows the result of the fit with functional form (5.5). (b) Exponential slope  $b$  of  $d\sigma^{\gamma p \rightarrow \omega p}/d|t|$  as observed in this analysis (solid circle) compared with low energy data [20, 25, 26, 28, 29, 72, 73] (open circles). For the measurements of this analysis the inner part of the vertical error bar shows the statistical error, while the outer one shows the statistical and systematic errors added in quadrature. The horizontal bars indicate the  $W_{\gamma p}$  range covered by the measurements. The line is given by equation (2.52). It was constrained to pass through the data point of this analysis.

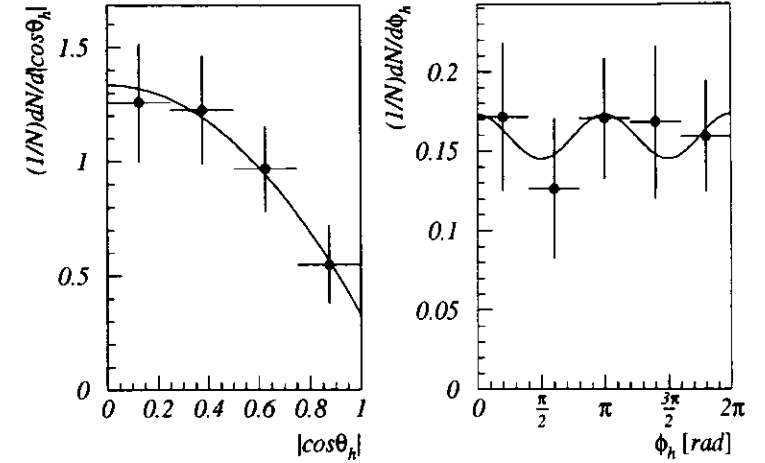


**Figure 5.20:** Acceptance corrected distribution of  $|\cos\theta_h|$  and  $\phi_h$ , where  $\theta_h$  and  $\phi_h$  are the polar and azimuthal angles of the  $\omega$  meson decay plane in the  $s$ -channel helicity frame, respectively. Fits according to equations (2.29) and (2.30) are superimposed.

in Section 2.3.3. The direction of the normal was defined as that of  $\vec{\pi}^+ \times \vec{\pi}^-$ , where  $\vec{\pi}^+$  ( $\vec{\pi}^-$ ) is the three momentum of the positively (negatively) charged pion. The experimental resolution in  $\cos\theta_h$  is about 0.05 and in  $\phi_h$  about 0.8 rad. Upon averaging over  $\phi_h$  or  $\cos\theta_h$  one expects, respectively, the behaviour as given by equations (2.29) and (2.30). As the distribution of  $\cos\theta_h$  was found to be symmetric,  $|\cos\theta_h|$  was considered instead. The acceptance corrected distributions of  $|\cos\theta_h|$  and  $\phi_h$  are shown in Figure 5.20. They were obtained by repeating the mass fits described in Section 5.5.1, applied in each bin of  $|\cos\theta_h|$  and  $\phi_h$ . Fits of the functions (2.29) and (2.30) to the corrected data yield:

$$r_{00}^{04} = 0.11 \pm 0.08(\text{stat.}) \pm 0.26(\text{sys.})$$

and:

$$r_{1-1}^{04} = -0.04 \pm 0.08(\text{stat.}) \pm 0.12(\text{sys.}).$$

Both values are compatible with the prediction of  $s$ -channel helicity conservation: by assuming  $R = Q^2/m_\omega^2$  for the ratio  $R$  of the longitudinal to the transverse  $\gamma^*p$  cross section from VDM as given by equations (2.22) and (2.23) and taking the mean assuming a  $Q^2$  probability as given by equation (2.25), equation (2.31) yields  $r_{00}^{04} = 0.10$ . The expectation for the other matrix element is  $r_{1-1}^{04} = 0$  (see Appendix A).

### 5.6.4 The Total $\omega p$ Cross Section

Using equation (2.32), the total  $\omega$  proton cross section  $\sigma^{\omega p}$  was determined. With  $\left. \frac{\sigma^{\gamma p \rightarrow \omega p}}{d|t|} \right|_{t=0} = 10.7 \mu\text{b}/\text{GeV}^2$  (see above) and  $f_\omega^2/4\pi = 24.6$  as given by Table 2.3, one gets:

$$\sigma^{\omega p} = 27.5 \pm 2.8(\text{stat.}) \pm 3.4(\text{syst.}),$$

where the systematic error includes the error of  $\left. \frac{\sigma^{\gamma p \rightarrow \omega p}}{d|t|} \right|_{t=0}$  and the error of  $f_\omega^2/4\pi$ . The value agrees with the expected value of  $29 \pm 1 \text{ mb}$  at  $W = 80 \text{ GeV}$  obtained from the parametrizations of Sections 2.4.1 and 2.4.2, where the error was estimated from the differences between the parametrizations.

### 5.6.5 The $\gamma \leftrightarrow \omega$ Coupling Constant

Using on the other hand the predictions for  $\sigma^{\omega p}$  from the parametrizations of Sections 2.4.1 and 2.4.2, the  $\gamma \leftrightarrow \omega$  coupling constant can be determined with equation (2.32) to:

$$\frac{f_\omega^2}{4\pi} = 29.3 \pm 6.0(\text{stat.}) \pm 6.6(\text{syst.}),$$

where the systematic error is given by that of  $\left. \frac{\sigma^{\gamma p \rightarrow \omega p}}{d|t|} \right|_{t=0}$  and the above on the prediction of  $\sigma^{\omega p}$ . The value is in good agreement with the result of  $24.6 \pm 3.8$  given in Table 2.3.

## Chapter 6

# Comparison of Elastic Photoproduction of $\rho^0$ , $\omega$ and $\phi$ Mesons

The ratio of the cross sections of elastic photoproduction of the three light vector mesons  $\rho^0, \omega, \phi$  can be estimated using the SU(6) quark model [7] as discussed in Section 6.3. In Section 6.1 the above result for the elastic photoproduction of  $\omega$  mesons is compared with existing measurements of the elastic photoproduction of  $\rho^0$  and  $\phi$  mesons using the ZEUS detector. In Section 6.2 the ratio of  $\omega$  to  $\phi$  photoproduction cross sections is specified detecting both particles in the same measurement via the decay into  $\pi^+ \pi^- \pi^0$ .

### 6.1 Comparison with Existing Measurements of Elastic $\rho^0$ and $\phi$ Photoproduction

The cross sections for the elastic photoproduction of  $\rho^0$  and  $\phi$  mesons were measured by the H1 and ZEUS collaboration as well [5, 6, 38, 39]. For the comparison of the elastic  $\omega$  photoproduction cross section to those of  $\rho^0$  and  $\phi$ , the following results from ZEUS were used:

- $\gamma p \rightarrow \rho^0 p$  at  $W_{\gamma p} = 75 \text{ GeV}$  [39]:  $\sigma^{\gamma p \rightarrow \rho^0 p} = 11.10 \pm 0.18 \pm 1.75 \mu\text{b}$ ;
- $\gamma p \rightarrow \omega p$  at  $W_{\gamma p} = 80 \text{ GeV}$  (see Section 5.6.1):  $\sigma^{\gamma p \rightarrow \omega p} = 1.21 \pm 0.12 \pm 0.23 \mu\text{b}$ ;
- $\gamma p \rightarrow \phi p$  at  $W_{\gamma p} = 70 \text{ GeV}$  [6]:  $\sigma^{\gamma p \rightarrow \phi p} = 0.96 \pm 0.19^{+0.21}_{-0.18} \mu\text{b}$ .

Ignoring the slight differences in  $W_{\gamma p}$ , the ratios between the three cross sections are thus:

$$\sigma^{\gamma p \rightarrow \rho^0 p} : \sigma^{\gamma p \rightarrow \omega p} : \sigma^{\gamma p \rightarrow \phi p} = 9.17 \pm 0.92 \pm 2.27 : 1 : 0.79 \pm 0.18 \pm 0.24, \quad (6.1)$$

where the first error given is the statistical, the second the systematic.

## 6.2 Evaluation of the $\omega$ to $\phi$ Cross Section Ratio in the $\pi^+\pi^-\pi^0$ Decay Mode

As already mentioned in Section 5.5.1, in addition to the  $\omega$  signal the spectrum of the invariant mass of the  $\pi^+\pi^-\pi^0$  system shows a peak due to the elastic photoproduction of the  $\phi$  meson in the decay mode  $\phi \rightarrow \pi^+\pi^-\pi^0$ . This allows to determine the ratio  $\sigma^{\gamma p \rightarrow \omega p} : \sigma^{\gamma p \rightarrow \phi p}$  in a way alternative to the above one. Especially as both cross sections have similar sources of systematic uncertainties, using the same data and the same decay mode of the mesons is expected to give a smaller systematic uncertainty on  $\sigma^{\gamma p \rightarrow \omega p} : \sigma^{\gamma p \rightarrow \phi p}$ . In addition, the measurement via the  $\phi \rightarrow \pi^+\pi^-\pi^0$  decay mode has the advantage of covering the whole  $t$  range rather than requiring an extrapolation to  $|t| < 0.1 \text{ GeV}^2$  as necessary in the measurement using the  $\phi \rightarrow K^+K^-$  decay [6].

### 6.2.1 Event Selection and Reconstruction

To increase the statistics of the analysed sample, the data taken in 1995 were used for the determination of  $\sigma^{\gamma p \rightarrow \omega p} : \sigma^{\gamma p \rightarrow \phi p}$ . They correspond to a total integrated luminosity of  $6.4 \text{ pb}^{-1}$ . Due to technical reasons some runs had to be excluded reducing the total integrated luminosity to  $5.7 \text{ pb}^{-1}$ .

#### Trigger

The trigger used in 1995 changed on SLT and TLT level but was the same on FLT level as in 1994, i.e. as given in Section 5.1.1. The requirements at the SLT were:

- number of reconstructed tracks less than four,
- the absolute  $Z$  value of the reconstructed vertex must be within 60 cm or if no vertex could be reconstructed the number of unmatched CTD segments must be less than 15,
- reject events with calorimeter timing indicating that the event has occurred upstream of the interaction point.

At TLT level the following conditions were required (" $\omega$  bit"):

- number of vertices equal to one and number of reconstructed tracks equal to two,
- the absolute  $Z$  value of the reconstructed vertex must be within 66 cm,
- number of CAL clusters not matched to a track must be within 2 and 6,
- invariant mass of the tracks assuming pion masses and any pair of CAL clusters assuming zero masses must be less than  $1.5 \text{ GeV}$ ,
- tighter cuts on calorimeter timing.

To reduce the rate of the trigger, only every 2nd to 4th (run-dependent) event was saved and written to tape. The effective integrated luminosity of this bit is almost  $1.8 \text{ pb}^{-1}$ .

Due to this prescale, the additional use of further trigger bits at TLT level increases the effective integrated luminosity. Two additional bits were considered: the " $\rho$  bit":

- number of vertices equal to one and number of reconstructed tracks less than three,
- all tracks fitted to the vertex or number of reconstructed tracks equal to two if only one track could be fitted to the vertex,
- the absolute  $Z$  value of the reconstructed vertex must be within 66 cm,
- tighter cuts on calorimeter timing;

and the " $\phi$  bit":

- number of vertices equal to one and number of reconstructed tracks equal to two,
- the absolute  $Z$  value of the reconstructed vertex must be within 66 cm,
- the invariant mass of the tracks must be less than  $0.6 \text{ GeV}$  assuming pion masses,
- tighter cuts on calorimeter timing.

Using a logical and of all three TLT trigger bits decreases the efficiency but allows to use the data having passed all bits increasing the effective integrated luminosity to almost  $2.8 \text{ pb}^{-1}$ . This possibility was chosen as a systematic check as the use of all these trigger bits gives a sample which is partially statistical independent from the one selected only by the  $\omega$  bit. Nevertheless, the latter was used for the analysis itself.

#### Offline Selection and Reconstruction

The selection criteria of 1994 as described in Section 5.1.2 were used again yielding a sample of 1433 events in total.

The  $\pi^0$  meson was reconstructed as described in Section 5.1.3 except the correction for the inactive material between interaction point and the RCAL. Instead the presampler in front of RCAL was used as described in Section 4.2.4. The spectrum of the invariant mass  $m_{\gamma\gamma}$  of the two clusters for data and the below described Monte Carlo simulation is plotted in Figure 6.1. A fit with the sum of a Gaussian and a second order polynomial yields a mean of the Gaussian of  $\langle m_{\gamma\gamma} \rangle = 132 \pm 1 \text{ MeV}$  and a standard deviation of  $28 \pm 1 \text{ MeV}$  for the data and a mean of the Gaussian of  $\langle m_{\gamma\gamma} \rangle = 133 \pm 1 \text{ MeV}$  and a standard deviation of  $26 \pm 1 \text{ MeV}$  for the Monte Carlo, which is in good agreement. Events with  $92 < m_{\gamma\gamma} < 172 \text{ MeV}$  were selected.

After constraining the RCAL energies to the  $\pi^0$  mass as given by equation (5.1) the  $\omega$  or  $\phi$  candidate was reconstructed as described in Section 5.1.4.

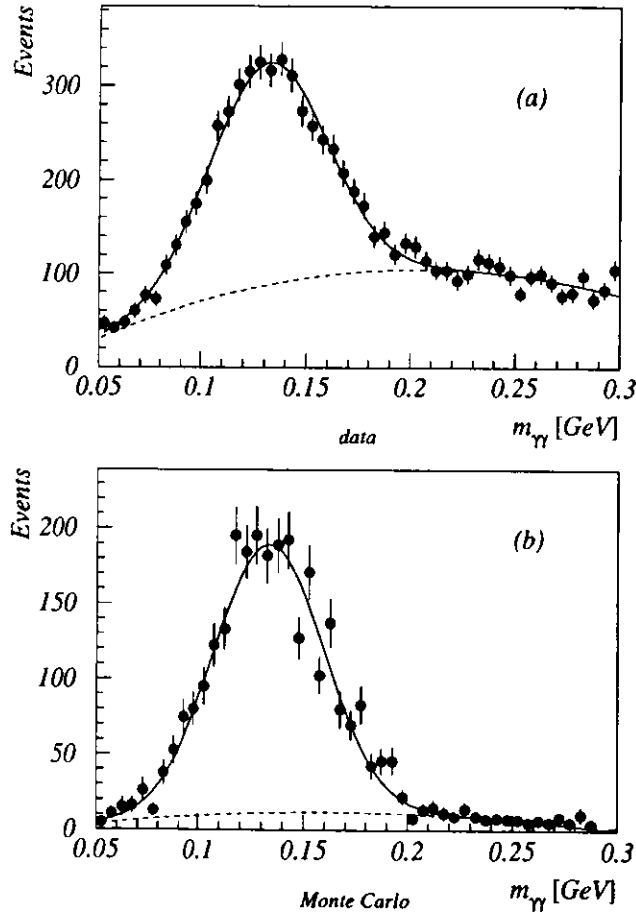


**Figure 6.1:** Invariant mass distributions of the two photons for (a) data and (b) Monte Carlo. The full line is the result of the fit explained in the text. The dashed line indicates the background as determined by the fit.

### 6.2.2 Acceptance Calculation

For the determination of the acceptance for the elastic photoproduction of  $\omega$  and  $\phi$ , again the generator PYTHIA was used (see Section 5.2.2). The events were generated in the kinematic range  $60 \leq W_{\gamma p} \leq 100$  GeV and  $Q_{min}^2 \leq Q^2 \leq 4$  GeV<sup>2</sup>. In order to adjust the Monte Carlo calculation to the data, the results from Section 5.6 or [6] were used, respectively.

The average acceptances for  $\omega$  and  $\phi$  photoproduction were evaluated in the region  $70 < W_{\gamma p} < 90$  GeV and  $|t| < 0.6$  GeV<sup>2</sup>. For simplicity, the RCAL-FLT efficiency was simulated with the Monte Carlo as well as no significant difference between the data driven method and the Monte Carlo was found in the 1994 analysis (see Section 5.2.1). The ratio of the acceptances was found to be  $\epsilon_\omega/\epsilon_\phi = 0.451$ .

### 6.2.3 Systematics

Again most of the systematic errors were estimated by changing various cuts applied in the analysis. The list was adopted from Section 5.4.2.

The uncertainty in the efficiency of the trigger was estimated by using two different trigger samples (see Section 6.2.1).

The model dependence was again estimated by changing the distributions of  $Q^2$ ,  $W_{\gamma p}$ ,  $t$  and the  $\omega$  decay angles within the ranges allowed by the results of Section 5.6 or [6] simultaneously.

The uncertainty of the subtraction of background from proton dissociation ( $\gamma p \rightarrow \omega N$  or  $\gamma p \rightarrow \phi N$ ) was estimated by omitting the subtraction and evaluating the ratio of cross sections again.

The systematic uncertainties due to radiative corrections and the luminosity were assumed to be the same for  $\omega$  and  $\phi$  photoproduction and thus to cancel in the determination of the ratio of the cross sections.

### 6.2.4 Analysis of the Mass Spectrum

The spectrum of the invariant mass of the  $\pi^+\pi^-\pi^0$  system  $m_{3\pi}$  after all offline cuts, the fit constraining the  $\gamma\gamma$  mass according to equation (5.1) and the background subtraction according to equation (5.3) is shown in Figure 6.2(a). For comparison, the invariant mass as given by the above Monte Carlo simulations for the reaction  $\gamma p \rightarrow \omega p$  and  $\gamma p \rightarrow \phi p$  is shown in Figure 6.2(b). The spectra were fitted with a function according to equation (5.4) yielding values of the  $\omega$  and  $\phi$  masses in data of  $784 \pm 2$  MeV and  $1010 \pm 8$  MeV, respectively, compatible with those of the Particle Data Group (PDG) [23]. The corresponding values of the Gaussian standard deviations are  $26 \pm 3$  MeV and  $29 \pm 12$  MeV, respectively. The results of the fits to the two Monte Carlo samples are:  $784 \pm 1$  MeV and  $1021 \pm 1$  MeV for the masses and  $29 \pm 1$  MeV and  $30 \pm 1$  MeV for the standard deviations. The agreement with the data is good.

The number of  $\omega$  and  $\phi$  candidates observed after background subtraction was determined by integrating the fitted Breit-Wigner functions in equation (5.4) within the kinematic limits. This yielded  $N_\omega = 203 \pm 18$  and  $N_\phi = 70 \pm 14$ .

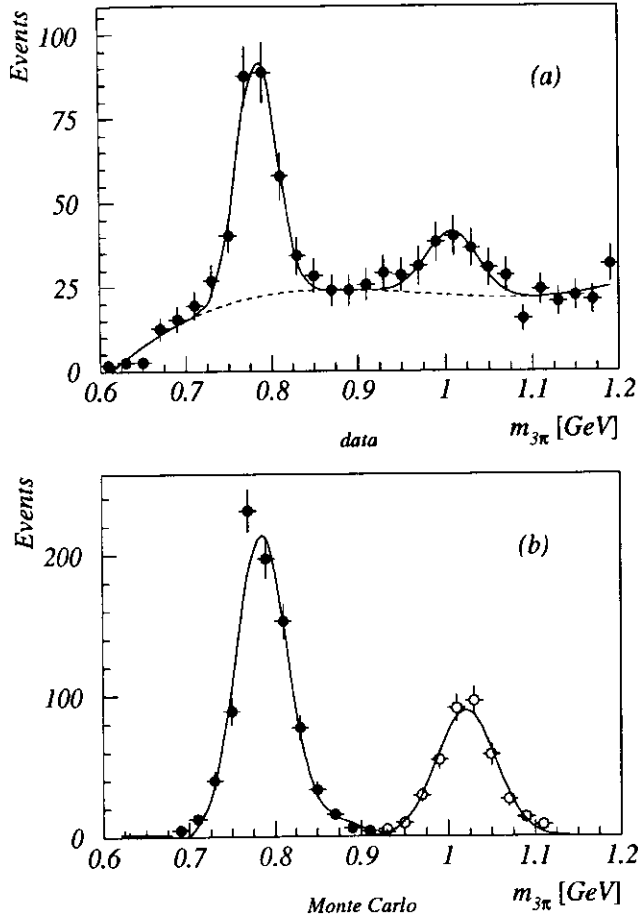


**Figure 6.2:** Invariant mass distribution of the  $\pi^+\pi^-\pi^0$  system after all offline cuts and the fit based on equation (5.1). (a) shows the data, (b) Monte Carlo events from  $\gamma p \rightarrow \omega p$  (solid circles) and  $\gamma p \rightarrow \phi p$  (open circles). The full line is a fit based on equation (5.4); the dashed line indicates the background as determined by the fits.

check	contribution
cut on $E_{CAL}$	4%
cut on $E_{3rd}$	2%
cut on $E_{HES}$	4%
calibration of $E_{HES}$	4%
cut on $m_{\gamma\gamma}$	3%
cut on $n_{track}$	4%
cut on $p_{Ttrack}$	3%
cut on $W_{\gamma p}$	3%
inel. backgr. subt.	1%
model dependence	5%
trigger efficiency	1%
total	11%

**Table 6.1:** List of the various contributions to the systematic error in  $\sigma^{\gamma p \rightarrow \omega p} : \sigma^{\gamma p \rightarrow \phi p}$ .

### 6.2.5 Ratio of the Cross Sections

The ratio of the  $\omega$  to the  $\phi$  elastic photoproduction cross section is given by:

$$\sigma^{\gamma p \rightarrow \omega p} : \sigma^{\gamma p \rightarrow \phi p} = 1 : \frac{N_\phi \epsilon_\omega B_{\omega \rightarrow 3\pi} \Phi_\omega}{N_\omega \epsilon_\phi B_{\phi \rightarrow 3\pi} \Phi_\phi},$$

where  $B_i$  are the branching ratios of the three-pion decay modes and  $\Phi_i$  the effective photon fluxes as given in Section 5.6.1. Using the number of events and the ratio of efficiencies from above we have thus:

$$\sigma^{\gamma p \rightarrow \omega p} : \sigma^{\gamma p \rightarrow \phi p} = 1 : 0.86 \pm 0.19(\text{stat.}) \pm 0.09(\text{syst.}).$$

The systematic error was estimated as described above. The single contributions are listed in Table 6.1. The result is in good agreement with that given in equation (6.1).

This value can be specified using the results from 1994 in addition. With the number of events given in Section 5.5.1 and the acceptance from Section 5.2.2 the  $\omega$  to  $\phi$  ratio was determined to be:

$$\sigma^{\gamma p \rightarrow \omega p} : \sigma^{\gamma p \rightarrow \phi p} = 1 : 0.73 \pm 0.30(\text{stat.}).$$

Assuming the same source of systematic errors for the 1994 and 1995 results – which is justified as the trigger contributing little to the error is the only difference in the selection criteria between 1994 and 1995 – the mean of both was determined using the statistical error as weight. A systematic error of 11% (see above) was then assumed for the mean yielding:

$$\sigma^{\gamma p \rightarrow \omega p} : \sigma^{\gamma p \rightarrow \phi p} = 1 : 0.81 \pm 0.11(\text{stat.}) \pm 0.09(\text{syst.}).$$

This is much more precise than the value given in equation (6.1) and thus will be used in the following. Together with the  $\rho^0$  to  $\omega$  ratio from equation (6.1) we have therefore:

$$\sigma^{\gamma p \rightarrow \rho^0 p} : \sigma^{\gamma p \rightarrow \omega p} : \sigma^{\gamma p \rightarrow \phi p} = 9.17 \pm 0.92 \pm 2.27 : 1 : 0.81 \pm 0.11 \pm 0.09. \quad (6.2)$$

### 6.3 Discussion

The ratio of the  $\gamma \leftrightarrow V$  coupling constants can be determined from the SU(6) quark model [7]. In its simplest form the light vector mesons are described by the following quark content:

$$\rho^0 = \frac{1}{\sqrt{2}}(u\bar{u} - d\bar{d}) \quad (6.3)$$

$$\omega = \frac{1}{\sqrt{2}}(u\bar{u} + d\bar{d}) \quad (6.4)$$

$$\phi = s\bar{s} \quad (6.5)$$

The strength of the coupling of a photon to a quark-antiquark-pair  $q\bar{q}$  is given by  $\sqrt{\alpha}e_q$ , where  $e_q$  is the fraction of the elementary charge carried by the quark. In the case of superposition of several quarks with an amplitude  $a_q$  we have a coupling with  $\sum_q \sqrt{\alpha}a_q e_q$ . On the other hand the strength of the coupling of a photon to a vector meson in VDM is given by equation (2.14), i.e. by  $4\pi\sqrt{\alpha}/f_V$  for  $Q^2 = 0$ . The square of both is proportional to the  $\gamma \leftrightarrow V$  or  $\gamma \leftrightarrow q\bar{q}$  transition probability and thus one expects [77]:

$$f_V^{-2} \sim \left( \sum_q a_q e_q \right)^2 \quad (6.6)$$

Therefore equations (6.3), (6.4) and (6.5) yield:

$$f_{\rho^0}^{-2} : f_{\omega}^{-2} : f_{\phi}^{-2} = 9 : 1 : 2.$$

This ratio is slightly modified as the  $\omega$  and  $\phi$  mesons are not the pure states as given by equations (6.4) and (6.5) [78]. The following singlet and octet states are formed in SU(6) [79]:

$$\omega_1 = \frac{1}{\sqrt{3}}(u\bar{u} + d\bar{d} + s\bar{s})$$

$$\omega_8 = \frac{1}{\sqrt{6}}(u\bar{u} + d\bar{d} - 2s\bar{s})$$

They have to be mixed to get the observed  $\omega$  and  $\phi$  mesons:

$$\omega = \omega_8 \sin \theta_V + \omega_1 \cos \theta_V$$

$$\phi = \omega_8 \cos \theta_V - \omega_1 \sin \theta_V$$

where  $\theta_V$  is the mixing angle. The case of "ideal" mixing, i.e. requiring the quark content given in equations (6.4) and (6.5), needs  $\theta_V \approx 35.3^\circ$ . Mass considerations require [79]:

$$\tan \theta_V = \frac{m_{\phi}^2 - m_{\omega_8}^2}{m_{\omega_8}^2 - m_{\omega}^2},$$

where the mass of the  $\omega_8$  state is determined by:

$$m_{\omega_8}^2 = \frac{1}{3}(4m_K^2 - m_{\rho}^2)$$

yielding  $\theta_V \approx 39^\circ$  [23]. Thus the  $\omega$  has an  $s\bar{s}$  admixture while the  $\phi$  has an  $u\bar{u} + d\bar{d}$  admixture. Therefore equation (6.6) yields:

$$\begin{aligned} f_{\omega}^{-2} : f_{\phi}^{-2} &= 1 : \cot^2 \theta_V \\ &\approx 1 : 1.5 \end{aligned}$$

where  $\theta_V = 39^\circ$  has been used.

For the relation to the ratio of cross sections a difference between the hadronic  $\omega p(\rho^0 p)$  and  $\phi p$  cross sections which is transferred to the photoproduction cross section has to be taken into account. Within the framework of VDM we have (see equation (2.24)):

$$\sigma^{\gamma p \rightarrow V p} \sim f_V^{-2} \sigma^{V p \rightarrow V p}.$$

While the quark model suggests  $\sigma^{\rho^0 p \rightarrow \rho^0 p} \approx \sigma^{\omega p \rightarrow \omega p}$ , we expect  $\sigma^{\omega p \rightarrow \omega p} \neq \sigma^{\phi p \rightarrow \phi p}$  which is confirmed by the results from the fits discussed in Section 2.4.1. Using equation (2.33) gives:

$$f_{\omega}^{-2} : f_{\phi}^{-2} \approx (\sigma^{\gamma p \rightarrow \omega p} : \sigma^{\gamma p \rightarrow \phi p}) / \left( \frac{(\sigma_{tot}^{\omega p})^2}{b_{\omega}} : \frac{(\sigma_{tot}^{\phi p})^2}{b_{\phi}} \right).$$

The parametrizations for  $\sigma_{tot}^{V p}$  and  $b$  as given in Tables 2.4, 2.5 and equations (2.53), (2.55) yield at  $W_{\gamma p} = 80 \text{ GeV}$ :

$$\frac{(\sigma_{tot}^{\omega p})^2}{b_{\omega}} : \frac{(\sigma_{tot}^{\phi p})^2}{b_{\phi}} \approx 1.6$$

and therefore;

$$f_{\omega}^{-2} : f_{\phi}^{-2} \approx (\sigma^{\gamma p \rightarrow \omega p} : \sigma^{\gamma p \rightarrow \phi p}) / 1.6.$$

Application to the result of equation (6.2) yields thus:

$$f_{\rho^0}^{-2} : f_{\omega}^{-2} : f_{\phi}^{-2} = 9.17 \pm 0.92 \pm 2.27 : 1 : 1.30 \pm 0.18 \pm 0.14.$$

Indeed, if one uses the results for  $f_V$  given in the last column of Table 2.3 one gets:

$$f_{\rho^0}^{-2} : f_{\omega}^{-2} : f_{\phi}^{-2} = 9.14 \pm 1.68 : 1 : 1.31 \pm 0.23.$$

Both results are in good agreement with each other and the SU(6) expectation.



## Chapter 7

### Conclusion

The reaction  $\gamma p \rightarrow \omega p$  ( $\omega \rightarrow \pi^+ \pi^- \pi^0$  and  $\pi^0 \rightarrow \gamma\gamma$ ) has been studied in  $ep$  interactions at HERA using the ZEUS detector. The kinematic range was defined by  $70 < W_{\gamma p} < 90$  GeV and  $|t| < 0.6$  GeV<sup>2</sup>. For the considered events the scattered positron was not observed in the detector, thereby restricting the photon virtuality  $Q^2$  to values smaller than 4 GeV<sup>2</sup>, with a median  $Q^2$  of about 10<sup>-4</sup> GeV<sup>2</sup>. The elastic  $\omega$  photoproduction cross section has been measured to be:

$$\sigma^{\gamma p \rightarrow \omega p} = 1.21 \pm 0.12 \pm 0.23 \mu\text{b}.$$

The differential cross section  $d\sigma^{\gamma p \rightarrow \omega p}/d|t|$  has an exponential shape  $e^{-b|t|}$  with a slope:

$$b = 10.0 \pm 1.2 \pm 1.3 \text{ GeV}^{-2}.$$

Both is in accord with expectations from models based on Regge theory and the vector meson dominance model. The angular distributions of the decay pions are consistent with  $s$ -channel helicity conservation.

The ratio of  $\rho^0$  to  $\omega$  to  $\phi$  cross sections at  $W_{\gamma p} \approx 80$  GeV was determined to be:

$$\sigma^{\gamma p \rightarrow \rho^0 p} : \sigma^{\gamma p \rightarrow \omega p} : \sigma^{\gamma p \rightarrow \phi p} = 9.17 \pm 0.92 \pm 2.27 : 1 : 0.81 \pm 0.11 \pm 0.09,$$

where the first ratio was obtained from the 1994  $\rho^0$  [39] and  $\omega$  photoproduction measurement, while the second ratio was determined using the same measurement of the  $\omega$  and  $\phi$  resonances in the reaction  $\gamma p \rightarrow \pi^+ \pi^- \pi^0 p$  based on the data taken in 1994 and 1995. The ratio is in good agreement with expectations from the SU(6) quark model.

## Appendix A

### Decay Angular Distributions

The study of the angular distributions of the decay products of a vector meson  $V$  produced in reaction (2.18) as discussed in Section 2.3.3 is a tool for checking different production models. The formalism to derive equations (2.29) and (2.30), the decay angular distributions in terms of the vector meson's density matrix elements  $\rho(V)$  describing its spin state, is given below.

#### A.1 The Density Matrices

The polarization states of the virtual photon exchanged between the positron and the proton in reaction (2.18) can be described by a density matrix  $\rho(\gamma)$ . It is essentially given by the leptonic tensor (2.2). A decomposition into an orthogonal set of hermitian matrices  $\Sigma^\alpha$  yields [80]

$$\rho(\gamma) = \frac{1}{2} \sum_{\alpha=0}^8 \tilde{\Pi}_\alpha \Sigma^\alpha, \quad (\text{A.1})$$

with:

$$\begin{aligned} \Sigma^0 &= \begin{pmatrix} 1 & 0 & 0 \\ 0 & 0 & 0 \\ 0 & 0 & 1 \end{pmatrix}; & \Sigma^1 &= \begin{pmatrix} 0 & 0 & 1 \\ 0 & 0 & 0 \\ 1 & 0 & 0 \end{pmatrix}; & \Sigma^2 &= \begin{pmatrix} 0 & 0 & -i \\ 0 & 0 & 0 \\ i & 0 & 0 \end{pmatrix}; \\ \Sigma^3 &= \begin{pmatrix} 1 & 0 & 0 \\ 0 & 0 & 0 \\ 0 & 0 & -1 \end{pmatrix}; & \Sigma^4 &= 2 \begin{pmatrix} 0 & 0 & 0 \\ 0 & 1 & 0 \\ 0 & 0 & 0 \end{pmatrix}; & \Sigma^5 &= \frac{1}{\sqrt{2}} \begin{pmatrix} 0 & 1 & 0 \\ 1 & 0 & -1 \\ 0 & -1 & 0 \end{pmatrix}; \\ \Sigma^6 &= \frac{1}{\sqrt{2}} \begin{pmatrix} 0 & -i & 0 \\ i & 0 & i \\ 0 & -i & 0 \end{pmatrix}; & \Sigma^7 &= \frac{1}{\sqrt{2}} \begin{pmatrix} 0 & 1 & 0 \\ 1 & 0 & 1 \\ 0 & 1 & 0 \end{pmatrix}; & \Sigma^8 &= \frac{1}{\sqrt{2}} \begin{pmatrix} 0 & -i & 0 \\ i & 0 & -i \\ 0 & i & 0 \end{pmatrix}. \end{aligned}$$

The vector  $\tilde{\Pi}$  is given by the positron polarization and kinematical quantities. The matrices  $\Sigma^0$ - $\Sigma^3$  describe transverse photons, where  $\Sigma^0$  represents the unpolarized part.  $\Sigma^4$  describes longitudinal photons and  $\Sigma^5$ - $\Sigma^8$  represent transverse-longitudinal interference terms.

Let  $T$  be the transition matrix for the reaction  $\gamma^* p \rightarrow V p'$ , i.e.:

$$T_{\lambda_V \lambda_{p'} \lambda_\gamma \lambda_p} = \langle \lambda_V \lambda_{p'} | j_\lambda, | \lambda_p \rangle,$$

where  $j$  denotes the matrix of the electromagnetic current. As a consequence of parity conservation,  $T$  obeys the following symmetry relation [80]:

$$T_{-\lambda_V - \lambda_{\mu'}, -\lambda_\gamma - \lambda_p} = (-1)^{(\lambda_V - \lambda_{\mu'}) + (\lambda_\gamma - \lambda_p)} \cdot T_{\lambda_V \lambda_{\mu'} \lambda_\gamma \lambda_p}. \quad (\text{A.2})$$

The density matrix  $\rho(V)$  defining the polarization state of the vector meson  $V$  is then given by the transition matrix and the photon density matrix:

$$\rho(V) = T \rho(\gamma) T^\dagger.$$

It can be decomposed into hermitian matrices  $\rho^\alpha$  corresponding to the decomposition of  $\rho(\gamma)$  given by equation (A.1):

$$\rho(V) = \sum_{\alpha=0}^6 \Pi_\alpha \rho^\alpha, \quad (\text{A.3})$$

with:

$$\rho_{\lambda_V \lambda_V'}^\alpha = \frac{1}{N_\alpha} \sum_{\lambda_{\mu'} \lambda_p \lambda_\gamma \lambda_\gamma'} T_{\lambda_V \lambda_{\mu'} \lambda_\gamma \lambda_p} \Sigma_{\lambda_\gamma \lambda_\gamma'}^\alpha T_{\lambda_V \lambda_{\mu'} \lambda_\gamma \lambda_p}^*, \quad (\text{A.4})$$

where  $N_\alpha$  is a normalisation factor chosen such that  $\text{Tr} \rho^0 = \text{Tr} \rho^4 = 1$ .  $\Pi$  differs from  $\tilde{\Pi}$  only by a different normalisation. The components of the vector  $\Pi$  vanish except  $\Pi_0$  and  $\Pi_4$  in the case of unpolarized incoming and undetected scattered positron [80]. Thus only  $\rho^0$  and  $\rho^4$  are relevant to this analysis. Using the symmetry properties of  $T$  as given by equation (A.2) and those of  $\Sigma^\alpha$  we have:

$$\rho_{-\lambda - \lambda'}^\alpha = (-1)^{\lambda - \lambda'} \rho_{\lambda \lambda'}^\alpha. \quad (\text{A.5})$$

## A.2 The Probability Distributions

The probability distribution of the decay angles  $\theta_h$  and  $\phi_h$  in the restframe of the vector meson  $V$  as defined in Section 2.3.3 is given by the decay amplitude  $\mathcal{M}$  and the density matrix  $\rho(V)$  [19]:

$$W(\cos \theta_h, \phi_h) = \frac{1}{N} \frac{dN}{d \cos \theta_h d \phi_h} = \sum_{\lambda_V \lambda_V'} \langle \theta_h, \phi_h | \mathcal{M} | \lambda_V \rangle \rho(V)_{\lambda_V \lambda_V'} \langle \lambda_V' | \mathcal{M}^\dagger | \theta_h, \phi_h \rangle,$$

Using the rotation matrices  $D$  from quantum mechanics, one has [81]:

$$\langle \theta_h, \phi_h | \mathcal{M} | \lambda_V \rangle = C \sqrt{\frac{3}{4\pi}} D_{\lambda_V \Lambda}^1(\phi_h, \theta_h, -\phi_h)^*,$$

where  $\Lambda$  is the difference of the helicities in the final state. In the following two possibilities are distinguished:

- (a) The decay into spinless particles:  $\Lambda = 0$  (e.g. for the decay  $\rho^0 \rightarrow \pi^+ \pi^-$ );
- (b) the decay into a particle of spin 1 and a spinless particle:  $\Lambda = \pm 1$  (e.g. for the decay  $\phi \rightarrow \rho \pi$ ).

Thus case (a) is described by:

$$W_s(\cos \theta_h, \phi_h) = \frac{3}{4\pi} \sum_{\lambda_V \lambda_V'} D_{\lambda_V 0}^1(\phi_h, \theta_h, -\phi_h)^* \rho(V)_{\lambda_V \lambda_V'} D_{\lambda_V 0}^1(\phi_h, \theta_h, -\phi_h),$$

while case (b) is described by:

$$W_v(\cos \theta_h, \phi_h) = \frac{3}{4\pi} \sum_{\lambda_V \lambda_V'} D_{\lambda_V \pm 1}^1(\phi_h, \theta_h, -\phi_h)^* \rho(V)_{\lambda_V \lambda_V'} D_{\lambda_V \pm 1}^1(\phi_h, \theta_h, -\phi_h).$$

The angular distribution is decomposed according to equation (A.3):

$$W(\cos \theta_h, \phi_h) = \sum_{\alpha=0}^6 \Pi_\alpha W^\alpha(\cos \theta_h, \phi_h).$$

Using the explicit form of the rotation matrices:

$$\begin{aligned} D_{10}^1(\phi_h, \theta_h, -\phi_h) &= -D_{0-1}^1(\phi_h, \theta_h, -\phi_h) = -\frac{1}{\sqrt{2}} \sin \theta_h e^{-i\phi_h}, \\ D_{01}^1(\phi_h, \theta_h, -\phi_h) &= -D_{-10}^1(\phi_h, \theta_h, -\phi_h) = \frac{1}{\sqrt{2}} \sin \theta_h e^{i\phi_h}, \\ D_{11}^1(\phi_h, \theta_h, -\phi_h) &= D_{-1-1}^1(\phi_h, \theta_h, -\phi_h) = \frac{1}{2} (1 + \cos \theta_h), \\ D_{-1-1}^1(\phi_h, \theta_h, -\phi_h) &= D_{11}^1(\phi_h, \theta_h, -\phi_h) = \frac{1}{2} (1 - \cos \theta_h) e^{-2i\phi_h}, \end{aligned}$$

together with the above symmetry properties of  $\rho^0$  and  $\rho^4$  given by equation (A.5) and the trace condition  $\text{Tr} \rho^0 = \text{Tr} \rho^4 = 1$  we have:

$$\begin{aligned} W_s^\alpha(\cos \theta_h, \phi_h) &= \frac{3}{4\pi} \left[ \frac{1}{2} (1 - \rho_{00}^\alpha) + \frac{1}{2} (3\rho_{00}^\alpha - 1) \cos^2 \theta_h - \sqrt{2} \text{Re}\{\rho_{10}^\alpha\} \sin 2\theta_h \cos \phi_h \right. \\ &\quad \left. - \rho_{1-1}^\alpha \sin^2 \theta_h \cos 2\phi_h \right], \\ W_v^\alpha(\cos \theta_h, \phi_h) &= \frac{3}{4\pi} \left[ \frac{1}{2} (1 + \rho_{00}^\alpha) - \frac{1}{2} (3\rho_{00}^\alpha - 1) \cos^2 \theta_h - \sqrt{2} \text{Re}\{\rho_{10}^\alpha\} \sin \theta_h \cos \phi_h \right. \\ &\quad \left. + \rho_{1-1}^\alpha \sin^2 \theta_h \cos 2\phi_h \right]. \end{aligned}$$

To simplify the notation, the matrix  $r^{04}$  can be introduced as a composition of  $\rho^0$  and  $\rho^4$ :

$$r^{04} = \Pi_0 \rho^0 + \Pi_4 \rho^4.$$

Thus the recombination of the  $W^\alpha(\cos \theta_h, \phi_h)$  yields, using the fact that  $\Pi_\alpha = 0$  for  $\alpha \neq 0, 4$  (see above):

$$\begin{aligned} W_s(\cos \theta_h, \phi_h) &= \frac{3}{4\pi} \left[ \frac{1}{2} (1 - r_{00}^{04}) + \frac{1}{2} (3r_{00}^{04} - 1) \cos^2 \theta_h - \sqrt{2} \text{Re}\{r_{10}^{04}\} \sin 2\theta_h \cos \phi_h \right. \\ &\quad \left. - r_{1-1}^{04} \sin^2 \theta_h \cos 2\phi_h \right] \\ W_v(\cos \theta_h, \phi_h) &= \frac{3}{4\pi} \left[ \frac{1}{2} (1 + r_{00}^{04}) - \frac{1}{2} (3r_{00}^{04} - 1) \cos^2 \theta_h - \sqrt{2} \text{Re}\{r_{10}^{04}\} \sin \theta_h \cos \phi_h \right. \\ &\quad \left. + r_{1-1}^{04} \sin^2 \theta_h \cos 2\phi_h \right] \end{aligned}$$

The distributions of  $\cos \theta_h$  and  $\phi_h$  are measured separately in this analysis and thus one has to average over  $\phi_h$  or  $\cos \theta_h$ , respectively, yielding:

$$W(\cos \theta_h) = \frac{3}{4} [1 \mp r_{00}^{04} \pm (3r_{00}^{04} - 1) \cos^2 \theta_h],$$

$$W(\phi_h) = \frac{1}{2\pi} [1 \mp 2r_{1-1}^{04} \cos 2\phi_h],$$

where the upper sign describes the decay into scalar particles only (case (a)) and the lower sign the decay producing a vectorial particle (case (b)).

### A.3 The Density Matrices in Case of SCHC

If the helicity is conserved in the hadronic centre-of-mass system, the case of SCHC is fulfilled. Thus we have  $\lambda_V = \lambda_\gamma$  and  $\lambda_{p'} = \lambda_p$  so that equation (A.4) is reduced to:

$$\rho_{\lambda_V \lambda_V}^\alpha = \Sigma_{\lambda_V \lambda_V}^\alpha \frac{1}{N_\alpha} \sum_{\lambda_p} T_{\lambda_V \lambda_p, \lambda_V \lambda_p} T_{\lambda_V \lambda_p, \lambda_V \lambda_p}^*$$

As  $\Sigma_{11}^0$ ,  $\Sigma_{-1-1}^0$  and  $\Sigma_{00}^4$  are the only non-vanishing  $\Sigma^\alpha$ -matrix elements for  $\alpha = 0, 4$ , the same is therefore true for  $\rho^0$  and  $\rho^4$ . Equation (A.5) requires  $\rho_{11}^0 = \rho_{-1-1}^0$ , so that the trace condition  $\text{Tr} \rho^0 = \text{Tr} \rho^4 = 1$  yields:

$$\rho^0 = \frac{1}{2} \begin{pmatrix} 1 & 0 & 0 \\ 0 & 0 & 0 \\ 0 & 0 & 1 \end{pmatrix}; \quad \rho^4 = \begin{pmatrix} 0 & 0 & 0 \\ 0 & 1 & 0 \\ 0 & 0 & 0 \end{pmatrix}.$$

Using the explicit form of the vector  $\Pi$  as used in the decomposition of  $\rho(V)$  [80] we have:

$$r_{04} = \frac{\rho^0 + (\epsilon + \delta)R\rho^4}{1 + (\epsilon + \delta)R}$$

with the fraction of the longitudinal to the transverse virtual photon flux [9]:

$$\epsilon = \left( 1 + \frac{y^2 + 16m_p^2 Q^2 / W_{\gamma p}^4}{2(1-y) - 8Q^2 m_p^2 / W_{\gamma p}^4} \right)^{-1},$$

the mass correction factor:

$$\delta = \frac{2m_e^2}{Q^2} (1 - \epsilon),$$

and  $R = \sigma_L^{\gamma^* p} / \sigma_T^{\gamma^* p}$ , the ratio of the longitudinal to the transverse photon-proton cross section. Due to  $\rho_{1-1}^0 = \rho_{-1-1}^0 = 0$  (see above) we have:

$$r_{1-1}^{04} = 0,$$

while  $\rho_{00}^0 = 0$  and  $\rho_{00}^4 = 1$  gives:

$$r_{00}^{04} = \frac{(\epsilon + \delta)R}{1 + (\epsilon + \delta)R},$$

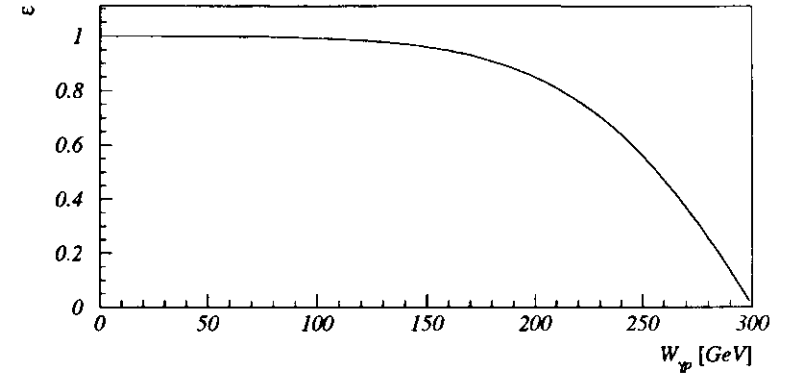


Figure A.1: The fraction  $\epsilon$  of the longitudinal to the transverse virtual photon flux versus  $W_{\gamma p}$ .

which is equivalent to:

$$R = \frac{1}{\epsilon + \delta} \frac{r_{00}^{04}}{1 - r_{00}^{04}}.$$

In the HERA photoproduction kinematic range  $m_p^2 Q^2$  can be neglected against  $W_{\gamma p}^4$  and thus we have:

$$\epsilon \approx \frac{2(1-y)}{1 + (1-y)^2}.$$

The behaviour of  $\epsilon$  in this approximation versus  $W_{\gamma p}$  is shown in Figure A.1. For sufficiently small  $W_{\gamma p}$  we have  $\epsilon \approx 1$  and thus  $\delta \approx 0$  so that:

$$r_{00}^{04} \approx \frac{R}{1+R} \Leftrightarrow R \approx \frac{r_{00}^{04}}{1 - r_{00}^{04}}.$$

## Bibliography

- [1] G.A. Schuler and T. Sjöstrand, Nucl. Phys. **B407** (1993) 539.
- [2] A. Donnachie and P.V. Landshoff, Phys. Lett. **B296** (1992) 227.
- [3] T.H. Bauer et al., Rev. Mod. Phys. **50** (1978) 261.
- [4] ZEUS Collab., M. Derrick et al., Phys. Lett. **B350** (1995) 120.
- [5] ZEUS Collab., M. Derrick et al., Z. Phys. **C69** (1995) 39.
- [6] ZEUS Collab., M. Derrick et al., Phys. Lett. **B377** (1996) 259.
- [7] C.A. Levinson, H.J. Lipkin, and S. Meshkov, Phys. Lett. **7** (1963) 81.
- [8] F.J. Gilman, Phys. Rev. **167** (1967) 1365.
- [9] L.N. Hand, Phys. Rev. **129** (1963) 1834.
- [10] J.J. Sakurai, Ann. Phys. **11** (1960) 1.
- [11] K. Fujikawa, Phys. Rev. **D4** (1971) 2794;  
J.J. Sakurai and D. Schildknecht, Phys. Lett. **B40** (1972) 121;  
J.J. Sakurai and D. Schildknecht, Phys. Lett. **B41** (1972) 489;  
J.J. Sakurai and D. Schildknecht, Phys. Lett. **B42** (1972) 216;  
A. Bramón and M. Greco, Nuovo Cim. Lett. **3** (1972) 693;  
A. Bramón, E. Etim, and M. Greco, Phys. Lett. **B41** (1972) 609.
- [12] D.R. Yennie, Rev. Mod. Phys. **47** (1975) 311.
- [13] J.J. Sakurai, Phys. Rev. Lett. **22** (1969) 981.
- [14] N.N. Achasov and V.A. Karnekov, Sov. J. Nucl. Phys. **38** (1983) 736.
- [15] P. Joos et al., Nucl. Phys. **B 113** (1976) 53;  
C. del Papa et al., Phys. Rev. **D19** (1979) 1303;  
ZEUS Collab., M. Derrick et al., Ref. pa 02-053, ICHEP96 Conference in Warsaw, 25-31 July, 1996.
- [16] M.G. Ryskin, Z. Phys. **C57** (1993) 89.
- [17] E. Lohrmann, *Hochenergiephysik*, Teubner Studienbücher: Physik (1986).

- [18] K. Goulianos, Phys. Rep. **101**(1983) 169.
- [19] K. Schilling, P. Seyboth, and G. Wolf, Nucl. Phys. **B15** (1970) 397.
- [20] SBT Collab., J. Ballam et al., Phys. Rev. **D7** (1973) 3150.
- [21] J.P. Bruq et al., Phys. Lett. **B77** (1978) 438;  
L.A. Fajardo et al., Phys. Rev. **D24** (1980) 46.
- [22] E.M. Levin and L.L. Frankfurt, JETP Lett. **2** (1965) 65;  
H.J. Lipkin, Phys. Rev. Lett. **16** (1966) 71;  
H.J. Lipkin, Phys. Lett. **B335** (1994) 500.
- [23] R.M. Barnett et al., Phys. Rev. **D54** (1996) 1.
- [24] R.M. Egloff et al., Phys. Rev. Lett. **43** (1979) 657.
- [25] R.M. Egloff et al., Phys. Rev. Lett. **43** (1979) 1545 and **44** (1980) 690 (Erratum).
- [26] A.M. Breakstone et al., Phys. Rev. Lett. **47** (1981) 1782.
- [27] D. Aston et al., Nucl. Phys. **B209** (1982) 56.
- [28] OMEGA Collab., M. Atkinson et al., Nucl. Phys. **B231** (1984) 15.
- [29] J. Busenitz et al., Phys. Rev. **D40** (1989) 1.
- [30] A. Donnachie and P.V. Landshoff, Phys. Lett. **B348** (1995) 213.
- [31] P.D.B. Collins, *An Introduction to Regge Theory and High Energy Physics*, Cambridge University Press (1977).
- [32] A. Donnachie and P.V. Landshoff, Nucl. Phys. **B231** (1984) 189.
- [33] A. Baldini et al., *Numerical Data and Functional Relationships in Science and Technology*, Group I, Vol. 12a and 12b, Landolt-Börnstein, New Series (1988).
- [34] CDF Collab., F. Abe et al., Phys. Rev. **D50** (1994) 5550.
- [35] J.-R. Cudell, K. Kang, and S.K. Kim, e-Print Archive hep-ph/9601336 (1996).
- [36] A. Donnachie and P.V. Landshoff, Nucl. Phys. **B267** (1986) 690.
- [37] C.W. Akerlof et al., Phys. Rev. **D14** (1976) 2864;  
D.S. Ayres et al., Phys. Rev. **D15** (1977) 3105;  
A. Schiz et al., Phys. Rev. **D24** (1981) 26;  
D. Brick et al., Phys. Rev. **D25** (1982) 2794;  
NA22 Collab., M. Adamus et al., Phys. Lett. **B186** (1987) 223.
- [38] H1 Collab., S. Aid et al., Nucl. Phys. **B463** (1996) 3.
- [39] D. Westphal, PhD thesis, University of Hamburg, in preparation.
- [40] H. Cheng, J.K. Walker, and T.T. Wu, Phys. Lett. **B44** (1973) 97.

- [41] C. Bourrely, J. Soffer, and T.T. Wu, Nucl. Phys. **B247** (1984) 15.
- [42] G. Wolf, DESY 94-022 (1994).
- [43] H1 Collab., I. Abt et al., DESY 93-103 (1993).
- [44] The ZEUS Detector, Status Report, DESY (1993).
- [45] M. Derrick et al., Nucl. Instrum. Methods **A 309** (1991) 77;  
A. Andresen et al., Nucl. Instrum. Methods **A 309** (1991) 101;  
A. Bernstein et al., Nucl. Instrum. Methods **A 336** (1993) 23.
- [46] A. Bornheim et al., ZEUS-Note 95-130.
- [47] A. Dwurażny et al., Nucl. Instrum. Methods **A 277** (1989) 176.
- [48] I. Fleck, PhD thesis, University of Hamburg 1994; F35D-94-09, DESY internal report (*in German*).
- [49] C. Alvisi et al., Nucl. Instrum. Methods **A 305** (1991) 30.
- [50] N. Harnew et al., Nucl. Instrum. Methods **A 279** (1989) 290;  
C.B. Brooks et al., Nucl. Instrum. Methods **A 283** (1989) 477;  
B. Foster et al., Nucl. Instrum. Methods **A 338** (1994) 254.
- [51] B. Bock et al., Nucl. Instrum. Methods **A 344** (1994) 335.
- [52] D. Kisiielewska et al., DESY-HERA 85-25 (1985);  
J. Andruszków et al., DESY 92-066 (1992).
- [53] W. Schott, ZEUS-Note 95-039.
- [54] M. Kasprzak, ZEUS-Note 92-072.
- [55] W.H. Smith, K. Tokushuku, and L.W. Wiggers, in the Proceedings of CHEP 92 in Annecy, 21-25 September 1992, p. 222.
- [56] P. de Jong, ZEUS-Note 92-019.
- [57] T. Doeker, A. Frey, and M. Nakao, ZEUS-Note 94-123.
- [58] G. Jahn, PhD thesis, University of Hamburg 1992; F35D-92-03, DESY internal report (*in German*).
- [59] T. Kuhn-Sander, Diploma thesis, University of Hamburg 1996; F35D-96-15, DESY internal report (*in German*).
- [60] I. Fleck and K. Ohrenberg, ZEUS-Note 95-009.
- [61] J. Grosse-Knetter, ZEUS-Note 95-089;  
J. Grosse-Knetter, ZEUS-Note 96-034.
- [62] ZEUS Collab., M. Derrick et al., Z. Phys. **C73** (1996) 73.

- [63] T. Sjöstrand and M. Bengtsson, *Comput. Phys. Commun.* **43** (1987) 367;  
M. Bengtsson and T. Sjöstrand, *Comput. Phys. Commun.* **46** (1987) 43;  
T. Sjöstrand, in *Proceedings of the Workshop Physics at HERA*, DESY, 29-30 October 1991,  
ed. W. Buchmüller and G. Ingelman, p. 1405.
- [64] M. Arneodo, L. Lamberti, and M.G. Ryskin, DESY 96-149 (1996); submitted to *Comput. Phys. Commun.*
- [65] H. Abramowicz et al., *Phys. Lett.* **B269** (1991) 465.
- [66] K. Kurek, e-Print Archive hep-ph/9606240 (1996).
- [67] G. Zech, DESY 95-113 (1995).
- [68] L. Köpke and R. van Woudenberg, ZEUS-Note 94-016.
- [69] K. Piotrkowski and M. Zachara, ZEUS-Note 95-138.
- [70] ZEUS Collab., M. Derrick et al., *Z. Phys.* **C63** (1994) 391;  
H1 Collab., S. Aid et al., *Z. Phys.* **C69** (1995) 27.
- [71] H.R. Crouch et al., *Phys. Rev.* **155** (1967) 1468.
- [72] ABBHHM Collab., R. Erbe et al., *Phys. Rev.* **175** (1968) 1669.
- [73] M. Davier et al., *Phys. Rev.* **D1** (1970) 790.
- [74] SWT Collab., Y. Eisenberg et al., *Phys. Rev.* **D5** (1972) 15.
- [75] W. Struczinski et al., *Nucl. Phys.* **B108** (1976) 45.
- [76] LAMP2 Group, D.P. Barber et al., *Z. Phys.* **C26** (1984) 343.
- [77] R. van Royen and V.F. Weisskopf, *Nuovo Cim.* **A50** (1967) 617.
- [78] M. Ross and L. Stodolsky, *Phys. Rev. Lett.* **17** (1966) 563;  
R.J. Oakes and J.J. Sakurai, *Phys. Rev. Lett.* **19** (1967) 1266;  
T.H. Bauer and D.R. Yennie, *Phys. Lett.* **B60** (1976) 169.
- [79] D.H. Perkins, *Hochenergiophysik*, Addison-Wesley (1990).
- [80] K. Schilling and G. Wolf, *Nucl. Phys.* **B61** (1973) 381.
- [81] K. Gottfried, J.D. Jackson, *Nuovo Cim.* **33** (1964) 309.

### Acknowledgements

It was an exiting experience and great delight to work in a multinational collaboration like ZEUS. I want to thank all its members for their cooperation and help.

It is my pleasure to thank Prof. Dr. E. Lohrmann for enabling me to do this thesis. Especially I want to thank him for his continuous support, encouraging advice and his numerous enlightening ideas.

I address many thanks to the members of the ZEUS photoproduction group, especially M. Arneodo, G. Iacobucci, and A. Proskuryakov for fruitful discussions about this analysis.

As well I would like to thank the members of the HES group for supporting me in my work with HES as well as for their discussions.

Finally special thanks go to the graduate and Diploma students of ZEUS, Heiko Beier, Olaf Deppe, Dirk Westphal,... for being open to any kind of discussion, their abundant help and encouragement.

